Improvement of the methanol-to-hydrocarbons catalytic performance for one-dimensional zeolites obtained by post-synthetic modifications

Dissertation for the degree of

Philosophiae Doctor

Pablo del Campo Huertas

Department of Chemistry

Faculty of Mathematics and Natural Sciences

UNIVERSITY OF OSLO

January 2017

Series of dissertations submitted to the
Faculty of Mathematics and Natural Sciences, University of Oslo
No. 1854

ISSN 1501-7710

Cover: Hanne Baadsgaard Utigard.
Print production: Reprosentralen, University of Oslo.

to my parents, to my sister, to my Ana

Preface

The work presented in this thesis was carried out as a part of a 3.5 year PhD scholarship (beginning May 2013). The project was jointly financed by Department of Chemistry, University of Oslo and the CRI-centre "Innovative Natural Gas processes and Products" (*in*GAP). The PhD study comprises 30 ECTS and research stays for 6 months at the R&D facilities at Haldor Topsøe (Lyngby, Denmark) and for 3 months at the ITQ-UPV Institute (Valencia, Spain). Professor Stian Svelle (University of Oslo) has acted as my principal supervisor and Senior Scientist Palo Beato (Haldor Topsøe) as subsidiary supervisor during the entire project. Professor Unni Olsbye and Professor Karl Petter Lillerud were co-supervisors of the project.

I had the great pleasure to work in a scientific field that really excited me. All the supervisors are acknowledged for the advice and guidance throughout this period. Special thanks to Stian for his professional guidance, sharing excellent ideas, assisting with equipment issues and facilitating my stay in Oslo. Also, I really appreciated the scientific and non-scientific enthusiastic discussions with Unni. She was always open to any query. Pablo is greatly acknowledged for sharing optimism, fresh and innovative ideas and giving me a great time under the period in Denmark. I thank all the UiO group which accompanied me for the help with the experiments performed at the ESRF and the collaboration in the resulting papers. I would like to thank Gloria Bostick for her kind patient assistance with all the administration. The stay at the ITQ-UPV institute was supervised by Professor Fernando Rey and Professor Jose Serra, with experimental help of Miguel Palomino and Maria Teresa Navarro. Thanks to all you for the data discussion and also for the support during my sick leave.

I would like to thank all my present and former colleagues in the catalysis group for a great working environment and time together. Special thanks to Dani Rojo and Michael Dyballa for reading the thesis and Juan S. Martinez-Espín and Andrea Molino for the nice time and useful contributions to the presented work.

Thanks of course to my parents, my sister, family and home friends for all the support given to me. Finally, very special thanks to my Ana, for her loving support and persistence. Without you it would have been impossible to complete this journey together.

List of abbreviations and symbols

IUPAC	International Union of Pure and Applied Chemistry
FCC	Fluid Catalytic Cracking
HDS	Hydrodesulphurization
SCR	Selective Catalytic Reduction
E_a	Activation Energy
EFAl	Extra-framework Aluminium
EFSi	Extra-framework Silicon
SDA	Structure Directing Agent
MTH	Methanol-to-Hydrocarbons
NG	Natural Gas
MTG	Methanol-to-Gasoline
TIGAS	Topsøe Integrated Gasoline Synthesis
DME	Dimethyl Ether
MTO	Methanol-to-Olefins
MTP	Methanol-to-Propylene
HCP	Hydrocarbon Pool
PMB	Polymethylbenzene
WHSV	Weight Hour Space Velocity
TOS	Time on Stream
PDA	Pore Directing Agent

CTAB Cetyltrimethylammonium Bromide

TBAOH Tetrabutylammonium Hydroxide

BAS Brønsted Acid Site

MAS NMR Magic-Angle Nuclear Magnetic Resonance

USY Ultra-Stable Zeolite Y

LAS Lewis Acid Site

BA Brønsted Acidity

LA Lewis Acidity

ASD Acid Site Density

LDPE Low Density Polyethylene

IZA International Zeolite Association

PXRD Powder X-Ray Diffraction

a.u. Arbitrary Units

MP-AES Microwave Plasma-Atomic Emission Spectrometry

SEM Scanning Electron Microscopy

TEM Transmission Electron Microscopy

BET Brunauer, Emmett and Teller

PSD Pore Size Distribution

BJH Barett-Joyner-Halenda

FTIR Fourier Transformed Infrared

MS Mass Spectrometer

TPD Temperature Programmed Desorption

TGA Thermogravimetric Analysis

HXRD	High Energy X-Ray Diffraction
PDP	Powder Diffraction Pattern
GC	Gas Chromatography
FID	Flame Ionization Detector
GC-MS	Gas Chromatograph-Mass Spectrometer
HTI	Hydrogen Transfer Index
Å	Åmstrong (10^{-10} m)
µm	Micrometer (10^{-6} m)
λ	Wavelength
ρ	Density
θ	Angle of diffraction

Table of contents

List of publications

This Thesis is based on the four manuscripts listed and numbered below. The full manuscripts are collected in the Appendix.

Paper I: *Time- and space-resolved high energy operando X-ray diffraction for monitoring the methanol to hydrocarbons reaction over H-ZSM-22 zeolite catalyst in different conditions.* Pablo del Campo, W. A. Slawinski, R. Henry, M. Westgård Erichsen, S. Svelle, P. Beato, D. Wragg*, U. Olsbye*, Surface Science 648 (**2016**) 141–149.

Paper II: *Influence of post-synthetic modifications on the composition, acidity and textural properties of ZSM-22 zeolite.* Pablo del Campo, P. Beato*, F. Rey, M.T. Navarro, U. Olsbye, K.P. Lillerud, S. Svelle*, Catalysis Today (**2017**) http://dx.doi.org/10.1016/j.cattod.2017.04.042

Paper III: *Impact of post-synthetic treatments on unidirectional H-ZSM-22 zeolite catalyst: Towards improved clean MTG catalytic process.* Pablo del Campo, U. Olsbye, K.P. Lillerud, S. Svelle*, P. Beato*, Catalysis Today (**2017**) http://dx.doi.org/10.1016/j.cattod.2017.05.011

Paper IV: *Syngas to liquids via oxygenates.* M. Westgård Erichsen, J.S. Martinez-Espin, F. Joensen, S. Teketel, Pablo del Campo, K.P. Lillerud, S. Svelle, P. Beato*, U. Olsbye*, Book Chapter in "Small-Scale Gas to Liquid Fuel Synthesis", CRC Press **2015**.

*corresponding author(s)

The author's contribution

Paper I: The author participated in planning the experiments and synthesized all the samples. The author was strongly involved in the construction of the experimental setup at synchrotron facilities, contributed to the catalytic operando measurements and performed all the in house catalytic testing and characterization of the samples. The author was strongly involved in data interpretation and writing of the manuscript and all graphics.

Paper II: The author planned the experiments, synthesized and prepared all the samples. The author performed all the characterization of the samples (TEM was done with a technician at ITQ-Valencia or Haldor Topsøe AS). The author strongly participated in data interpretation and writing of the manuscript and all graphics.

Paper III: The author participated in planning the experiments, synthesized all the samples and performed all the characterization of the samples and all the catalytic tests over the materials. The author strongly participated in data interpretation and writing of the manuscript and all graphics.

Paper IV: The author was involved in writing of the manuscript (mostly Sections 3.4 and 3.5 of Paper IV) and preparation of graphics.

This paper is printed as separate and comprises a literature survey on previous publications of the catalysis group. The most relevant results are presented as a part of the introductory Chapter 3 (Section 2.5). The study forms part of the european large-scale OCMOL (Oxidative Coupling of Methane followed by Oligomerization to Liquids) project.

Papers not included in this Thesis

CHA/AEI intergrowth materials as catalysts for the Methanol-to-Olefins process. R.L. Smith, S. Svelle, Pablo del Campo, T. Fuglerud, B. Arstadd, A. Lind, S. Chavan, M.P. Attfield, D. Akporiayed, M.W. Anderson*, Applied Catalysis A: General 505 (**2015**) 1-7.

Fossil Fuels: The Effect of Zeolite Catalyst Particle Morphology on Catalyst Performance in the Conversion of Methanol to Hydrocarbons. K.A. Łukaszuk, Pablo del Campo, A. Molino, M. Nielsen, D. Rojo-Gama, J.S. Martinez-Espin, K.P. Lillerud, U. Olsbye, S. Bordiga, P. Beato, S. Svelle*, Book Chapter in "Nanotechnology for Energy Sustainability", B. Raj, M. Van de Voorde and Y. Mahajan (Ed.) (**2017**) Wiley-VCH Verlag GmbH & Co. KGaA.

*corresponding author

List of conference contributions

Improved catalytic performance for the methanol to gasoline reaction over mesoporous one-dimensional ZSM-22 and ZSM-23 zeolites obtained by desilication Pablo del Campo, P. Beato, S. Svelle.

Oral presentation at the 14th Norwegian Catalysis Symposium, March 2-3 2014, Trondheim, Norway

Improved catalytic performance for the methanol to gasoline reaction over mesoporous one-dimensional 10-ring zeolites obtained by desilication. Pablo del Campo, P. Beato, S. Svelle.

Poster presented for poster symposium at the 16th Nordic Symposium on Catalysis, June 15-17 2014, Oslo, Norway

Operando time- and space-resolved X-ray diffraction for monitoring the methanol to hydrocarbons reaction over H-ZSM-22 zeolite catalyst in different conditions. Pablo del Campo, W. A. Slawinski, R. Henry, M.W. Erichsen, S. Svelle, P. Beato, D. Wragg, U. Olsbye.

Poster presented at the inGAP Closing Seminar, March 3 2015, Oslo, Norway

Influence of post-synthetic treatments on unidirectional ZSM-22 catalyst: Towards improved clean gasoline catalytic process. Pablo del Campo, P. Beato, S. Svelle.

Oral presentation at the 15th Norwegian Catalysis Symposium, December 3-4 2015, Bergen, Norway

Influence of post-synthetic treatments on unidirectional ZSM-22 zeolite catalyst: Towards improved clean gasoline catalytic process. Pablo del Campo, S. Svelle, P. Beato.

Oral presentation at the 11th Natural Gas Conversion Symposium, June 5-9 2016, Tromsø, Norway

Scope

The overall objective of this Ph.D. project was to improve the catalyst performance of unidirectional 10-ring ZSM-22 and ZSM-23 zeolite catalysts in the conversion of methanol to hydrocarbons with particular focus on catalyst lifetime, while maintaining the high selectivity towards the aromatic-free alkene fraction.

The work presented herein is based on previous investigations of the group, which showed that the MTH-shape selective ZSM-22 and ZSM-23 catalysts yield a product spectrum being rich in C_{5+} branched alkanes and alkenes and virtually without aromatics. Thus, they are potential catalysts to yield a product that might be suitable as aromatic-free gasoline after hydrogenation. However, the investigations outlined the lower stability towards deactivation of these catalysts in comparison with commercially used ZSM-5 catalyst.

The primarily objective of this work is to prolong the lifetime by introducing mesoporosity in the one-dimensional ZSM-22 and ZSM-23 zeolites by post-synthetic treatments based on organic aided desilication in alkaline solution and sequential acid washes. While the introduction of mesoporosity for more open structures has been extensively examined, very little work has been reported for 10-ring unidirectional zeolites. It was therefore decided to carry out an extensive investigation of the preparation and characterization of a large body of samples prepared by NaOH and surfactant aided desilication under different conditions. Over time, the study over ZSM-22 was extended to organic assisted desilication with TBAOH, with the aim of arriving at general observations and predictable procedure for mesopore introduction in one-dimensional 10-ring materials, which are very prone to pore blocking.

During the work, it was noticed that basic characterization (composition, textural properties, particle morphology and acidity) was not sufficient to completely understand the relationships between the zeolite properties and their MTH catalytic performance. It was therefore decided to employ advanced characterization FTIR spectroscopic techniques combined with sterically demanding probe molecules and accessibility/uptake measurements to overcome this challenging issue. Preliminary mechanistic studies were carried out to elucidate the evolution of the reaction mechanism. In addition, structure-activity/deactivation correlations brought by time- and space-resolved operando synchrotron methods were performed in order to provide new insights in the deactivation mechanism of the ZSM-22 catalysts for the MTH reaction.

During the Ph. D. project large amount of work was carried out related to the MTH reaction also with other catalysts. For this reason, discussions on the MTH reaction with additional catalysts are also included in this Thesis.

This Thesis is organized in five main chapters. The first chapter provide a background for the general aspects of catalysis and zeolites as acid catalysts. In the second chapter an overview of the energetic, technology and mechanistic aspects of the MTH reaction is given, with particular focus on previous work concerning the performance of one-dimensional catalysts in the MTH conversion. Chapter three provides a broad literature survey on the desilication methods developed to improve the catalytic properties of one-dimensional materials. Chapter four provides details on the experimental methods used. Chapter five presents a summary of the results of the work performed during this project. For a detailed discussion of the results the author encourages consulting the papers collected in the Appendix.

1. Introduction

1.1. Catalysis in general

The IUPAC defines catalysis as "*the action of a catalyst*" and a catalyst is defined as "*a substance that increases the rate of a reaction without modifying the overall standard Gibbs energy change in the reaction*". Catalysis is, thus, the chemical process of increasing the reaction rate by the action of a catalyst, which do not affect the thermodynamic equilibrium composition after the termination of the reaction. A catalyst is not consumed in the reaction and can be used for successive catalytic cycles.

This definition came immediately from the description brought by J.J. Berzelius in 1835 after systematically investigating the vague observations recorded until then, and classifying them as "Catalysis" for the first time [1]. From the XIX century, the application of catalysis have led to the optimization of most of the chemical and industrial processes, promoted by the astonishing growth of academic knowledge gained on the field [2]. Certainly, the increase in the demand of bulk chemicals for the growing mankind activities has been a driving force to the remarkable development of the catalytic processes. One significant stage in the development of catalysis happened when Haber and Bosch developed the process for the fixation of atmospheric nitrogen in the ammonia synthesis in 1909, motivated by the Chilean embargo on potassium nitrate as a nitrate source [3]. The increase of the catalytic industrial production had also notable events of the history as a backdrop. For instance, the demands on explosives based on nitric acid were extremely high during World War One [4]. In the first period of the XX century, catalysis was mostly developed for the industrial production of synthetic fuels by innovative technologies such as Fischer-Tropsch and FCC processes [3, 4], which, for example, contributed to the provision of fuel to the means of transport during World War Two. From the last period of the XX century the efforts were principally focussed on the petrochemical industry to cover the automotive demands and other catalytic processes related to the manufacturing of synthetic polymers. Nowadays, catalysis is involved in about 90 % of the current chemical processes, ranging from the production of fine chemicals to exhaust gas catalysts [2]. Furthermore, catalysis has gained significance owing to the recent society concerns on the industry impacts on the environment. The ultimate goal of the use of catalysts is to lower process investments and operation costs and also increase the selectivity

or rate of formation of one particular reaction product minimizing the formation of undesired by-products.

Currently, significant efforts are devoted to exploit the catalytic applications by synthesizing more selective and stable catalysts and expanding the knowledge towards a molecular-level understanding of the catalytic reaction, by the development of surface science or *in-situ/operando* characterization techniques, computational chemistry and reactor modelling. Efforts are ongoing to bridge the pressure and material gap to real conditions for practical applications.

The reason behind the extraordinary application of catalysts is based on the fact that the catalysed reaction proceeds more efficiently than the ordinary reaction. Figure 1.1a compares the potential energy diagram of a catalysed and non-catalysed reaction. A non-catalytic reaction will proceed only if reactants A and B collide with sufficient energy to overcome the activation barrier (E_a in Figure 1.1). The stronger the chemical bond, the higher the activation energy needed to break this bond. Formation of new bonds lowers again the energy curve as the product is formed. A catalyst increases the rate of a reaction by increasing the number of successful interactions between reactant particles and, thus, provides an alternative route for the reaction that is energetically favourable (needing a lower activation energy). It does it by forming an adsorption complex with the reactant with a transient bond, which stabilizes the transition state. Chemically, it changes the electron distribution and relative orientation in a way that favours the formation of new bonds, whereas the intermolecular bond of the adsorbed molecules is weakened and the bond breaking is facilitated [2]. A catalyst does not lower the original activation energy of the reaction. Note that the non-catalysed curve in Figure 1.1a is not affected, meaning that if particles collide with enough energy, they will follow the same way as without the action of the catalyst. However, the majority of the particles will react via the easier catalysed route.

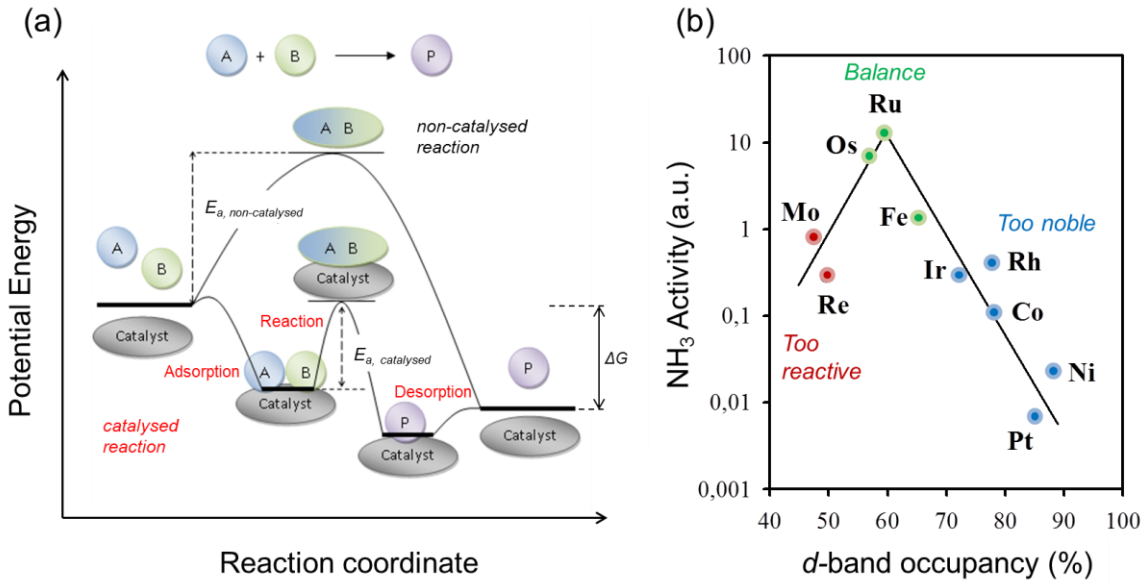

Figure 1.1. (**a**) Potential energy diagram of a non-catalysed (upper curve) and a heterogeneous catalysed (lower curve) reaction and (**b**) Volcano plot showing the catalytic activity of various supported metals for the ammonia synthesis. Adapted from [2].

The catalytic reaction is fully described as a cycle process in which the catalyst is recovered unaltered after acting in the reaction. The catalytic process consists of three main steps, *i.e.* adsorption, reaction and desorption, as illustrated in Figure 1.1a. The reactant molecules are first bond to the catalyst surface in a spontaneous adsorption reaction and the Gibbs free energy is lowered. In a second step, the reactants interact to form the product while they are bound to the catalyst paying an energy cost (E_a), which is significantly lower than that of the non-catalysed reaction. The last step is desorption of the product from the catalyst in an endothermic step, which brings the total Gibbs energy to the same level as that of the non-catalysed process. After desorption, the catalyst is in the same state as before adsorption and ready to catalyse the next reaction in the next cycle. This cyclic process is not always ideal since the interaction between the catalyst and reacting molecules can add some complexity. A proper energetic balance of all steps is required for successful catalytic process. In other words, for the completion of a catalytic reaction, this interaction should not be too weak, but also not too strong. This is the basis of the Sabatier's principle, illustrated in the so-called *volcano plot* in Figure 1.1b for the particular case of ammonia synthesis catalysed with different supported metals. The catalysts in the left region (red) can dissociate N_2 molecule, but the product nitrogen atoms bound very strongly, hindering them to desorb form the

catalytic surface and causing blocking. The reactant is weakly adsorbed on the catalysts to the right (blue) and they are unable to dissociate the N_2 molecule. All show lower catalytic activity than the optimal catalysts in the centre of the plot (green), with the highest ammonia production.

Catalysis can be classified in homogeneous or heterogeneous, depending on whether the catalyst is in the same or in a different phase as the reactants, respectively. There is a third discipline, named biocatalysis, which involve natural enzymes as very specific catalysts. The synthetic catalytic processes tend to mimic the chemistry of the enzymatic catalysis in order to reach the best shape selective properties and highest activity for a targeted process.

This work is focussed on heterogeneous catalytic processes in which reacting molecules interact in gas phase with a solid catalyst. More precisely, zeolites will be used as solid acid catalysts and the methanol conversion will be investigated in the gas phase.

1.2. Zeolites as heterogeneous acid catalysts

Zeolites are inorganic crystalline aluminosilicates containing channels and cavities. The zeolite structure is formed by a three-dimensional framework composed of tetrahedral TO_4 building blocks (where T are Si^{4+} or Al^{3+} tetrahedrally coordinated atoms) linked to each other through corner oxygen atoms. The arrangement of these building blocks gives rise to the different zeolite structures, which are characterized by the presence of well-defined channels and cavities of molecular dimensions, typically in the range of 4 to 12 Å, as schematically represented in Figure 1.2. The system of channels and cavities leads to solids with very high surface area and pores of different sizes. Accordingly, small molecules can enter these pores whereas larger molecules are sieved out. This concept is exploited to direct the chemical reaction towards the production of a desired product. Therefore, zeolites belong to the wider class of materials known as molecular sieves [5, 6].

One defining property of zeolites is their internal channel system, which is determined by the zeolite crystalline lattice structure. This system can be highly variable in pore size and degree of interconnection. The zeolite channel system is described by the number of tetrahedral units that form the ring, the internal ring diameter and the uni-, bi- or tri-directional arrangement of

channels, which can be interconnected or not. The number of connected O or T atoms determines the effective pore aperture of the zeolite channel. Zeolites are defined as small (8-), medium (10-), or large (12-membered-ring) pore materials, depending on the ring size of the largest channel. According to the IUPAC Commission on Zeolite Nomenclature, the different zeolite topologies are named with a three capital letters code [7]. As an example, MFI topology (ZSM-5, Silicalite-1) is a three-dimensional system formed by the intersection of 10-, 6- and 5-membered ring channels formed from arrangement of pentasil units, whereas TON topology (ZSM-22. Theta-1, NU-10) is composed of one-dimensional 10-ring channels (Figure 1.2). Both zeolites are medium pore materials. The rings are, however, not always perfectly symmetrical due to, among other effects, the strain induced by the bonding between sub-units or coordination of some oxygen atoms of the ring to cations within the structure. Additionally, zeolite channels may have small apertures or side pockets, which enlarge the internal volume.

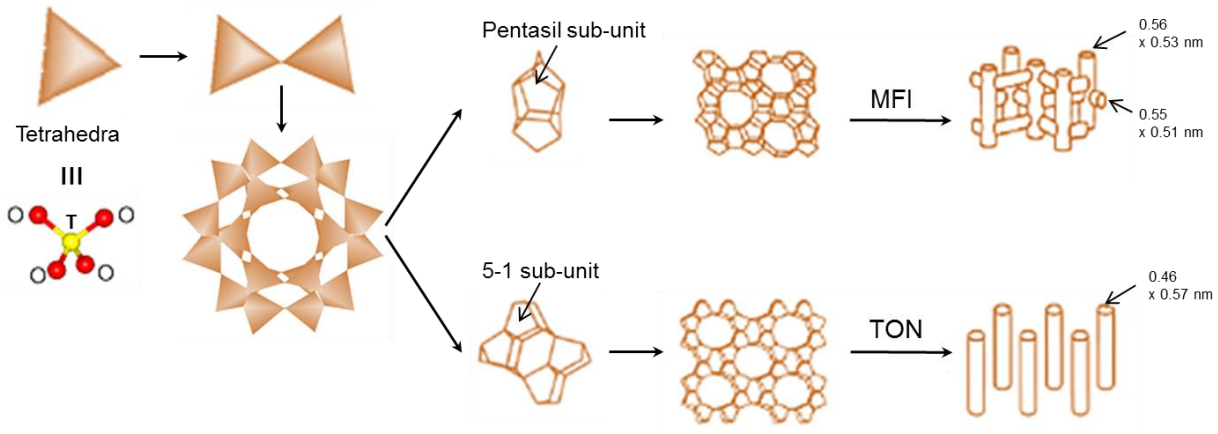

Figure 1.2. Structure of MFI- and TON- type zeolites and their internal micropore system. Adapted from [8].

Zeolites are naturally formed, but they can also be obtained by synthetic means [5]. It was the Swedish mineralogist A. F. Cronstedt who discovered the first mineral zeolite in 1756. He observed that large amounts of steam and water were released upon rapid heating of the mineral and decided to refer to this material as "boiling stone", or "zeolite" in Greek (*zeo* means "to boil" and *lithos* mean "stone"). However, since large mineable deposits of natural zeolites were unknown or hardly exploited, there was no significant commercial application of zeolites until synthetic procedures were developed. About 200 years after Cronstedt

discovery, the New Zealand-born R. Barrer successfully made the first synthetic zeolite in 1948 [5, 8, 9]. Around the same time, zeolites A (LTA), X (Al-rich FAU) and Y (Si-rich FAU) were discovered by Milton and Breck [9]. Zeolites were first commercialised in 1954 and used as desiccants and in NG drying by exploiting their hydrophilic properties (see below). New zeolites for novel uses appeared steadily through the 1960s, but the paramount eruption of new zeolite structures happened in the last two decades of the XX century [2]. Currently, approximately 200 zeolites have been identified, and about 40 naturally occurring zeolites are known [7]. Many synthetic zeolites have analogue structural natural materials, such as synthetic Mordenite. However, chemical impurities contained in natural zeolites, which are costly to remove, make synthetic zeolites more attractive for specific applications, in case that both natural and synthetic form of the same zeolite is available. In applications where purity is not so important, the cheapness of a natural zeolite may favour its choice.

The chemical composition of a zeolite is determined by the composition of its unit cell. The zeolite unit cell has the chemical formula $[xM_{2/n}O \cdot xAl_2O_3 \cdot ySiO_2 \cdot wH_2O]$ in the as-synthesized form [10], where M is the cation with valence n of an element which can belong to the group IA or IIA of the periodic table, or an organic cation, $(x + y)$ is the number of tetrahedras per unit cell and w are moles of water contained in the zeolite voids.

The Si/Al ratio calculated from the structure determines the zeolite properties to a large extent. On this basis, a classification of zeolites according to the silicon content has been established. Low silica (or, conversely, high alumina) zeolites have Si/Al ratios in the range of 1 to 1.5, whereas high silica (or low alumina) zeolites show Si/Al from ~ 10 to 200. Zeolites with Si/Al between these values are considered as intermediates. There are also pure silica molecular sieves with a Si/Al of theoretically ∞, such as Silicalite-1.

Once certain pore architecture has been synthesized, the second step necessary to obtain a zeolite catalyst is to introduce catalytically active sites within their pores, such as Brønsted acidity. In heterogeneous catalysis, an active site is the specific place on the surface of a catalyst where chemical reactions take place. Identification of the active site is essential to design better catalysts. The possibility to introduce active sites inside zeolite channels and cavities in a controllable manner and to identify the nature of these sites by the available characterization techniques makes zeolites unique solid catalysts when compared with metals, oxides and sulfides, in which the particular active sites are frequently unknown [11]. If the zeolite structure contained only SiO_4 tetrahedras (Figure 1.3a), it would be electrically neutral

and highly hydrophobic and, therefore, it would not have acidic character. Brønsted acid sites are introduced by isomorphically substituting a Si^{4+} ion by a trivalent metal cation, such as Al^{3+}. This creates a negative charge in the zeolite lattice, which can be compensated by organic or inorganic alkaline cations. Such zeolites still show no Brønsted acidity. This is generated by ion exchange of the cations by protons using NH_4^+ and di- or trivalent cations, followed by calcination. The proton is bonded to the oxygen atom connected to neighbour Si and Al atoms, resulting in a bridged hydroxyl group responsible for the Brønsted acidity (Figure 1.3c) [10, 11]. Theoretically, one proton should be introduced for each Al^{3+} in the zeolite framework. Thus, one acid site is generated for each Al atom. Accordingly, the larger the number of Al atoms (or the lower Si/Al ratio) the higher the potential number of acid sites. The Si/Al ratio is, thus, a good indicator of the acid site density of the zeolite catalyst. However, the Brønsted acid sites must have sufficient strength to produce appropriate catalytic activity, *i.e.* to donate or partially transfer a proton to the reacting molecule. The strength of the acidic sites depends, among other parameters, on the zeolite topology and the framework composition [12].

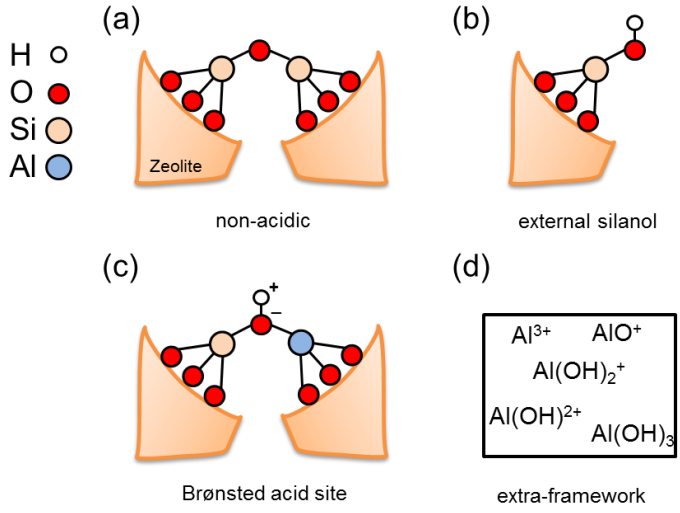

Figure 1.3. Schematic representation of the molecular structure of a non-acidic zeolite (**a**), a silanol site located on the external zeolite surface (**b**), a Brønsted acid site (**c**) and possible extra-framework Al species (**d**).

The total acid site density also depends on the number and type of extra-framework Al (EFAl) species, which may be generated during the activation processes of the zeolite or post-synthetic treatments [13]. The nature of these EFAl species remains mostly unknown.

However, some studies identified EFAl species as Al^{3+}, oxoaluminium AlO^{+}, $Al(OH)_2^{+}$ or $Al(OH)^{2+}$cations, or neutral species such as Al-OH species [12-16]. The active centres present as Al^{3+} EFAl species has strong Lewis character, *i.e.* they are capable to accept an electron pair from the reacting molecule. Such Lewis sites may modify the acid strength when interacting with surrounding Brønsted sites, which ultimately affect the catalytic properties of the zeolite [17, 18]. Other common structural defects encountered in zeolite catalysts are silanol (Si-OH) groups, formed due to the lack of chemical bonding between two vicinal tetrahedra located on the external surface (Figure 1.3b), or extra-framework Si (EFSi) species or silanol nests when a T-atom is missing [12-14, 19, 20].

The control of the chemical composition through the synthesis process is of paramount importance to tailor not only the number acid sites and acid strength but also the porous structure. Zeolites are usually synthesized under hydrothermal conditions following the steps [9, 10]: amorphous sources of silica and alumina are mixed together in an aqueous solution of a metallic cation source and SDA (template), usually in a basic medium. The resulting solution is well mixed and then heated at high temperatures in a sealed autoclave. The crystallization takes place after a certain induction period in which the product is still amorphous. After this time, crystallization starts by sequential steps of nucleation of the phases, followed by growth of the nuclei to form larger crystalline crystals. Gradually, all the amorphous material is replaced by approximately equal mass of zeolite crystals. The final crystals are recovered by filtration, washed with deionized water and dried at mild conditions. Harsh activation conditions have to be applied in order to remove the template from the framework.

Efforts have been devoted to synthesize materials containing other elements than silicon and aluminium [5, 7]. Similar crystalline structures but with additional tetrahedrally coordinated atoms, such as phosphorous, as well as ion-exchanged transition metals, can be synthesized. They belong to the generic group of zeotypes, which includes aluminophosphates ($AlPO_4$), silicoaluminophosphates (SAPO) and substituted aluminophosphates (MeAlPO and MeSAPO) molecular sieves.

1.2.1. Diffusion and shape selectivity in zeolites

Diffusion effects are decisive for the performance of zeolites as catalysts. When the size of a reacting molecule is similar to the zeolite pore dimensions, as is the case of acid catalysed hydrocarbon reactions, the diffusion of the reactant through the micropores to reach an active site, or the diffusion of the products out of the zeolite crystal, play a crucial role in the catalytic performance. Zeolites operate in the intra-crystalline regime, which is the more restricted regime of diffusion in porous materials. This implies that zeolites may be easily subjected to diffusion limitations if the pore system is restricted. Zeolites with channels of different pore dimensions cause molecules of different sizes diffuse preferentially through one or another channel. Differences in diffusivities are then used to increase the selectivity to a targeted product by control of the pore size of the zeolite catalyst [11], which brings to the concept of shape selectivity. The shape selectivity concept was first described by Mobil scientists in 1960 as the ability of zeolites to discriminate reactants, products and reaction intermediates based on molecular diffusion dominating over their thermodynamic equilibrium distribution [21]. Shape selective properties are important to avoid undesired side products.

Three types of shape selectivity are exhibited by zeolites [21, 22]:

- By reactant shape selectivity, reactant molecules are discriminated on the basis of their molecular size. Accordingly, molecules in the reactant mixture that are too large to enter the pore openings are prevented to reach the active sites in the zeolite crystal, whereas reactant molecules small enough can enter and react in the active sites. As an example, the linear *n*-butanol molecule is dehydrated over the narrow-pore A zeolite, but the more bulky isobutanol, having a larger cross sectional area, is not (Figure 1.4). By this principle, the two alcohols can be easily separated by choosing the adequate zeolite [3].

- Product shape selectivity occurs by discrimination among product molecules. Certain product molecules are too big to diffuse intact out of the zeolite pores. The alkylation of toluene by methanol over medium-pore H-MFI zeolite illustrates the product shape selectivity (Figure 1.4). The primary product of the alkylation reaction is not rich in *p*-xylene, since *o*- and *m*-xylenes are thermodynamically more favoured. However, H-MFI yields preferentially *p*-xylene because its diffusivity is about 1000 times faster than that of its isomers and, thus, it leaves the zeolite crystal more rapidly. On the other hand, *o*-

and *m*-xylenes are diffusion limited and remain within the zeolite pores to undergo further isomerization reactions, which result in increased yields of *p*-xylene [3].

- Transition-state selectivity is characterized by constraints imposed by the zeolite channel structure on forming molecules during the transition stage. Only certain products from reactions that involve transition-state complexes small enough or with the appropriate orientation to accommodate inside the pores are formed, as represented in Figure 1.4. In transition-state selectivity, neither reactants nor potential product molecules are prevented to diffuse in or out the zeolite crystal.

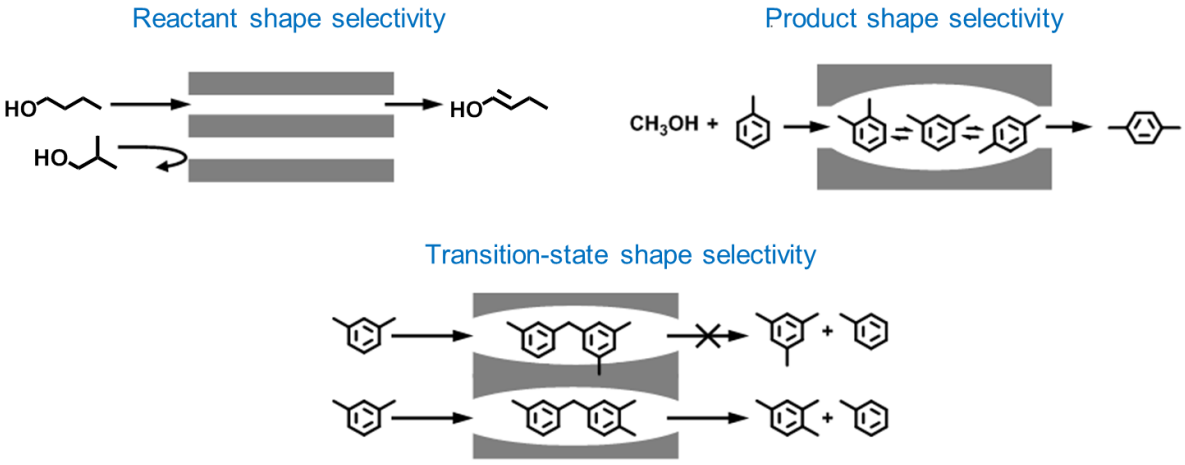

Figure 1.4. Examples of the three cases of shape selectivity in zeolites. Adapted from [21].

The intrinsic acidity combined with the tuneable porosity and molecular sieve properties make zeolites highly active and selective and, therefore, highly applicable in many targeted catalytic processes. Particularly, the successful application of zeolites as acid catalysts in large scale petrochemical and refining processes has been extensively demonstrated. A brief summary of the main breakthroughs in the history of heterogeneous catalysis is given based on literature [2, 3, 23]. The major advance in zeolite catalysis took place when FAU and MFI zeolites were added to acid clays and silica-alumina cracking catalysts in the FCC process to convert oil into fuels and chemicals in the mild-1960s. The use of zeolites allowed higher conversions and yields, but gasoline with low octane numbers. Few years earlier, Union Carbide successfully used Y zeolite in isomerization reactions. This catalyst was also applied to catalytic cracking of heavy oil fractions by researchers of Mobil Oil in 1962. However, it

was not until 1983 when they tested the first large-scale commercial cracking facility. Over time, the zeolite-based FCC technologies evolved towards the production of high-octane gasoline. Zeolites catalysts have been also applied in the conversion of methanol-to-hydrocarbons (MTH) since Chang and Mobil co-workers discovered that H-ZSM-5 catalyst selectively converted methanol into an aromatic-rich hydrocarbon mixture when operated at long contact times [24]. Further commercialization efforts based on Mobil Oil´s methanol to gasoline process have been limited by the energy market of that period [25]. A detailed description of the development of the MTH technologies is given in Chapter 2 (Section 2.2).

The application of zeolites as acid catalysts in hydrocarbon conversion reactions is becoming increasingly important in today´s oil industry. With today's increase of the fuel demand, the use of zeolite catalysts allows the transformation of gas oil and other oil distillate residues into more environmental friendly fuels, such as lead-free gasoline and diesel. By using zeolites, the energetic efficiency of a process is improved and emissions and hazardous wastes can be reduced. Zeolites are also extremely successful catalysts for organic synthesis in the production of fine chemicals and lower-cost synthetic plastics [2, 6]. Beyond catalytic applications, zeolites have also high performance in adsorption, gas separation and ion-exchange processes [2, 6, 26, 27].

1.3. Materials related to this work

Two one-dimensional 10-ring zeolites are the materials employed in the present work: ZSM-22 and ZSM-23. Figure 1.5 (top) shows simplified representations of the two one-dimensional channel structures, in which the accessible space inside the pores is represented in blue.

The crystal structures of ZSM-22 and ZSM-23 are closely related to each other due to their identical structural subunits. Both show orthorhombic crystal system. Both framework structures are made up by 5-, 6-, and 10-membered rings which are constructed from the same 5-1 secondary building units (see Figure 1.2). These subunits generate non-interconnecting one-dimensional 10-ring channels parallel to the short 5 Å axis [10]. The channel dimensions of ZSM-22 and ZSM-23 are practically the same. Nevertheless, there are small differences in the shapes and the openings, giving rise to different framework topologies with slightly different framework density. Main parameters are listed in Table 1.1.

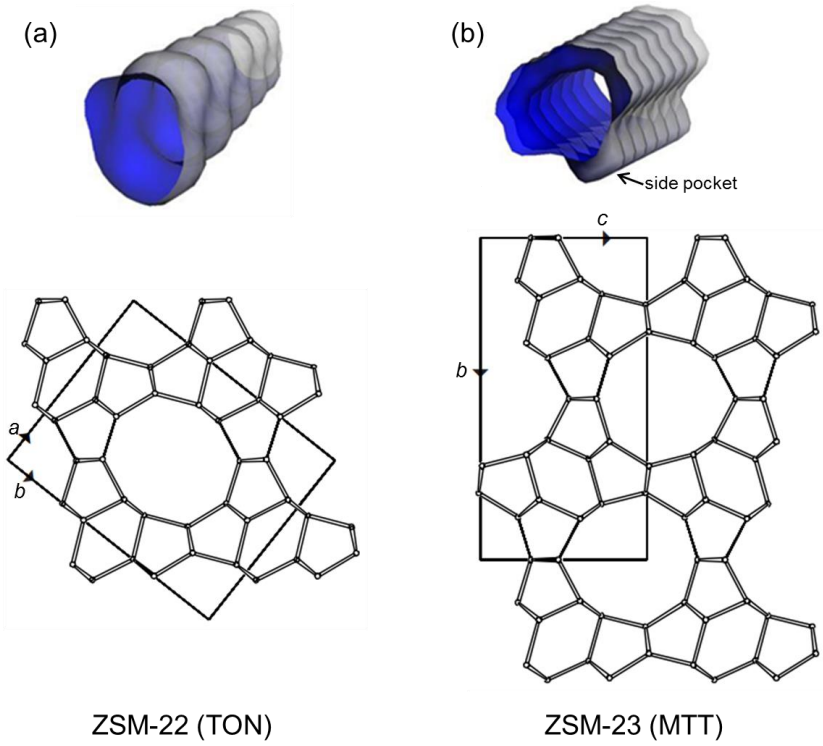

Figure 1.5. Schematic representation of the channel systems (**top**) and projection of the framework structure (**bottom**) of the ZSM-22 (**a**) and ZSM-23 (**b**) zeolites, from IZA web site (http://www.iza-structure.org/databases/ModelBuilding/TON)

- ZSM-22 has a TON topology. The 10-ring channels of TON are elliptical and slightly zigzag in shape, with dimensions 5.7 x 4.6 Å. The projection of the structure of the cell parallel to [001] (along the shortest *c* direction) is shown in Figure 1.5a (bottom). There are two such 10-membered ring channels per unit cell. The maximum diameter of a sphere that can be included inside the largest channel is 5.71 Å. TON has a framework density of 19.7 T-atoms per 1000 $Å^3$ [7, 28, 29].

- ZSM-23 has a MTT topology. The tear-drop shaped non-connected 10-ring channels of MTT show a slight side pocket and dimensions 5.2 x 4.5 Å. The framework structure of ZSM-23 can be constructed by repeated twining of the ZSM-22 framework after (110) [30-32]. The projection of the structure of the cell along the shortest *a* direction is shown in Figure 1.5b (bottom). The small side pocket makes the maximum diameter of a sphere that can be included inside the channel increase to 6.19 Å and the framework density slightly larger than that of TON, with 20.1 T-atoms per 1000 $Å^3$ [7, 30, 33].

Table 1.1

Main parameters of the one-dimensional ZSM-22 and ZSM-23 zeolite structures.

Structure	Topology	10-ring channel system			Max. diameter[1]	Framework density
		Dimensions	Shape	Side pocket		
ZSM-22	TON	5.7 x 4.6 Å	elliptical	none	5.71 Å	19.7 T/1000 Å^3
ZSM-23	MTT	5.2 x 4.5 Å	tear-drop	very small	6.19 Å	20.1 T/1000 Å^3

[1] Maximum diameter of a sphere that can be included in the largest channel.

The templates used in the synthesis gel of one-dimensional materials usually consist of long hydrocarbon chains with polar species at both chain ends. These templates act as structure directing agents and direct the crystallization preferentially towards similar needle-like morphologies for both ZSM-22 and ZSM-23 [29, 34-37]. This can be explained by a directing effect of the template, minimizing the surface energy of the intermediates as described in the mechanisms of crystal growth proposed by Cundy and Cox [9].

Only one batch ZSM-22 was in house synthesized, and ZSM-22 and ZSM-23 zeolites were provided from a commercial vendor. All zeolites were calcined, extensively characterized and submitted to various post-synthetic treatments with the aim to introduce additional mesoporosity. The protonated zeolites were catalytically tested in the MTH reaction.

2. The Methanol-To-Hydrocarbon Reaction

2.1. Energetic perspectives

Crude oil remains as the present world's leading source for both liquid fuels and raw materials, accounting for about 33 % of the global energy consumption (Figure 2.1a) [38]. However, current estimates, based on the up-to-date proved size of oil reserves (some 1700 thousand million barrels) and the increasing demand of energy needs, predict that the global oil reserves would last for 50.7 years at the current rate of consumption [38]. This, however, also depends on the development of new crude oil extraction technologies and unexploited wells. This scenario calls for new feasible alternative energy sources to cover the global demand, such as natural gas, coal, biomass, atomic energy, hydrogen, urban waste (for district heating) or even recycled CO_2 [39]. It has been estimated that current sources of liquid fuels will not have the capacity to cover all demand in 2020 [40] (Figure 2.1b). However, sources for liquid fuels are currently over covering this need. Nevertheless, alternative carbon sources or new technologies will be important for covering the demand of fuel needs.

Syngas (CO and H_2) can be produced from methane (NG) or coal. Methanol is currently synthesized almost exclusively from fossil-fuel-based syngas using $Cu/ZnO/Al_2O_3$-based catalysts [25], but it can also be obtained from biomass or by direct oxidative conversion of NG [2]. The MTH technologies can potentially fill the gap for an alternative route to produce petroleum-related and raw chemicals from C_1 sources, which are considerably more abundant than crude oil. Despite the fact that coal reserves may last for more than one century and coal remain the dominant energy source in Asia [38], the socio-economical, safety and environmental adversities associated with coal extraction from mines makes coal not the best fossil fuel alternative [39]. Biomass technologies still need to be developed to be considered a real alternative to produce methanol. The economics to produce, for instance, agriculture-based ethanol to replace fossil fuels is still not favourable [39]. Natural gas, hence, represent the most convenient alternative source of methanol [25, 41].

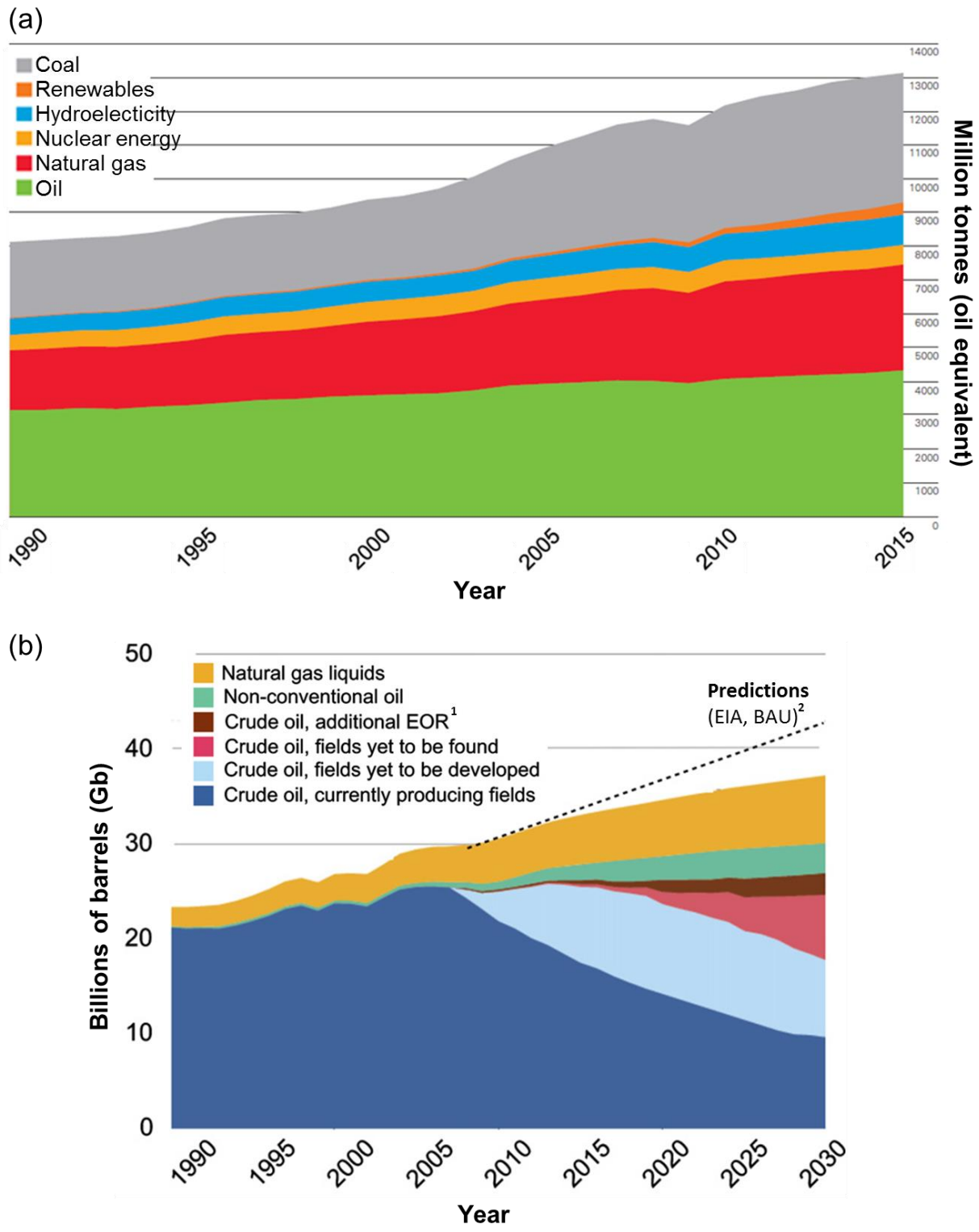

Figure 2.1. World primary energy consumption in million tones oil equivalent from year 1990 to 2015 (**a**) and projected world liquid fuels demand and supply (**b**). Adapted from [38] and [40], respectively. [1]Enhanced Oil Recovery, [2]Energy Information Administration, Business as Usual.

Nowadays, less than a quarter of natural gas produced annually is burned in flares. As shown in Figure 2.1a, the remainder natural gas accounted for a considerably 23.8 % of primary energy consumption in 2015. The estimated natural gas total proved reserves are comparable but some larger to that of oil (52.8 % at the current rate) [38], also dependent on the new advances in exploration and recovery methods. As long as natural gas remains abundant, it appears reasonable to use it as methanol source. Also, the potential greenhouse effect of methane can be reduced. Regarding the process efficiency, natural gas treatments do not give solid residues and it is economically favourable to extract and transport as well as flexible in use. On the other hand, its storage is not easy.

Methanol from natural gas-based syngas does not reduce the current dependence on non-renewable fossil fuels. This implies that at some point, the synthesis of methanol will have to turn to alternative renewable technologies, such as the reductive conversion of CO_2 recycled from industrial effluents and exhausts [39]. Interestingly, the use of atmospheric CO_2 itself offers a feasible long-range solution to produce hydrocarbons via methanol, which would eventually replace fossil fuel technologies and alleviate global warming [39].

2.2. Development of MTH technologies

The methanol catalytic conversion into hydrocarbons was discovered by Chang and Mobil co-workers in the 1970s. They showed that H-ZSM-5 yielded an aromatic rich hydrocarbon mixture terminated at C_{10} when operated at long contact times [42]. This opened a new era of extensive research interest and commercial efforts for the MTH technologies, which lasts until today [24, 25]. The Mobil´s methanol-to-gasoline (MTG) process was firstly commercialised on New Zealand during the oil crisis in the 1980s, with a high-octane gasoline production over 600 000 ton/year, but later shut down due to the subsequent drop in the oil price relative to that of methanol [24, 43]. Around the same time, the TIGAS process, also based on H-ZSM-5, was demonstrated on pilot scale [44]. By combining methanol and DME synthesis in a single reactor unit and using high pressures and moderate temperatures, the conversion of syngas towards high-octane gasoline was increased. However, this process was never further developed due to the global energy market status. Later on, more attention was paid to the methanol-to-olefins (MTO) reaction for production of light olefins (ethene and propene) from

methanol. The UOP/Norsk Hydro MTO technology was proven in a demo plant in 1995 [45]. This process utilizes the H-SAPO-34 catalysts in fluid bed operation to produce a selective mixture of ethene and propene from methanol. Lurgi developed the industrial process for the production of propene from methanol (MTP) over H-ZSM-5, which was demonstrated in a Lurgi/Statoil demo plant and is nowadays commercialized in China [46]. This process operates at high temperatures and rather low pressures in a parallel fixed-bed setup with feed injection between beds and product recycle to maximize the yield of propene. Mobil also developed a fluidized bed process producing either gasoline or light alkenes over H-ZSM-5 depending on process conditions. The produced alkenes could also react to produce gasoline, lubricants and distillate fuels in the Mobil's olefin-to-gasoline and distillate process (MOGD) [41]. Currently, intense commercialization efforts for MTH technologies are ongoing [41].

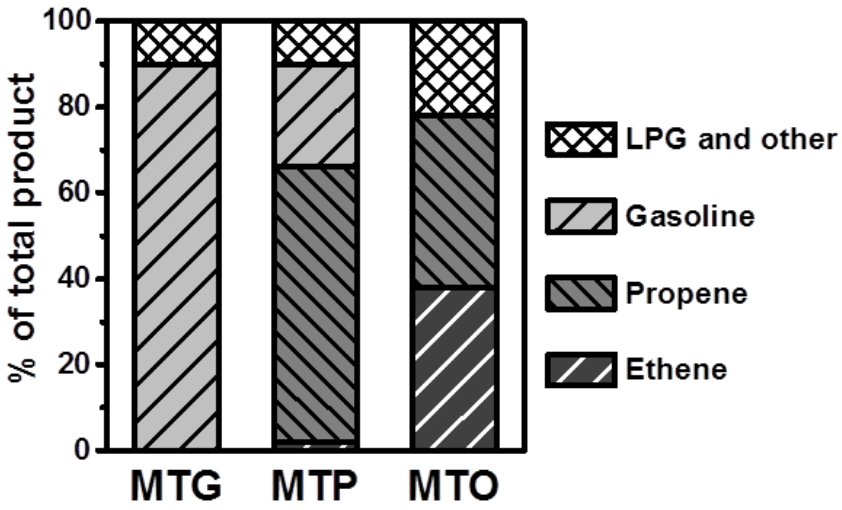

Figure 2.2. Product fractions produced by the MTG, MTP and MTO processes, from [41].

By adjusting the process conditions and choosing a suitable zeolite catalyst, the MTH effluent distribution can be varied. Therefore, specific MTG, MTO or MTP processes can be developed [25]:

- To produce a quality gasoline, product molecules must be allowed to diffuse through channels of at least 10 T-atoms. Two zeolites are outlined as MTG catalysts. H-ZSM-5 is the preferred zeolite catalyst to produce high-octane gasoline. H-ZSM-5 yields a product stream typically rich in gasoline-range hydrocarbons with aromatics (Figure 2.2) at intermediate reaction temperatures (320-420 ^{o}C) and high pressure. H-ZSM-22

catalytically behaves as a 10-ring zeolite, but with an effective pore size slightly smaller than H-ZSM-5 and one-directional channel system. It yields a product effluent mainly composed of aromatic-free C_{5+} branched alkanes and alkenes, as an effect of its unique shape selective properties. Despite this catalyst has not been commercialized yet, owing to its rapid deactivation, the H-ZSM-22-based MTG product might be suitable as environmental friendly gasoline production.

- The archetype MTO catalyst is the zeotype H-SAPO-34. The CHA topology of H-SAPO-34 is responsible of the product distribution. While aromatic intermediates can be generated in the large cavities of H-SAPO-34, the narrow pore apertures do not allow molecules larger than C_4 to diffuse out of the crystal. Thus, aromatics react further to smaller hydrocarbons before they can diffuse out. As a result, a product stream rich in ethene and propene is selectively obtained (Figure 2.2). Zeolites with 10-ring channels can also be tuned to more olefin production. Bhan *et al.* proved that by increasing the crystal size of H-ZSM-5 the selectivity towards light olefins can be enhanced [47].

- By using high temperatures and low pressures, H-ZSM-5 can catalyse the MTH reaction to produce propene (MTP) with some by-product LPG-type fuel and lower gasoline content, as shown in Figure 2.2.

2.3. Evolution of the reaction mechanisms

A MTH-based catalyst can transform methanol into hydrocarbons in an apparently single step or black box. Far from it, the extensive research carried out in the last decades has shown that the MTH mechanism is indeed very complex, but it can be understood by applying a number of approaches. Isotopic labelling studies, single reaction kinetics and novel computational and experimental methods, such as advanced spectroscopic techniques, gave breakthrough insight into the reaction and deactivation mechanisms [25]. The MTH mechanisms are difficult to determine owing to the heterogeneity of the adsorption and the transport limitations imposed by the pore system of the zeolites [24]. However, it is the same pore system that allows a rational study of the reaction. By choosing the appropriate zeolite catalyst and technique, the MTH reaction could be described in detail [25].

The MTH reaction is highly exothermic. Generally, it proceeds via first alkene formation from an equilibrium mixture of methanol and DME. The formed alkenes react further to a mixture of higher alkenes, alkanes and aromatics in the so-called hydrocarbon pool (HCP). It has been demonstrated that the MTH reaction is autocatalytic [48]. This means that small amount of products can catalyse the reaction and the rate of conversion of this route is substantially higher than the rate of direct C–C bond formation. Last findings demonstrated that the MTH reaction takes place over hybrid organic-inorganic sites, where alkene and/or aromatic molecules act as autocatalytic species within the catalyst pores in the so-called dual cycle mechanism [25]. The main mechanistic findings are listed below and the relevant proposals are shown in Figure 2.3.

- Chen and Reagan proposed the autocatalytic nature of the MTH reaction [48].

- Dessau an co-workers co-fed ^{13}C labelled methanol with ^{12}C-alkenes and -arenes over H-ZSM-5 and proposed that the MTH reaction proceed via sequential alkene methylation/ cracking steps [49, 50], as illustrated in Figure 2.3a. The initial alkenes come from C–C coupling reactions, but once trace impurities of C_{2+} are formed, they are capable to initiate the autocatalytic reaction. Aromatics were proposed as final products resulting from hydrogen transfer reactions and not act as active centres for product formation.

- Langner [51], Mole and co-workers [52, 53] carried out co-feed experiments by reacting cyclic alcohols and isotopic labelled aromatics together with methanol. The expeiments supported Dessau's indirect mechanism for alkene formation, but involving also methylated cyclic or aromatic as intermediates.

- The MTH mechanism was in part clarified when Dahl and Kolboe co-fed supposed intermediates (ethene and propene) and ^{13}C labelled methanol over the zeotype H-SAPO-34, which yields predominantly C_2-C_4 alkenes [54-56]. The experiment showed not only singly and triply, but also doubly ^{13}C labelled propene. This suggested a more complex picture than a simple consecutive mechanism. The HCP concept, consisting in fragments of $(CH_2)_n$ which react repeatedly with methanol to form other intermediates or products (Figure 2.3b) was proposed. The stoichiometry of the HCP was not specified.

- The groups of Haw and Kolboe simultaneously identified polymethylbenzenes (PMBs) as principal HCP species in H-SAPO-34 [57-59]. Later studies supported the importance of PMB intermediates in H-Beta zeolite [60, 61]. Additional studies by Hunger *et al.* evidenced the HCP mechanism in H-ZSM-5, H-SAPO-34 and H-SAPO-18 catalysts [62-64].

- Steady-state isotope transient experiments over H-ZSM-5 catalyst showed that ethene and lower PMBs with up to four methyl substitutes displayed similar contents of ^{13}C, whereas the higher alkenes (C_{3+}) were more reactive for the ^{13}C methanol than the PMBs [65, 66]. The dual cycle concept, by which the HCP proceeds through two interconnected mechanisms running in parallel (Figure 2.3c), was proposed. In the aromatic or arene cycle, the aromatic molecules get methylated until higher PMB are formed, which either leave the catalyst pores or split to lighter alkenes (mainly ethene) by de-alkylation reactions. In the alkene or olefin cycle, alkenes are successively methylated up to a certain size and leave the pores or are cracked down to lighter alkenes, similarly as proposed by Dessau [49, 50], however, with negligible contribution of the alkene cycle to ethene formation. Both cycles are connected through cyclization and hydrogen transfer reactions.

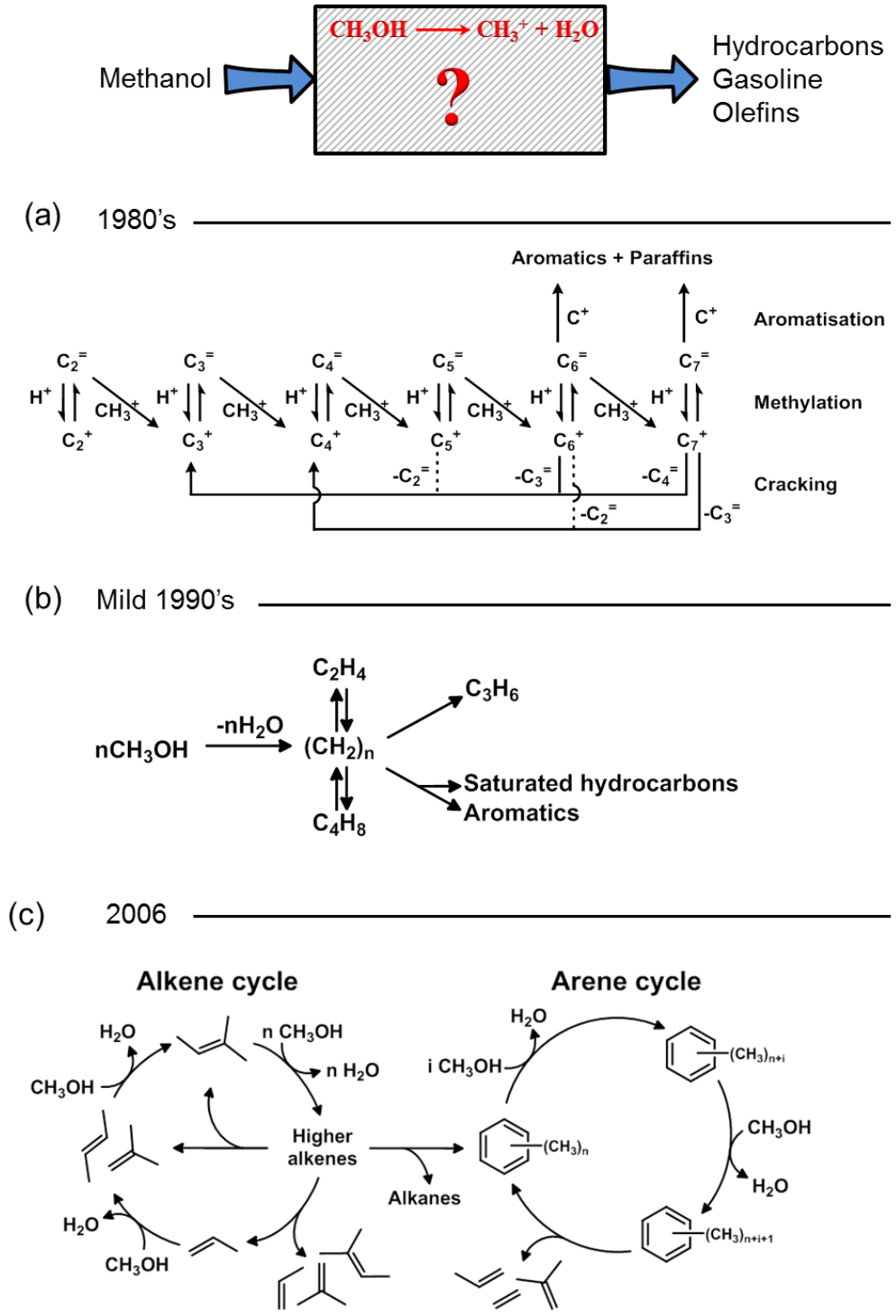

Figure 2.3. Evolution of the MTH mechanisms. Schemes of the (**a**) methylation/cracking mechanism proposed by Dessau, adapted from [49], (**b**) hydrocarbon pool mechanism proposed by Dahl and Kolboe, adapted from [55] and (**c**) dual cycle mechanism proposed by Svelle and co-workers, reproduced from [67].

The dual cycle mechanism is the currently accepted mechanism for the MTH reaction. It shows that not only aromatics, but also alkenes can act as reaction centres for the autocatalytic reaction. The relative importance of each cycle as well as the structure of the intermediates

depend on the catalyst structure and process conditions [25]. It was shown that medium pore-sized zeolite catalysts favoured the alkene cycle and only accommodated low substituted PMBs, whereas in catalysts with pores or cavities large enough to accommodate larger PMBs, the arene cycle is more favoured [68-72]. However, it has also been suggested that low reaction temperatures and high pressures may favour the alkene cycle over large pore zeolites [73, 74] as well as catalysts with low acid strength [67, 75].

The implication that aromatics only participate in one of the cycles and that the reduction of the catalyst pore size imply a lower contribution of the arene cycle, raised the idea of whether it was possible to suppress the aromatic cycle by choosing the appropriate catalyst architecture. This was addressed using the narrow-pore one-dimensional ZSM-22 zeolite as catalyst. Steady-state isotopic transient studies demonstrated that H-ZSM-22 strongly favours the alkene cycle, while the formation of aromatic products from methanol through the arene cycle was virtually suppressed [76-79]. This resulted in low yield of ethene, virtually no aromatics and high selectivity towards branched C_{5+} hydrocarbons. The zeolite pore structure was the dominant parameter to force the operation of only one of the cycles.

The mechanism is more complex for catalysts that allow the operation of both cycles. In this sense, Bhan and co-workers introduced a descriptor by which the relative rates of propagation of the alkene and arene cycles that can operate in MFI catalyst can be described [80]. Assuming that ethene was formed essentially from the aromatic cycle and 2-methylbutane + 2-methyl-2-butene were preferentially from the alkene cycle, the ratio between them was used to describe the relative propagation of the cycles. The influence of temperature, co-feeding and particle size was also studied and related to particular properties of the catalyst [47, 81].

2.4. Shape selectivity in MTH

The product distribution of the MTH reaction is strongly controlled by the shape-selective effects of the diverse zeolite topologies [25], although the effect of the Si/Al ratio, acid site density and strength or crystal size should not be discarded [76]. The ideal study should be focussed only in the pore topology while maintaining the rest of the properties uniform. Reactant shape selectivity will not influence the MTH reaction, since methanol is small

enough (3.6 Å) to enter the pores of all the MTH-based zeolites. However, both product and intermediate shape selective effects affect the effluent distribution.

The size of the larger product is controlled by the dimensions of the channel by product shape selectivity. Figure 2.4 shows a correlation between the cross-section area of the largest channel of a series of zeolite catalysts and the kinetic diameter of the largest product formed in appreciable amounts in the MTH reaction over each material. Small pore 8-ring openings limit the products to linear alkenes. Medium pore size channels of 10-ring zeolites may limit the effluent products to either branched alkenes or aromatics, depending on small size variations. Smaller 10-ring channels produce branched alkenes and alkanes, while larger channels yield mainly methylbenzenes. Zeolites with 12-ring channels provide essentially no product shape selectivity and, hence, the heaviest methylated benzene (HexaMB) is the largest product.

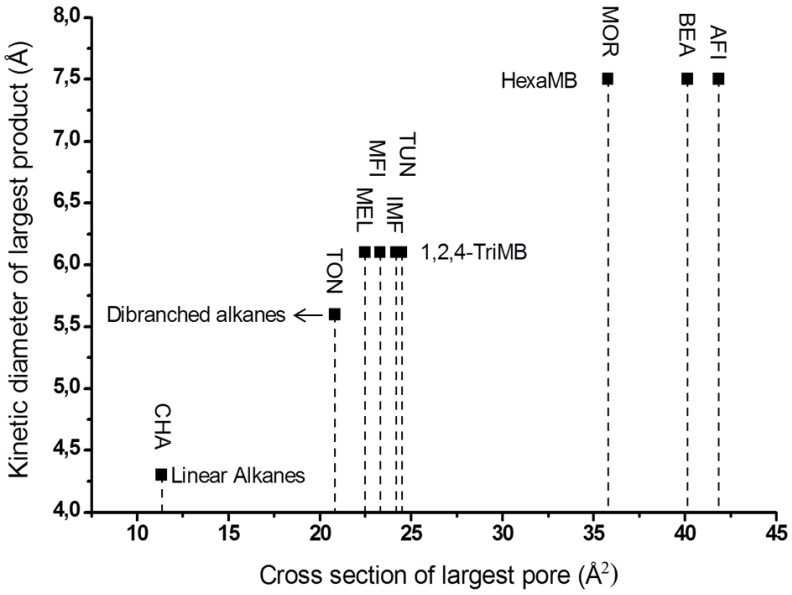

Figure 2.4. Kinetic diameter of the largest product vs. cross section of the largest pore. Reproduced from [76].

Cavities and side-pockets present on the main channels, as well as channel intersections of three-dimensional structures, also affect the product distribution, as they provide larger space where reactions may occur. Changes in product selectivity induced by these parameters make the discrimination between different shape selective effects complex [21, 76]. The selectivity over small pore zeolites is restricted by product-shape selectivity. However, the product

selectivity over medium (10-ring) and large (12-ring) pore zeolites is found to be further restricted by intermediate shape selectivity [76]. Zeolites which large pores and/or extra space favour the more space-demanding hydride transfer reaction, by which the aromatics and alkanes are produced from higher alkenes. As the size of the zeolite structure decreases to medium pore sizes and without alterations, the arene-based reactions and alkene-based cracking reactions are less favoured, whereas methylation reactions, which are less space-demanding, are increasingly favoured. Hence, the product spectrum ranges from aromatics and alkanes rich mixture to a product rich in C_{5+} alkenes [76]. The different product distribution as a result of slight variations in the same pore sizes is illustrated with the three-dimensional ZSM-5 and the one-dimensional ZSM-22 10-ring structures (Sections 2.2-2.3).

The influence of the cavities or side-pockets is illustrated with the comparison of two one-dimensional 10-ring structures: H-ZSM-22 (TON) and H-EU-1 (EUO), which contains large 12-ring side cavities that provide significantly more space than the 10-ring channels. Product distributions containing larger products than would be expected based on the medium sized channel size of EUO were reported [78]. The involvement of the more spacious pockets open to the external surface of the H-EU-1 crystal allows the formation of aromatics otherwise prevented in the small unmodified 10-rings. It should be mentioned that the H-EU-1 crystals employed in the study were smaller than H-ZSM-22 crystals, so reactions occurring on the external surface area may be more pronounced for H-EU-1.

2.5. Challenges of one-dimensional zeolites

Although aromatics boost the gasoline octane number, there are limits on the aromatic content in gasoline fuels, since they can cause cancer [82]. While the carcinogenic aromatics content of low-silica H-ZSM-5-based MTG gasoline (23-35 vol%) is not particularly high compared to standard gasoline [41], it is still higher than desired. An environmental friendly gasoline consists of branched alkanes of 5-10 carbon atoms and is free of aromatics [82]. Teketel *et al.* firstly demonstrated that it was possible to obtain a product virtually without aromatics under appropriate conditions over H-ZSM-22 (TON) catalyst [79]. The H-ZSM-22-based MTG product, being rich in C_{5+} aromatic-free branched alkanes and alkenes (Figure 2.5) meets the

fuel requirements and might be suitable as high octane gasoline after hydrogenation. Alternatively, the C_2-C_4 alkene rich product might be utilized as an alkylation feedstock.

The potential of 10-membered ring one-dimensional zeolites as catalysts for MTH reside in their ability to produce environmental friendly gasoline [41, 78, 79]. Other unidimensional 10-ring zeolites closely related to the ZSM-22 structure with similar catalyst properties were also investigated as MTH catalysts [78]. Figure 2.5 shows the C_2-C_4, C_{5+} aliphatic and aromatic yields for H-ZSM-22 (TON), H-ZSM-23 (MTT), H-EU-1 (EUO) and H-ZSM-48 (MWW) zeolite catalysts versus methanol conversion together with the pore system of each zeolite. The small side pocket of MTT zeolite did not affect the product distribution. On the other hand, the slightly larger channel diameter of the MRE structure strongly affected the product distribution and notable amount of aromatics were observed in the C_{5+} fraction, in agreement with previous discussion (Section 2.4). The effluent of this material showed significantly lower selectivity for C_{5+} hydrocarbons but appreciable formation of aromatics. Therefore, H-ZSM-22 and H-ZSM-23 are suitable catalysts to produce environmental friendly gasoline.

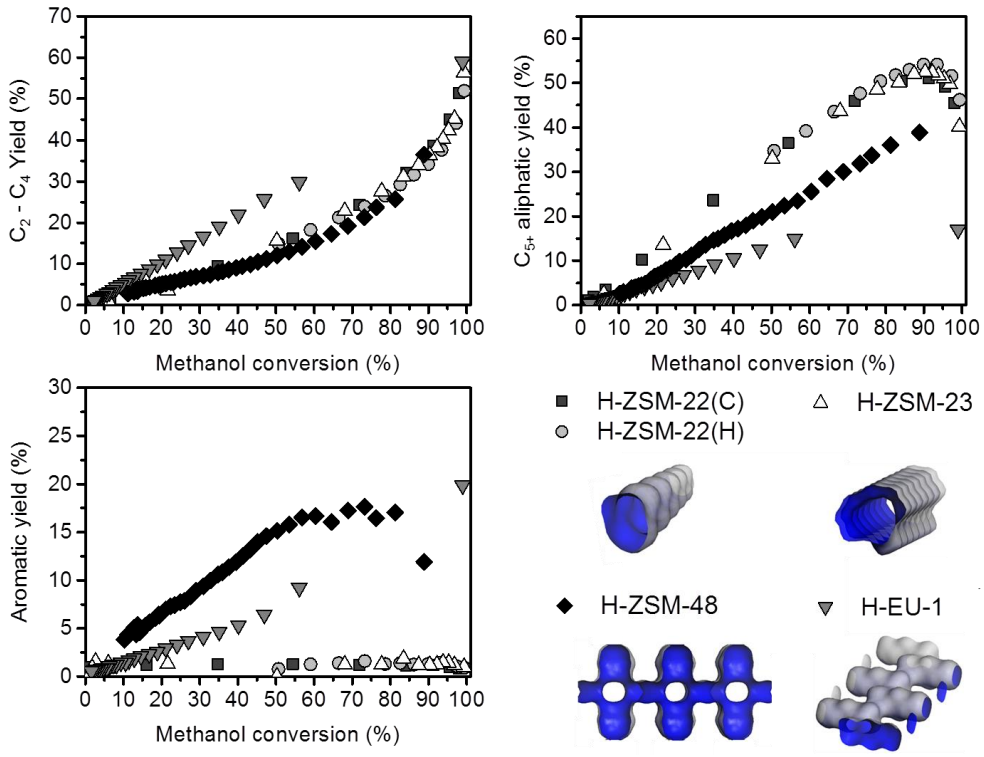

Figure 2.5. Yields of various hydrocarbon products as a function of methanol conversion at 400 ^{o}C and WHSV = 2 $gg_{cat}h^{-1}$ and illustrations of the pore systems for the one-dimensional catalysts. For the H-ZSM-22 catalysts, "C" and "H" denotes commercial and in house synthesized, respectively. Adapted from [41].

The major drawback associated with one-dimensional 10-ring zeolites is the low activity for methanol conversion as well as the limited lifetime or rapid deactivation by coking, compared to commercially used zeolite catalysts, such as H-ZSM-5 [25, 78, 79, 83]. Teketel *et al.* demonstrated that high contact times or low weight hourly space velocities (WHSV) (< 4 $g_{MeOH}g_{cat}^{-1}h^{-1}$) were required to obtain appreciable conversion of methanol over H-ZSM-22 at 400 ^{o}C [79]. Li *et al.* similarly found that a WHSV of 1 $gg_{cat}^{-1}h^{-1}$ was needed to achieve certain conversion at 450 ^{o}C [84, 85]. The low activity of H-ZSM-22 was further explored by Janssens *et al*. using an autocatalytic deactivation model [86]. They found that the critical contact time (*i.e*. the contact time needed to launch the autocatalytic MTH reaction) was much higher for H-ZSM-22 than for H-ZSM-5, meaning that H-ZSM-22 necessitates longer time for the autocatalytic reaction to dominate the reaction rate. Similar consideration can be drawn for H-ZSM-23, which displayed a critical contact time similar to H-ZSM-22 under the same operation conditions [41, 87]. Screening tests of all these catalysts showed that WHSVs below 4 $gg_{cat}^{-1}\,h^{-1}$ were required to achieve initial conversions near 100 %. An increase in space velocity resulted in more rapid deactivation, in agreement with previous studies [79, 87]. The low lifetime of one-dimensional catalysts is evidenced in the methanol conversion versus time of stream plot shown in Figure 2.6.

The total methanol conversion capacity (*i.e*. the total gram amount of methanol converted into hydrocarbons per gram of catalyst before complete deactivation) serves as quantitative comparing parameter of the MTH catalytic performance, given that the acid site density of the catalysts is similar. Teketel *et al.* showed that a maximum conversion capacity for H-ZSM-22 of 12 $g_{MeOH}g_{cat}^{-1}$, with a WHSV of 2 $gg^{-1}h^{-1}$ [79]. While this value was lower than the conversion capacity of the commercially used H-SAPO-34 catalyst [88], the lower amount of acid sites in H-ZSM-22 means that the conversion capacity per acid site in this catalyst was higher. However, the H-ZSM-22 conversion capacity was estimated in the order of one twentieth of that of H-ZSM-5 with similar acid site density [86].

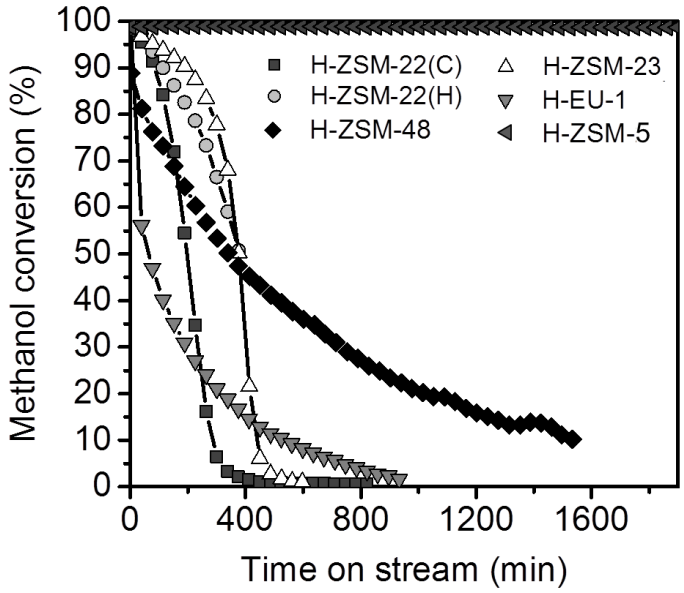

Figure 2.6. Comparison of the methanol lifetime between the one-dimensional zeolite catalysts and the commercially used H-ZSM-5 at 400 ^{o}C and WHSV = 2 $gg_{cat}h^{-1}$. Reproduced from [41].

The rapid deactivation of the one-dimensional catalysts is a direct consequence of their restricted channel structure. The channels of the zeolite can be considered tunnels inside the catalyst crystal within which small molecules may diffuse in and out. It has been mentioned that the shape and connectivity of these tunnels play a major role in determining which products are actually formed, but also influence the stability against coking. Figure 2.7 shows that in the case of zeolites with three-dimensional (3D) pore architecture, the tunnels intersect each other and the number of pore openings multiplies, making the structure more resistant against pore blocking. In one-dimensional zeolites, however, the channels go from one side to the other without crossing, so the diffusion of molecules throughout the crystal is limited and coke deposits can easily block the pores and deactivate the catalyst.

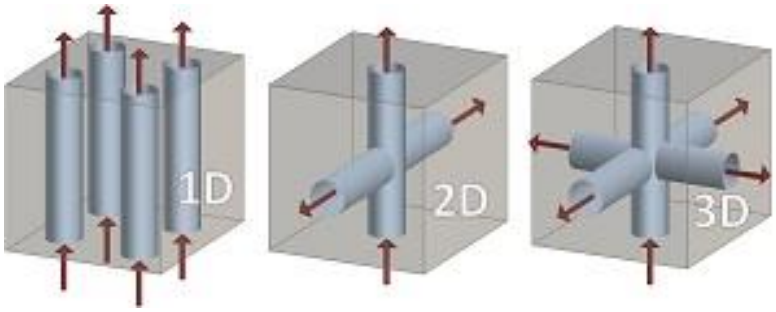

Figure 2.7. Schematic representation of the dimensionality of zeolites.

The mechanism of deactivation during the MTH reaction has been recently reviewed by Olsbye *et al.* [83]. It is assumed that coke deposits are the main cause of catalytic deactivation in MTH either by pore blocking or poisoning the active sites. However, the autocatalytic nature of the MTH reaction makes deactivation studies a very challenging task. Firstly, they are to be carried out at full initial conversion to ensure that the autocatalytic reaction is dominating methanol conversion. Secondly, species which are active intermediates (such as PMBs) in one topology (CHA) may be deactivating species in another topologies (TON, MTT) [25]. Olsbye *et al*. employed two different approaches to model the deactivation behaviour of the MTH reaction: First, an autocatalytic deactivation model was proposed, assuming that deactivation is proportional to methanol conversion [89]. It was found that the slope of a linear plot of catalyst lifetime to 50% conversion versus contact time characterized the deactivation of H-ZSM-22. Secondly, it was assumed that coke was only formed by the reaction between methanol and aromatic species [86]. Recently, Lercher *et al.* compared the MTH reaction over H-ZSM-5 in plug-flow and back-mixed reactors and hypothesized that the evolution of coke species depends on the position of the catalyst particle in the catalytic bed [90]. In the early stages of the MTH reaction, the H-ZSM-5 zeolite deactivated fast by blocking of individual Brønsted acid sites due to oxygen-containing surface species. These species were further transformed to aromatic compounds and deactivation proceeded by forming large coke species that blocked the catalyst pores.

The shape of the deactivation curve can be correlated with the mode of coke formation. It was proposed that the typical *S* shape of the MTH deactivation curve, involving a short period of full conversion followed by a reduction of the slope and final deactivation, appears when methanol is strongly involved in reactions leading to deactivation by coke and the interconversion reaction among products contribute less to the catalyst deactivation. On the other hand, a progressive reduction of the curve with time on stream (TOS) as the product concentration decreases was indicative of a different mechanism of deactivation, by which coke is formed mainly from reaction products.

Very recent spatio-temporal studies performed by Rojo *et al.* [87] suggested that, for one-dimensional 10-ring topologies (TON and MTT), methanol is strongly involved in reactions leading to coke formation, whereas products alone are not involved in coke forming reactions, validating previous investigations [83]. Other studies also showed that the accumulation of molecular coke occurred mainly within the micropores [25, 83, 87] . Other catalytic properties, such as acid strength and acid site density, may also have a strong influence in the

deactivation mode [83, 91]. These findings were previously proposed by space- and time-resolved operando XRD investigations which are included in **Paper I**, and will be elaborated in Chapter 5.

The diffusion limitations imposed by the one-dimensional 10-ring structures might be partially solved by using one-dimensional zeolites but with larger channel size, such as 12-membered ring structures. MTH research has focussed on H-Mordenite (MOR), a one-dimensional 12-ring channel with side pockets. This zeolite, however, showed also rapid deactivation mainly caused by the involvement of aromatics as coke precursors at 350–400 ^{o}C [87, 92]. However, better catalytic performance in MTH has been shown for MOR catalysts when decreasing the acid site density by Park *et al.* [92].

The major challenge associated with the materials relevant to this work (ZSM-22 and ZSM-23) is to increase the low lifetime in MTH conversion while maintaining the selectivity towards low-aromatic gasoline products. A significant extension of the catalyst lifetime will lead to less frequent regeneration and might allow regular fixed bed operation, thereby significantly lowering process investment and operation costs.

3. Catalyst Improvement by Post-synthetic Approaches

The optimization of the MTH catalytic performance can be reached by changes in the operation conditions or in the catalytic properties. This work is mainly focussed on the improvement by modification of the catalyst properties, particularly by means of post-synthetic treatments.

It is the presence of differently sized micropores that give rise to the use of zeolites as shape selective catalysts. However, the micropore system also limits the applicability of zeolites as MTH catalysts, often imposing diffusion limitations and preventing access to the active sites of the zeolite crystal [93]. Furthermore, ZSM-22 and ZSM-23 zeolites crystalize preferentially as long needles, with the 10-ring channels running in the direction of the needles. Several approaches have pointed to the crystal morphology as a key factor for solving the accessibility problems of the catalyst. In particular, an increased number of pore openings are accessible by using nanosized crystals or by introducing a secondary network of mesopores into the crystal. This can be achieved by a variety of synthetic (bottom-up) and post-synthetic (top-down) approaches. The preparation of such hierarchical zeolites and their improved catalytic performance has been extensively reviewed [13, 94-106].

In these materials molecules diffuse closer to the Knudsen diffusion regime, which is characterized by diffusivities 2-3 orders of magnitude larger than those observed in the more restrictive intra-crystalline regime typical for the purely microporous zeolites [96, 107]. Figure 3.1a, b shows preferential Knudsen pathways in the mesopores (green) than random diffusion paths within the micropores (yellow). Additionally, diffusivity in medium sized zeolites can be specially affected by amorphous species or structural defects in the crystal [11, 108, 109].

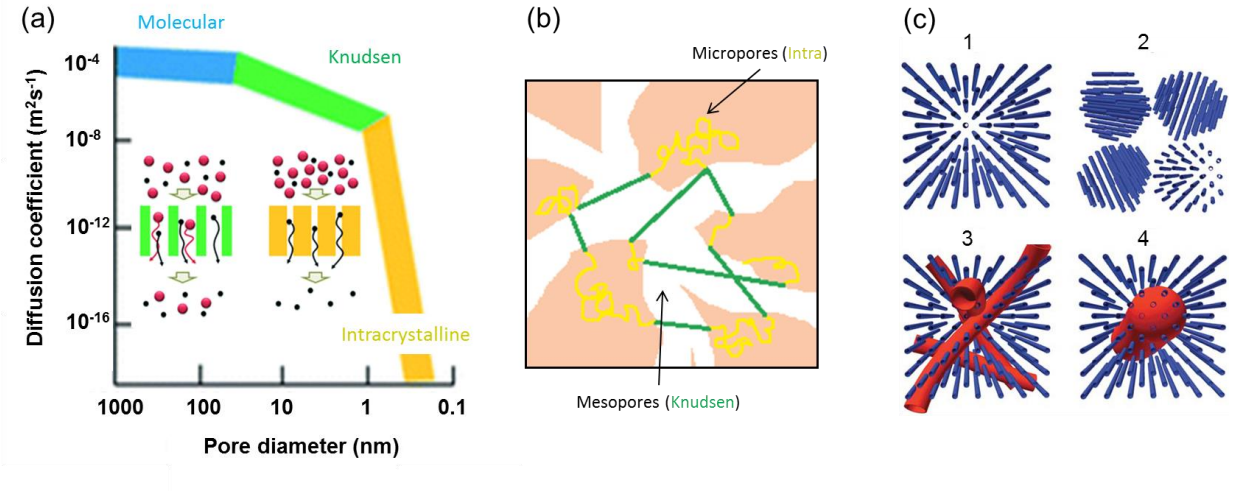

Figure 3.1. (**a**) Magnitudes of diffusion coefficients in different diffusion regimes as a function of pore size and illustration of the diffusion of different sized molecules within mesopores (green) and micropores (yellow). (**b**) Section of a microporous material with embedded interconnected mesopores. Solid lines show molecular trajectories of intra-crystalline diffusion in micropores (yellow) and Knudsen diffusion in mesopores (green). (**c**) Relative position of micro- and mesopores in hierarchical zeolites. Adapted from [96, 107].

Only having different pore diameters (micro/meso) is not the only requisite for the zeolite to be considered hierarchical. The pore systems needs to be efficiently interconnected into well-organized open pathways [102]. If the created mesopores are occluded within the existing micropore system without exiting to the outer parts (case 4 in Figure 3.1c), the catalyst will show diffusion limitations. Hierarchical zeolites must combine the intrinsic catalytic properties of microporous zeolites and the facilitated access and transport in the created mesopore network. The secondary porosity can be either intra- (created within the crystal) or inter-crystalline (agglomerated particles or sheets), as illustrated in cases 2 and 3 of Figure 3.1c, respectively, or even a combination of those.

The effectiveness factor (η), which relates the reaction rate with the intrinsic chemical rate, is generally used in heterogeneous catalysis to illustrate the different degree of catalyst utilization [96, 102]. It is generally presented as a function of the Thiele modulus (ϕ), as in Figure 3.2b. Large Thiele modulus indicates that the diffusion rate is low and diffusion, instead of kinetics, limits the overall reaction. High Thiele modulus and low effectiveness factor results in a poor utilization of the catalyst. In these cases, the concentration throughout the catalyst crystal (c) is much lower than the surface concentration (c_s) and c/c_s approaches zero (Figure 3.2a). Full use of the catalyst particle is associated with a kinetically-controlled regime with no diffusion limitations with Thiele modulus close to zero and effectiveness

factor close to unity. In these cases, the surface concentration approximates the concentration throughout the catalyst and c/c_g approaches one. In order to maximize the effectiveness factor, the diffusion length (L) has to be minimized, and this can be reached with hierarchical zeolites.

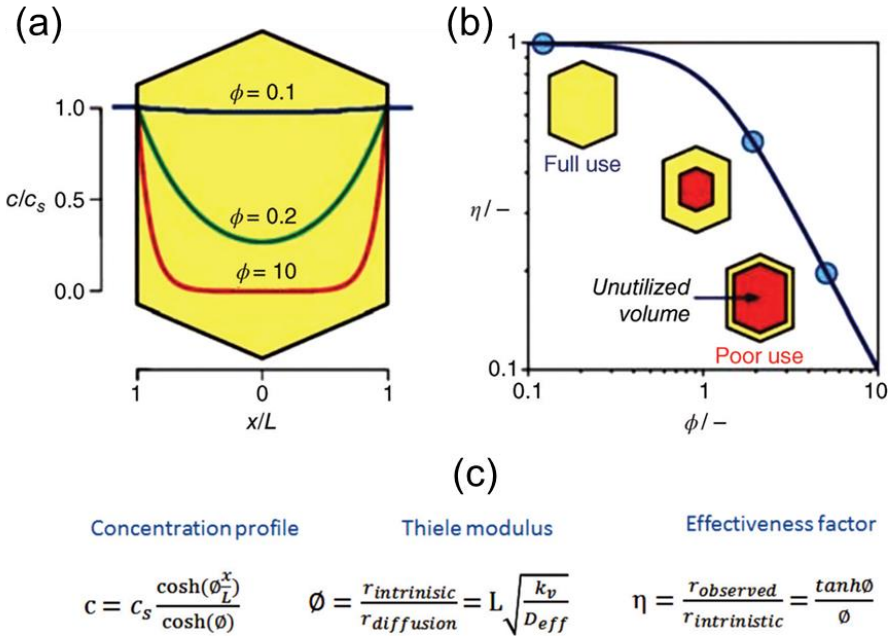

Figure 3.2. (**a**) Concentration profiles in a zeolite crystal with slab geometry at different Thiele modulus. (**b**) Effectiveness factor as a function of Thiele modulus. (**c**) Formulas of concentration profile, Thiele modulus and effectiveness factor. Adapted from [102].

Post-synthetic treatments usually involve destruction of part of the zeolite structure. Depending on the extracted zeolite atoms, these treatments are divided into dealumination and desilication. Dealumination strategies involve leaching of Al from the zeolite framework, usually by steaming at high temperatures. During desilication, Si species are leached out of the zeolite framework and mesopores can be created. Desilication with alkaline solutions, usually NaOH, is the most employed technique to create mesoporosity in zeolites, owing to the efficiency and simplicity of the method. More advanced techniques involve the addition of different molecules to the solution usually referred as pore directing agents (PDA), such as surfactants or alkylammonium hydroxides. This may affect the zeolite catalytic properties in different ways. Further strategies involve a secondary step of acid leaching in order to solve the limitations encountered by the aforementioned methods.

The preparation, characterization and catalytic effects of desilicated ZSM-22 and ZSM-23 zeolites have been extensively investigated in this thesis (**Papers I-III**). Mixtures of NaOH with CTAB (cetyltrimethylammonium bromide) or TBAOH (tetrabutylammonium hydroxide), as well as subsequent acid washing, were employed, thereby encompassing the array of desilication methods reported. Along this chapter, the different desilication methods will be presented, with particular emphasis on one-dimensional zeolites. Table 3.1 (showed at the end of the chapter) presents a summary of all relevant studies dedicated to introduce mesopores in one-dimensional 10-ring and 12-ring zeolites by desilication post-synthetic treatments.

3.1. Desilication by alkaline treatment

Desilication is based on the attack of the hydroxyl ions of the alkaline agent to the framework Si atoms. The preferential removal of Si results in a reduction of the Si/Al ratio and partial dissolution of the zeolite structure, which might be accompanied by mesopore formation. The amount of Si leached out strongly on the number of accessible Si-O linkages. The first challenge is, thus, carry out proper calcination of the microporous zeolite in order to allow larger crystal areas susceptible to mesopore formation [110].

Process conditions such as duration, temperature, base concentration or solid-to-liquid ratio, have a strong influence on the mesopore formation [106]. Generally, more severe conditions generate larger mesopores. However, since different zeolites have different structural properties, desilication parameters need to be adjusted for each particular topology to avoid inefficient dissolution or, on the contrary, excessive loss of material or reduced crystallinity. Zeolite properties, such as chemical composition and structural features, also greatly affect the sensitivity to framework dissolution and mode of mesopore creation by alkaline treatment. General findings applicable to various topologies will be described now.

The mechanism of mesopore formation is markedly dependent on the Al concentration and distribution [111-114]. The negative charge introduced by an Al atom in local framework positions prevents the OH^- attack to surrounding Si atoms and zeolite dissolution is prevented [111]. Therefore, Al-rich zeolites are less susceptible to mesopore generation by desilication than high silica zeolites. High Si/Al ratios, however, result in an excessive dissolution of the framework. In this sense, Groen and co-workers found an optimal Si/Al range of 25 to 50 for

the generation of uniform mesoporosity in MFI framework while maintaining the crystallinity [109, 114], as illustrated in Figure 3.3a. Location of gradients in Al concentration also influences the mechanism of mesopore formation. Mesopores will be preferentially developed from low alumina framework environments, as demonstrated by Al-zoning experiments performed on desilicated ZSM-5 crystals [94, 106, 113, 115]. Additionally, the nature of the Al species may impact desilication by alkaline treatment. Alkaline treated ZSM-5 zeolite with high degree of non-framework Al showed low Si extraction and, consequently, limited mesopore development [116].

Table 3.1 shows that all the desilicated 10-ring zeolites have Si/Al ratios within the optimal range of mesopore generation found for MFI zeolites. On the other hand, some studies reported increased mesopore surface areas even for 12-ring MOR zeolites with relatively low Si/Al after NaOH treatment [117-121]. However, the degree of mesopore surface created was lower than for other 12-ring desilicated structures listed in Table 3.1. Muraza *et al.* [122] showed that the high Si/Al ratio of a ZSM-12 MTW zeolite was neither an impediment to the mesopore development by alkaline treatment, when desilication was carried out under microwave irradiation. Also a first dealumination step previous to desilication has been used for increasing the Si/Al ratio and favour mesopore creation in initially high alumina MOR zeolites [118, 120].

Defects or intergrowths within the zeolite crystal may also strongly influence the mode of mesopore creation. Ogura *et al.* [123] proposed the formation of mesopores by removal of the less resistant amorphous SiO_2 species along boundaries between twining MFI crystals and Svelle *et al.* [124] showed that for MFI zeolite crystals with high number of defects, the Si/Al effect becomes less important and mesopores are formed preferentially from the defects or intergrowths (Figure 3.3b).

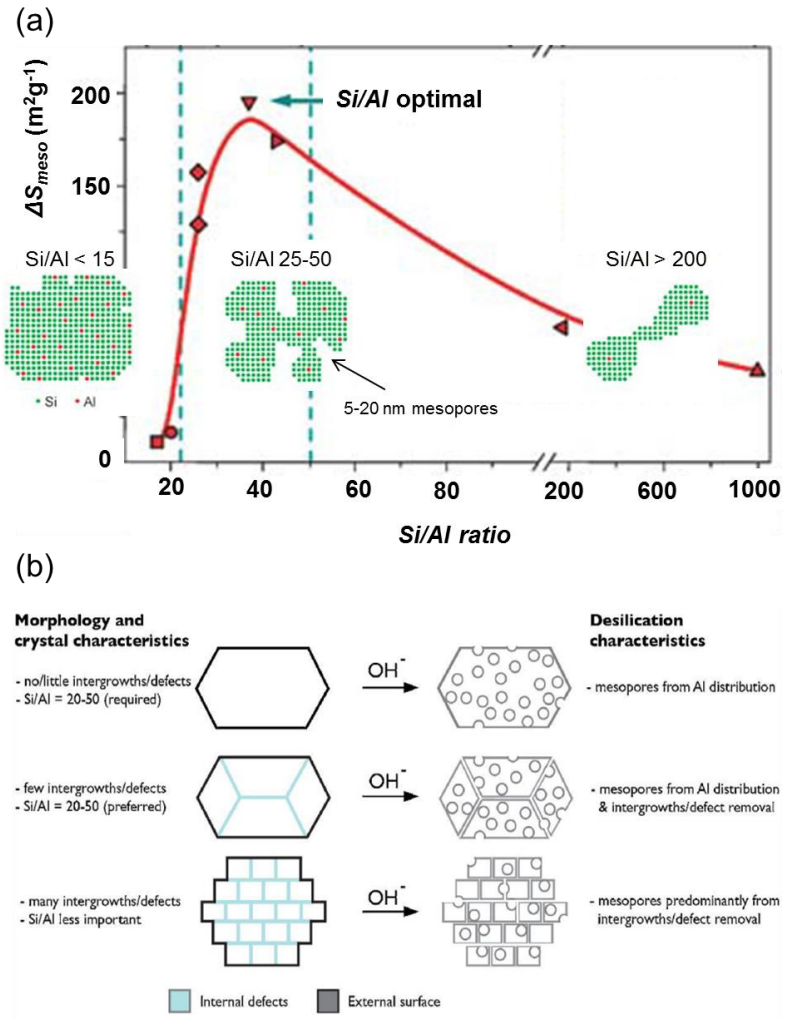

Figure 3.3. (**a**) Effect of the Si/Al on the desilication process and developed mesopores surface area (ΔS_{meso}) and (**b**) relationships between effects of defects/intergrowths and Si/Al ratio on the mesopores formation during desilication of MFI type zeolites. Adapted from [102] and [124].

With respect to the topology, it appears obvious that more open structures with two- or three-dimensional connected channels or large cavities would require less severe conditions to generate effective mesopores within the zeolite crystal than denser one-directional zeolites with similar composition [125, 126]. From Table 3.1, intra-crystalline type mesopores with a narrow size distribution typically of 5-10 nm in size are generally generated within 12-ring zeolite crystals, whereas similar NaOH treatments often results in a higher contribution of inter-crystalline type of mesopores over 10-ring structures. Additionally, pores of different shape and size can be generated depending on the location where the zeolite framework has been dissolved. For instance, if Si areas connecting channels and/or cages are dissolved, new accessible pores will be created in the zeolite structure. This possibility to open new volumes is limited for one-directional channel structures.

The morphology of the zeolite crystal may also impose limitations to develop intra-crystalline mesopores. Verboekend *et al.* investigated the mechanism of mesopore formation by alkaline treatment over different morphologies and concluded that the efficiency of the desilication method and the type of mesopores are strongly influenced by the size of the parent zeolite crystal [127]. If the smallest dimension of the crystal decreases to the typical mesopore size range (5-10 nm), the introduction of intra-crystalline mesoporosity by alkaline treatment was found to dramatically decrease. The short thickness of the needle-shaped crystals characteristic of one-dimensional zeolites favours the formation of inter-crystalline type of mesopores created by roughening of the crystal surface or fragmentation of the crystallites. For 10-ring zeolites, most of the studies reported increased mesopore surface attributed to the presence of both intra- and inter-crystalline mesopore with broad distribution of mesopore sizes (Table 3.1). Inter-mesoporosity generally resulted in lower developed surface area than the one associated with intra-crystalline mesoporosity, generated in larger 12-ring zeolites crystals (plate- and beam-like) under similar conditions. Noteworthy, an exceptional increase in external surface was observed by Liu and co-workers on a ZSM-22 (TON) zeolite modified by alkaline desilication [128]. On the other hand, Ahmed *et al.* reported loss of external surface area on desilicated EU-1 (EUO) zeolite [129], most likely caused by the deposition of EFAl species on the crystal surface. van Laak *et al.* [121] demonstrated inter-crystalline porosity between MOR coffin-shaped crystals with limited dimensions.

Despite desilication by alkaline treatment selectively removes Si from the zeolite framework, it is usually accompanied by framework Al extraction, especially in high alumina zeolites. With increasing desilication conditions, a larger number of amorphous EFAl species can be redeposited in the zeolite crystal. Increased concentration of EFAl species is usually associated with increased Lewis acidity. In addition, desilication treatments may lead to other structural effects, such as T-OH groups or hydroxyl silanol nests as extra-framework Si species (EFSi) [13]. These species might partially block the zeolite pores and modify the acidic properties of the mesoporous material, as previously mentioned in Chapter 1.

The realumination process affects particularly one-dimensional medium pore size structures. Table 3.1 shows that that mesopore generation upon alkaline treatment is generally accompanied by a drastic reduction of the micropore volume, caused by redeposited EFAl species. If these species are formed from framework Al, a reduction of the Brønsted acidity is generally accompanied by generation of Lewis acidity. A sequential acid step washing can restore the microporosity. A different scenario is found for the reported 12-ring zeolites. For

MOR zeolites, mesopores were usually generated without altering the micropore volume or acid site density. On the other hand, some studies reported a reduction of the micropore volume for desilicated MOR, MTW and IFR structures (Table 3.1). Most of these 12-ring treated samples maintained the Brønsted acidity, whereas others showed reduced acidic properties as a consequence of the deposition of amorphous EFAl or EFSi species. EFAl can be generated without drastically reducing the density of Brønsted acid sites [121, 130-132].

3.2. Additional pore directing agents

Desilication with NaOH is known to occasionally result in the destruction of the zeolite framework. The treatment is also not very specific with respect to the size of the mesopores developed. Instead, treatments combining NaOH with other agents such as surfactants or hydroxides or various organic (tetralkylammonium) cations, tend to result in controlled mesopore size. These methods are particularly appealing for high silica zeolites, for which the desilication via alkaline treatment alone results in excessive zeolite dissolution [133].

3.2.1. Alkaline-surfactant combined methods

The addition of micelle-forming surfactants to the alkaline solution protects the zeolite structure against the attack of the OH^- groups and provides better control of the mesopore development, irrespective of the Si/Al ratio. This strategy usually employs CTAB as surfactant under mild conditions and longer dissolution times than alkaline desilication. Such treatments often results in lower loss of material compared to alkaline desilication.

The NaOH attack to the Si-O bonds during desilication results in the dissolution of zeolite fragments. Surfactant molecules, with the positive-charged surfactant polar end pointing to the aqueous solution, may connect to the dissolved zeolite fragments and slowly induce reassembly or re-deposition of them to the zeolite structure, as schematically represented in Figure 3.4c. The process is therefore known as surfactant-assisted recrystallization. It has been mostly applied to FAU, MFI and MOR zeolites [98, 100, 134]. Ivanova *et al.* [134] clarified the mechanism of zeolite recrystallization by an extensively analysis of the

intermediate products recovered during each recrystallization step over as-synthesized and protonated MOR. The proposed mechanism involved a first rapid proton ion-exchange with Na^+ cations and formation of small mesopores within the crystals, followed by diffusion of CTAB molecules in the intra- and inter-crystalline spaces of the zeolite and ion-exchange of Na with CTA^+ cations. Finally, micelle formation and condensation of siliceous fragments around micelles both in the intra and inter-crystalline mesopores occurs. Surfactant species embedded in the zeolite crystal are eventually removed by calcination and pores of dimensions determined by the micelle size are created. Accordingly, by varying the chain length of the surfactant, the size of the created mesopores can be tuned to a range of pore size distributions [135, 136]. For instance, the addition of CTAB surfactant with C_{16} chain length in the desilication medium typically give 3-10 nm mesopores within the zeolite crystals.

A two-step recrystallization process, where the zeolite is partially dissolved in NaOH solution and then treated with CTAB, also leads to mesopores with controlled size. Ivanova and co-workers reported the formation of new mesoporous phases over MOR zeolites using this method [137]. Variation of the NaOH concentration resulted in different degrees of dissolution, which in turn lead to different types of MOR recrystallized materials, as represented in Figure 3.4a, b [138, 139]. By using mild NaOH solutions, composite materials consisting of two phases, a micro/mesoporous MOR-type zeolite and a mesoporous MCM-41 phase deposited on the crystal surface can be synthesized (Figure 3.4b). Excessive NaOH concentration resulted in too much crystal dissolution leading to a complete transformation to MCM-41 mesoporous material with absence of microporosity (Figure 3.4a). Table 3.1 shows that narrow 3-4 nm mesopores could be formed in MOR and MTW zeolites [131, 139] by this process. A similar recrystallization process was carried out over 10-ring ZSM-22 zeolite by Liu *et al.* [128]. Interestingly, the limitation imposed by the ZSM-22 crystal size on the generation of intra-crystalline type mesopores could be overcome, since well-defined 3-4 nm sized mesopores were achieved. Furthermore, the surfactant treatment removed extra-framework amorphous species generated by the NaOH treatment, resulting in enhanced accessibility to the reactive sites.

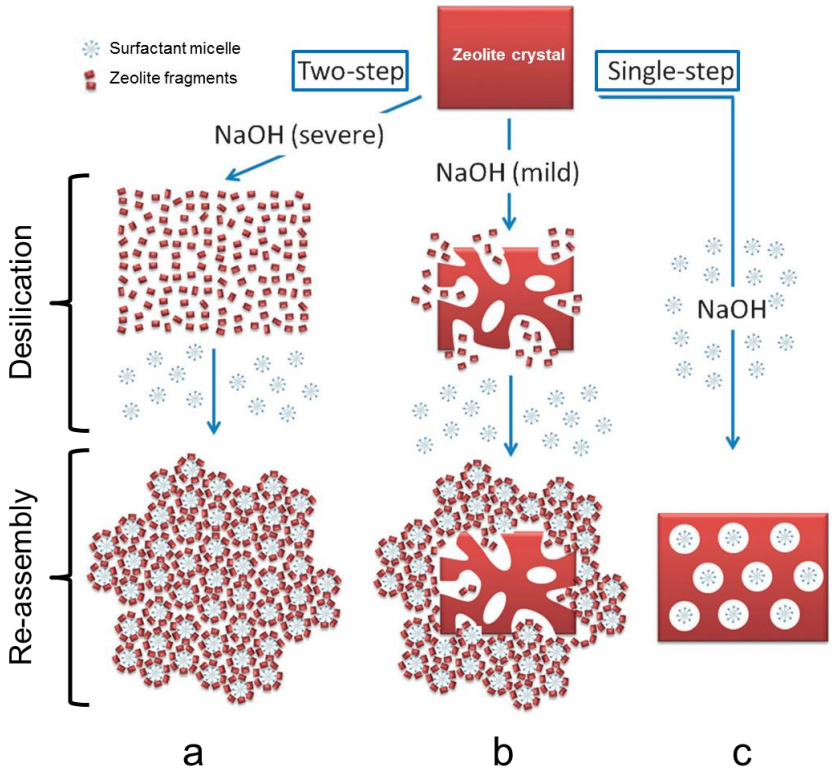

Figure 3.4. Schematic representation of the different materials prepared by two-step (**a**, **b**) and single-step (**c**) surfactant-assisted approaches. Adapted from [98].

3.2.2. Alkaline-tetralkylammonium hydroxides combined methods

Tetraalkylammonium cations, such as tetrapropyl (TPA^+) or tetrabutyl (TBA^+) cations, may also participate in the desilication process when organic TPAOH or TBAOH bases are mixed with inorganic NaOH in aqueous solutions. These cations have been reported to largely protect the zeolite crystal upon desilication, resulting in mesopores of small diameter and narrow pore size distribution. In comparison with inorganic hydroxides, they are intrinsically less reactive to break Si-O bonds and interact preferentially with the zeolite surface hindering the OH^- attack [94, 116]. Most of the research in this field has been dedicated to ZSM-5 and Beta zeolites [110, 140-146].

Effective mesopore creation has been reported even over highly siliceous MFI zeolites, which expanded the composition range of zeolites susceptible to mesopore development and highlights that mesopore generation is not fully dependent on the zeolite framework composition when the PDA is introduced [133, 143]. Interestingly, the use of organic

hydroxides during desilication may lead to mesoporous materials already in the protonic form after calcination, which avoids the need for the general ion-exchange process [94].

To the best of our knowledge, this strategy has not yet been applied to one-dimensional zeolites and will be investigated in this thesis (**Paper II**).

3.3. Effect of acid treatments

A mild acid treatment is usually combined with desilication strategies in order to alleviate accessibility problems created by amorphous species extracted during desilication. This strategy is mostly carried out for medium size one-dimensional zeolites (TON, MTT, EUO), as can be seen in Table 3.1, and results in hierarchical structures with preserved crystallinity and increased microporosity and surface area. The removal of the EFAl species caused increased Si/Al ratios closer to the ones of the starting zeolite. The Brønsted acidity can be partially restored or even increased. Verboekend *et al.* [127] reported a decrease in Si/Al ratio and, surprisingly, a reduced density of BAS with respect to the parent zeolite, accompanied by a partial removal of EFAl species. Very recently, Dyballa *et al.* performed desilication of ZSM-22 using both NaOH and KOH and sequential acid leaching and found significant reduction of the density of acid sites [147]. For the more spacious 12-ring materials, the micropore volume was not drastically affected upon desilication, meaning that the acid washing step is generally not needed. Only one study by Chaouati and co-workers reported acid washing of desilicated MOR zeolite with slightly reduced microporosity [117].

Acid treatments were also carried out to bring the Si/Al of high alumina MOR zeolites to adequate values for efficient mesopore development [118, 120]. The resulting zeolites showed an increased number of BAS and stronger acidity. A further acid leaching of the acid-alkaline treated zeolites did not result in any significant change in textural properties.

3.4. Influence on the catalytic properties

Hierarchical zeolites prepared by post-synthetic strategies have been demonstrated to give superior performance than conventional microporous zeolites in industrially important catalytic processes [96, 97, 101]. Intuitively, the introduction of mesoporosity lead to superior catalytic performance for zeolites which are more predisposed to suffer from diffusion limitations, such as one-dimensional zeolites with medium sized pores. Table 3.1 illustrates the benefits of one-dimensional hierarchical zeolites in several catalytic processes, including olefin oligomerization, isomerization and of alkanes, alkenes and xylenes, cracking of high alkanes, benzene and naphthalene alkylation, cumene disproportionation, LDPE pyrolysis and MTH reaction.

Form the reported investigations, it appears clear that acidity and porosity cannot be discussed independently since acidity is useless if not accessible and porosity similarly will not be fully effective without providing access to the acitve centres. For instance, Verboekend *et al.* [148, 149] demonstrated the need for an acid leaching step to open the access to the active sites and increase the performance of alkane isomerization catalysed reactions. Matias *et al.* [150] showed an increase in the initial butene isomerization catalyst activity oh H-NU-10, but the additional mesoporosity did not enhance the stability of the TON catalyst. Martinez *et al.* [151] highlighted the need for tuning the micro-mesoporous structure in order to achieve maximum diesel selectivity over Theta-1 catalyst. Concerning oxygenate to hydrocarbon reactions, Ahmed and co-workers reported increased conversions for DME to olefins and higher propylene selectivities for hierarchical H-EU1 [152].

With regard to the MTH reaction, most of the research has been dedicated to achieve mesoporous H-ZSM-5 catalysts by alkaline treatment [153-157], surfactant-assisted solutions [135, 158] and TBAOH combined method [159]. The general outcome of the effect of mesoporosity on MTH catalysts is an increased lifetime attributed to a more efficient use of the catalyst crystal which results in an increased resistance towards coking or coke species mainly formed on the external surface of the catalyst. Any modification of the pore size may modify the shape selective properties of the catalyst. Accordingly, it has been reported a significant improvement in propene and C_{5+} hydrocarbons selectivity for mesoporous H-ZSM-5-based MTO [157] or MTG [153] and also a shift in aromatics distribution towards heavier aromatic hydrocarbons [153, 154]. The Lewis acidity was suggested to have an

influence on the enhanced activity. With respect to one-dimensional zeolites, only a recent contribution by Dyballa *et al.* [147] found a two-fold increase in lifetime, accompanied by enhanced propene selectivities, in MTO conversion over mesoporous H-ZSM-22 catalysts with optimal BAS density. Furthermore, similar product spectrum was obtained for the purely microporous and the mesoporous catalyst, suggesting that the 10-ring pore system of H-ZSM-22 rules the shape-selective properties in MTO.

Table 3.1

Summary of the strategies carried out to create mesoporous one-dimensional zeolites including properties of the parent material, porosity and acidity modifications and the effect on test reactions employed over the hierarchical zeolites.

Zeolite structure [Ref.]	Strategy	Microporous zeolite		Hierarchical zeolite			
		Si/Al	Smallest dim/ morphology	Mesopores	Microporosity	Acidity, others	Reaction
10-ring TON							
Theta-1 [151]	Desilication NaOH 0.2M 0.5h 85C	50	0.04 µm Nanorods	Inter	Reduced	BA partly reduced	Increased initial activity in propene oligomerization Higher stability
	Desilication + acid $H_2C_2O_4$ 0.8M 2h 70C				Restored	BA restored	Improved selectivity to diesel
ZSM-22 [127]	Desilication NaOH 0.6M 2h 85C	42	0.04 µm Nanorods	Inter/intra Broad distribution	Reduced	BA reduced LA increased-EFAl	-
ZSM-22 [149]	Desilication + acid HCl 0.1M 6h 65C				Partly restored	BA partly restored LA partly reduced Removal of EFAl	Higher n-alkane isomerization activity and monobranched selectivity
ZSM-22 [148]	Desilication + acid NaOH + HCl	38	Nanorods	Inter/intra Broad distribution	Partly reduced	BA reduced EFAl	Superior alkane isomerization performance/less cracking
ZSM-22 [147]	Desilication + acid NaOH 0.4M 1h 85C + HCl 0.1M 6h 65C	30	< 1 µm Needle-like	Not indicated	Reduced	Optimal ASD Similar acid strength Defects	Increased MTO lifetime Increased propene selectivity
ZSM-22 [128]	Desilication NaOH 0.3M 0.5h 80C	32	0.03-0.05 µm Needle-like	Inter	Reduced	ASD reduced Acid strength reduced Defects	Increased n-alkane isomerization selectivity for composite materials
	Recrystallization NaOH 0.15-0.9M + CTAB 24h 100-120C			Intra (3-4 nm) to MCM-41	Reduced to absent	BA reduced LA increased Removal of EFAl	Best isomerization selectivity/low cracking activity for composite materials

Table 3.1 (*continued*)

Zeolite structure [Ref.]	Strategy	Microporous zeolite		Hierarchical zeolite			
		Si/Al	Smallest dim/ morphology	Mesopores	Microporosity	Acidity, others	Reaction
NU-10 [150]	Desilication NaOH 0.4M 0.5h 80C	31	0.05 µm Nanorods	Inter/intra (20 nm)	Partly reduced	BA reduced LA increased EFAl Removal of defects	Higher activity in 1-butene isomerization
NU-10 [160]	Desilication NaOH 0.6M 0.5h 80C	33	0.08 µm Needle-like	Inter/intra (20-30 nm)	Unaltered	LA increased EFAl, EFSi Adsorption enhanced	Increased activity in o-xylene isomerization
10-ring MTT							
ZSM-23 [161]	Desilication + acid NaOH 0.2M 5m 85C + HNO_3 0.3M 10m 80C	76	0.07 µm Nanorods	Inter/intra (2-5 nm)	Drastically increased	BA partly increased Similar acid strength Removal of defects	Enhanced stability in n-hexane cracking Higher propylene selectivity
10-ring EUO							
EU-1 [129]	Desilication NaOH 0.25M 1h 80C	25	Nanorods	Inter/intra (10-20 nm)	Reduced	Total acidity unaltered EFAl Defects	Decreased conversion in DME to olefins Higher propylene selectivity
EU-1 [152]	Desilication + acid NaOH 0.5M 1h 80C + HNO_3 4M 0.5 h 70C	25	< 0.5 µm Agglomerates	Intra (10 nm)	Restored	Total acidity increased Removal of EFAl Defects	Increased conversion in DME to olefins Higher propylene selectivity

Table 3.1 (*continued*)

Zeolite structure [Ref.]	Strategy	Microporous zeolite		Hierarchical zeolite			
		Si/Al	Smallest dim/ morphology	Mesopores	Microporosity	Acidity, others	Reaction
12-ring MOR							
Mordenite [125]	Desilication NaOH 0.2M 1h 85C	45	Not indicated	Intra	Unaltered	Total acidity unaltered Acid strength unaltered	-
Mordenite [109]	Desilication NaOH 0.2M 0.5h 65C	30	2 µm Plate-like	Intra (10 nm)	Unaltered	BA unaltered	Superior stability in benzene alkylation/Higher ethene selectivity
Mordenite [162]	Desilication NaOH 0.2M 0.5h 60C	18-40	Agglomerates	Not indicated	Partly reduced	BA reduced LA increased EFAl	Improved conversion in benzene alkylation with 1-dodecene Inhibition of 1-dodecene isomerization to linear alkylbenzenes
Mordenite [121]	Desilication NaOH 1M 15m 70C	5.5-10	0.04 µm Coffin-shaped	Inter (35 nm)/ Intra (3-8 nm)	Partly reduced	BA partly increased Amorphous species	Higher activity in benzene alkylation with propene Similar selectivity to cumene
Mordenite [119]	Desilication NaOH 0.2M 2h 85C	9.5	Aggregates	Inter/intra (10 nm)	Unaltered	Total acidity unaltered Acid strength unaltered EFAl	-
Mordenite [117]	Desilication NaOH 0.4M 2h 85C	10	0.1 µm	Intra (3-7 nm)	Partly reduced	BA reduced Acid strength increased LA increased EFAl	Increased activity in m-xylene transformation
	Desilication + acid HCl 0.5M 10m 30C				Unaltered	Removal of EFAl BA restored	No remarkable changes

Table 3.1 (*continued*)

Zeolite structure [Ref.]	Strategy	Microporous zeolite		Hierarchical zeolite			
		Si/Al	Smallest dim/ morphology	Mesopores	Microporosity	Acidity, others	Reaction
Mordenite [118]	Desilication NaOH 0.2M 0.5 h 65C	15	Plate-like	Limited	Unaltered	-	Low conversion in benzene alkylation
	Acid HNO_3 2M 4h 100C			Limited	Increased	BA reduced	Higher conversion in 2-methyl-2-pentene isomerization Higher benzene alkylation conversion
	Acid + desilication	25[1]		Intra	Reduced	BA increased Acid strength increased Removal of EFAl Diffusivity enhanced	Improved performance in 2-methyl-2-pentene isomerization Higher activity in benzene alkylation
Mordenite [120]	Acid HNO_3 3M 1h	8	0.15 µm Agglomerates	Limited	Unaltered	BAS reduced EFAl reduced	No significant improvement in benzene alkylation with propene
	Desilication NaOH 0.05-1M 70C			Inter/intra	Unaltered	LAS reduced	Higher activity and selectivity to cumene
	Acid + desilication	30[1]		Intra (3-8, 40 nm)	Unaltered	Acid strength increased EFAl	Increased activity Increased selectivity to cumene
	Acid + desilication + acid 0.1 M 15m 50C						No remarkable change
Mordenite [138]	Recrystallization NaOH 0.4-1.2M rT + CTAB 100C	48	> 0.1 µm Plate-like	Intra/inter to MCM-41	Unaltered to absent	Unaltered to decreased ASD and acid strength LAS increased Accessibility increased	Higher activity, stability and selectivity in naphthalene alkylation with cyclohexene for composite materials

Table 3.1 (*continued*)

Zeolite structure [Ref.]	Strategy	Microporous zeolite		Hierarchical zeolite			
		Si/Al	Smallest dim/ morphology	Mesopores	Microporosity	Acidity, others	Reaction
Mordenite [139]	Desilication NaOH 0.5M rT	48	0.1 µm	Intra (5-50 nm)	Partly decreased	Accessibility increased	Higher activity in cumene disproportionation
	Recrystallization NaOH 0.5-1.6M + CTAB 100C			Intra (3-4nm)/inter to MCM-41	Unaltered to absent	Unaltered to decreased ASD and acid strength Accessibility increased	Best activity and stability in cumene disproportionation for composite materials – coating prevents coking
12-ring MTW							
ZSM-12 [130]	Desilication NaOH 0.5M 1h 85C	45	Not indicated	Limited	Reduced	BA unaltered Acid strength increased LA increased	Increased activity in α-pinene isomerization
ZSM-12 [122]	Desilication NaOH 0.2M 10m 85C	80	0.1 µm Agglomerates	Intra (5-15 nm)	Drastically reduced	Total acidity reduced Acid strength reduced EFAl/EFSi	Higher selectivity to olefins n-heptane cracking
ZSM-12 [131]	Desilication NaOH 0.5M 1h 90C	40	< 1 µm Plate-like	Intra	Drastically reduced	EFSi Removal of defects	Higher activity selectivity in α-pinene isomerization
	Recrystallization NaOH/CTAB24h 100C						Lower activity
12-ring IFR							
ITQ-4 [132]	Desilication NaOH 0.2M 0.5h 65C	32	0.2 µm Beam-like	Intra (3-10 nm)	Drastically reduced	BA unaltered BA more accessible LA increased	-
ITQ-4 [163]	Desilication NaOH 0.2M 0.5h 65C	32	0.2 µm Beam-like	Intra (3-10 nm)	Reduced	BA unaltered Removal of defects Diffusion and adsorption enhanced	Improved activity and performance in LDPE pyrolysis

[1] Si/Al ratio of the sample before desilication (after first dealumination).

4. Experimental

A general description of the experimental procedures for the preparation of the materials used in this thesis (Section 4.1 and 4.2) as well as the characterization (Section 4.3 and 4.4) and catalytic testing (Section 4.5) methods are provided in this chapter. Particular emphasis is given to the characterization by physisorption measurements which are core for the present work.

4.1. Catalyst synthesis and preparation

Commercially available ZSM-22 (Si/Al = 50) and ZSM-23 (Si/Al = 23) zeolites supplied by Zeolyst International were employed in this thesis.

In house synthesized ZSM-22 zeolite was also investigated in this work. The synthesis was carried out under hydrothermal conditions. Before the synthesis, Teflon liners were cleaned in a 15 % HF solution and extensively rinsed with deionized water. ZSM-22 (Si/Al = 45) was synthesized following the procedure described elsewhere [36] and summarized:

- 1.05 g of aluminium sulphate (J. T. Baker) was added to 10.9 g of distilled water under vigorous stirring. An aqueous solution of 2.4 g of potassium hydroxide (Sigma-Aldrich) dissolved in 10.89 g distilled water was prepared and mixed with the previous solution. Another solution of 6.26 g of diaminooctane (DAO from Fluka) dissolved in 43.6 g of distilled water was added to the first mixture.
- To the resulting solution, 28.5 g of Ludox AS-30 colloidal silica (Sigma Aldrich) diluted with 16.16 g of distilled water was added under vigorous stirring. This final mixture was stirred for 30 min and aged for 24 h at room temperature.
- The gel with composition [8.9 K_2O : 1.0 Al_2O_3 : 90 SiO_2 : 3 K_2SO_4 : 27.3 DAO : 3588 H_2O] was transferred into 40 ml Teflon-lined stainless steel autoclaves. Crystallization was carried out at 160 °C for 72 h in a tumbling oven (37 rpm). Teflon coated magnets were placed inside the autoclaves to enhance the gel mixing.

- The product was recovered by filtration, extensively washed with deionized water and dried overnight at 90 °C.

4.1.1. Calcination and ion-exchange

The needle shaped ZSM-22 crystals containing narrow pores require a special calcination to remove the organic template. The as-synthesized zeolite was calcined under a flow of pure oxygen at 550 °C for 12 h. The temperature of the oven was increased stepwise, in 100 °C segments up to 400 °C and 50 °C segments above 400 °C, with a hold time of 30 min between each temperature increase. The received commercial ZSM-22 and ZSM-23 samples were calcined following the same procedure to ensure a proper template removal.

The acidic form of the calcined zeolites was produced by three consecutive ion exchanges with a 1 M NH_4NO_3 solution using 100 ml per gram of material in a plastic flask at 75 ºC for 2 h and calcined in static air at 550 ºC for 2 h, to remove ammonia.

4.2. Post-synthetic strategies

A series of desilicated ZSM-22 zeolites were prepared from the two (commercial and in house synthesized) calcined microporous samples by three sequential post-synthetic treatments, *i.e.* using NaOH, mixtures of CTAB/NaOH and mixtures of TBAOH/NaOH, followed by acid leaching. The conditions were selected according to literature [127, 150, 160]. Sample codes and treatments conditions are presented in the flow diagram in Figure 4.1.

4.2.1. Alkaline desilication

The calcined zeolites were treated with 0.2 M or 0.5 M NaOH aqueous solutions at 80 °C for 2 h, with a solid to liquid ratio of 33 g of zeolite per litter of NaOH solution (*-at* coded series). The final suspensions were quenched in ice bath, centrifuged and washed with deionized water until pH was close to neutral (measured with pH indicator). The samples were dried

overnight at 60 °C. A fraction of each desilicated sample was brought to the protonic form as described in Section 4.1.

4.2.2. Alkaline-surfactant desilication

Desilication of the calcined samples was carried out in a mixture of 0.05 M CTAB and 0.25 M or 0.5 M NaOH at 80 °C for 24 h. 50 g of zeolite was used per litter of CTAB/NaOH solution (-*ats* coded series). The final suspensions were quenched in an ice bath, centrifuged and washed with deionized water until pH was close to neutral. The samples were dried overnight at 60 °C. To remove all surfactant, the CTAB/NaOH samples were calcined at 550 °C for 15 h under a flow of pure O_2, using a heating rate of 1.8 °C/min to reach 550 °C in a flow of 50 : 50 N_2 and O_2. A fraction of each sample was brought to the protonic form as described in Section 4.1.

4.2.3. Alkaline-tetrabutylammonium desilication

The calcined samples were treated with a mixture of 0.08 M TBAOH and 0.12 M NaOH at 65 °C or 80 °C during 0.5 h. 30 g of zeolite was used per litter of TBAOH/NaOH solution (-*tba* coded series). The final suspensions were quenched in ice bath, centrifuged and washed with deionized water until the pH was close to neutral. The TBAOH/NaOH samples were calcined in the same way as for the CTAB/NaOH samples. A fraction of each sample was brought to the protonic form as described in Section 4.1.

4.2.4. Acid treatment

A fraction of each desilicated sample was submitted to acid washing in 0.1 M aqueous HCl solution at 65 °C for 6 h, using 10 g of zeolite per litter of solution. The resulting suspensions were quenched in ice bath, centrifuged and washed with deionized water until pH was close to neutral. The samples were dried overnight at 70 °C. For comparative purposes, the parent zeolite was also treated in HCl using the same conditions. The acid washed samples were brought to the protonic form as described in Section 4.1.

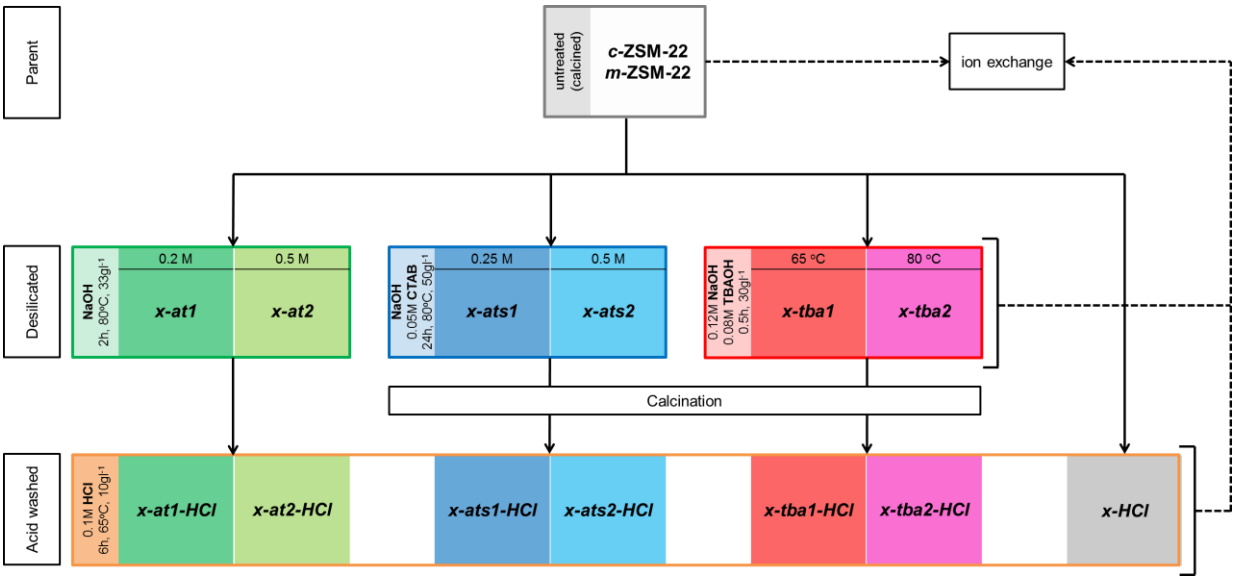

Figure 4.1. Flow diagram of the experimental steps carried out during the preparation of the ZSM-22 samples. First row corresponds to untreated zeolites, second row to desilicated zeolites and third row to acid-washed zeolites. Colour codes (green=*at* series, blue=*ats* series and red=*tba* series) are kept along this thesis. "*x*-" = commercial (*c*-ZSM-22-) or in house synthesized (*m*-ZSM-22-) ZSM-22.

The calcined commercial ZSM-23 zeolite was also submitted to post-synthetic treatments only using NaOH and mixtures of CTAB/NaOH, followed by acid leaching. Same procedure as described above was carried for each treatment. Sample codes and treatments conditions are presented in the flow diagram in Figure 4.2.

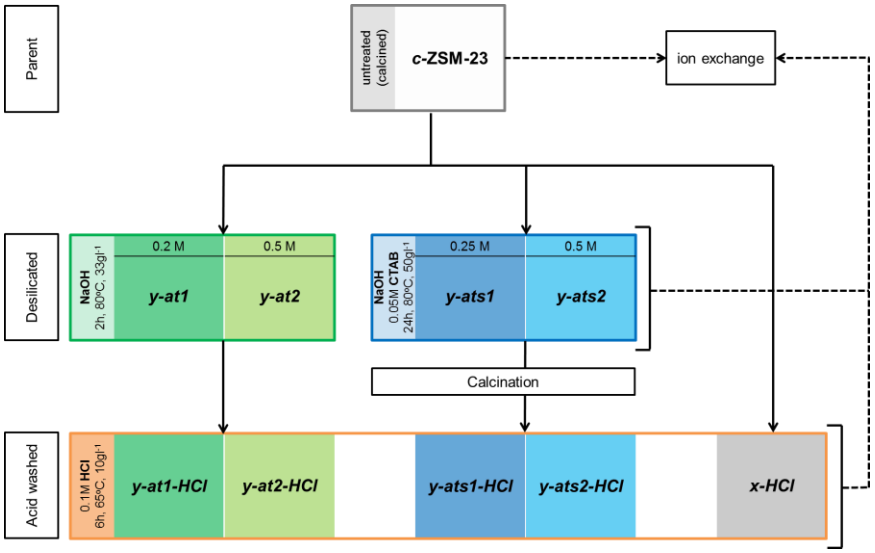

Figure 4.2. Flow diagram of the experimental steps carried out during the preparation of the ZSM-23 samples. First row corresponds to untreated zeolites, second row to desilicated zeolites and third row to acid-washed zeolites. Colour codes (green=*at* series, blue=*ats* series) are kept along this thesis. "*y*-" = commercial c-ZSM-23.

4.3. Ex-situ characterization

The microporous and post-synthetic treated zeolites were characterized by using a variety of methods prior to being tested in the MTH conversion. The characterization methods are outlined in this section.

4.3.1. Powder X-Ray Diffraction (PXRD)

PXRD was used to firstly analyse the phase purity of the in house synthesized ZSM-22 zeolite as well as to check the crystallinity of the commercial ZSM-22 and ZSM-23 samples. Figure 4.3 compares the diffraction pattern of the investigated zeolites with the theoretical TON and MTT pattern in the powder diffraction file (PDF) database revised by Joint Committee on Powder Diffraction Standards. Commercial and in house synthesized ZSM-22 samples consist of a highly crystalline TON structure. The peak observed around 21.5 degrees is ascribed to a cristobalite impurity which commonly co-exists with ZSM-22 [28, 36]. Commercial ZSM-23 shows a pure MTT structure. PXRD was also used to check the crystallinity of the samples after the post-synthetic treatments.

The PXRD measurements were performed using a Siemens Bruker D5000 instrument with Bragg-Brentano geometry and Cu K_α radiation (λ = 1.5406 Å). A small fraction of zeolite powder was grinded in a mortar and mixed with ethanol before dispersing it on a glass plate sample holder and allowing ethanol to evaporate.

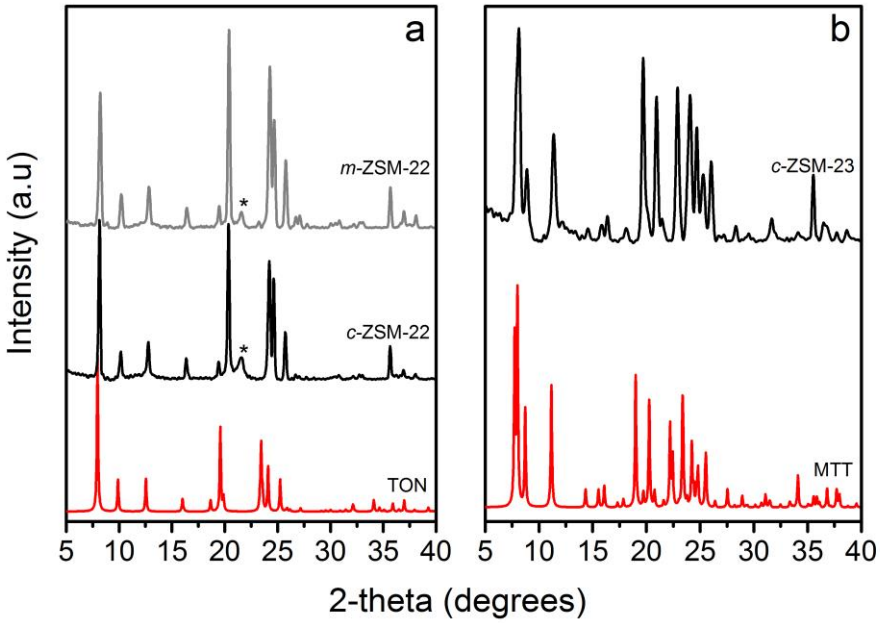

Figure 4.3. PXRD patterns of the (**a**) theoretical TON structure and commercial and in house synthesized ZSM-22 zeolites and (**b**) theoretical MTT structure and commercial ZSM-22 zeolite. Asterisk (*) indicates the position of cristobalite impurity.

4.3.2. Elemental Analysis

Once the correct phase was verified, elemental analysis was employed to quantify the Si and Al content in the zeolite and determine the Si/Al ratio. The measurements were performed on an Agilent Technologies 4100 Microwave Plasma-Atomic Emission Spectrometry (MP-AES) instrument.

Approximately 50 mg of zeolite was introduced in a Teflon vial. 1 ml of 15 wt% HF (Fluka, 40 %) was added to the vial. The vial was closed, shaken and left for 30 min. In order to neutralise the excess of HF, 0.15 g of H_3BO_3 was dissolved in 12.5 ml of H_2O in a 50 ml polypropylene volumetric flask and the dissolved zeolite was transferred into this volumetric flask and diluted to 50 ml.

4.3.3. Scanning Electron Microscopy (SEM)

SEM was used to investigate the crystal size and morphology of the zeolites as well as to assess the formation of mesopores by examining the roughening of the surface of the zeolite.

SEM micrographs were recorded on a SU8230 FE-SEM instrument working at 5–10 kV, using beam deceleration mode. The samples were prepared by dispersing a small amount of powder on a carbon tape on SEM stubs.

4.3.4. Transmission Electron Microscopy (TEM)

TEM was employed to determine the morphology and aspect ratio of isolated (when possible) zeolite crystallites as well as to investigate the intra-crystalline mesopore formation of the micro/mesoporous zeolites.

TEM images were recorded using a CM300 FEG-TEM operating at 300 kV (at Haldor Topsøe AS) and a Philips CM-10 microscope operating at 100 kV (at ITQ-UPV institute). A small amount of sample was crushed in a mortar and dispersed in ethanol, which was ultrasonicated for 20 sec to further break up the agglomerates. A few drops of this solution were placed on a TEM Cu-grid coated with lacey carbon placed on a piece of filter paper. The ethanol was allowed to evaporate for 10 min before the TEM grid was stored in ambient conditions.

4.3.5. Physisorption Measurements

N_2 physisorption measurements were used to determine the surface area and pore volume of the zeolites under study. The measurements were carried out on a Belsorp-mini II instrument. The BET method was used to determine the specific (BET) surface area, the *t-plot* method was applied to determine the micropore volume and the external surface area and the BJH method was used to evaluate the mesopore size distribution.

About 60 mg of zeolite was weighted and measured in a range of relative pressures of $\boldsymbol{p/p_0}$ = 0–0.99 at 77 K. Before each measurement, the samples were outgassed under vacuum at 80 ºC for 1 h and 4 h at 300 ºC. The porous properties of the deactivated samples were also

investigated (**Paper I)**. Coked catalysts were pre-treated under vacuum for 1 h at 80 ºC and 4 h at 150 ºC.

Isotherm type and total pore volume

The isotherms are presented as $\boldsymbol{V_a}$ (cm^3(STP) g^{-1}), *i.e.* the volume of standard state nitrogen (273.15 K, 101.3 kPa) adsorbed per gram of sample, plotted against $\boldsymbol{p/p_0}$, a dimensionless quantity which describes the pressure in the sample cell relative to the saturation pressure. The parent microporous zeolites gave type I adsorption isotherms (Figure 4.4a), whereas the micro/mesoporous samples showed a combination of type II-IV isotherms, according with the IUPAC classification [164, 165]. Type II-IV isotherms typically present a hysteresis loop (Figure 4.4d) associate with capillary condensation occurring in the mesopore, which provides information about the pore shape and structure [166, 167]. However, the analysis should be made carefully, since most mesopore systems had a broad variation of shapes and sizes. Samples with inter-crystalline mesopores generally showed an increase in the N_2 uptake at high partial pressures (Figure 4.4g) ascribed to the space between aggregated nanocrystals of the zeolite.

The total pore volume $\boldsymbol{V_{pore}}$ (cm^3/g) is determined from the adsorbed volume ($\boldsymbol{V_a}$) at partial pressures at $\boldsymbol{p/p_0} \sim 0.99$ from the following equation:

$$\boldsymbol{V_{pore}} = \frac{\boldsymbol{PV_aV_M}}{\boldsymbol{RT}} \qquad (\mathbf{1})$$

where

- $\boldsymbol{P}$ and $\boldsymbol{T}$ are ambient pressure and temperature, respectively
- $\boldsymbol{R}$ is the universal gas constant
- $\boldsymbol{V_M}$ is the molar volume of the liquid adsorbate. $\boldsymbol{V_M}$ (N_2) = 34.7 cm^3/mol

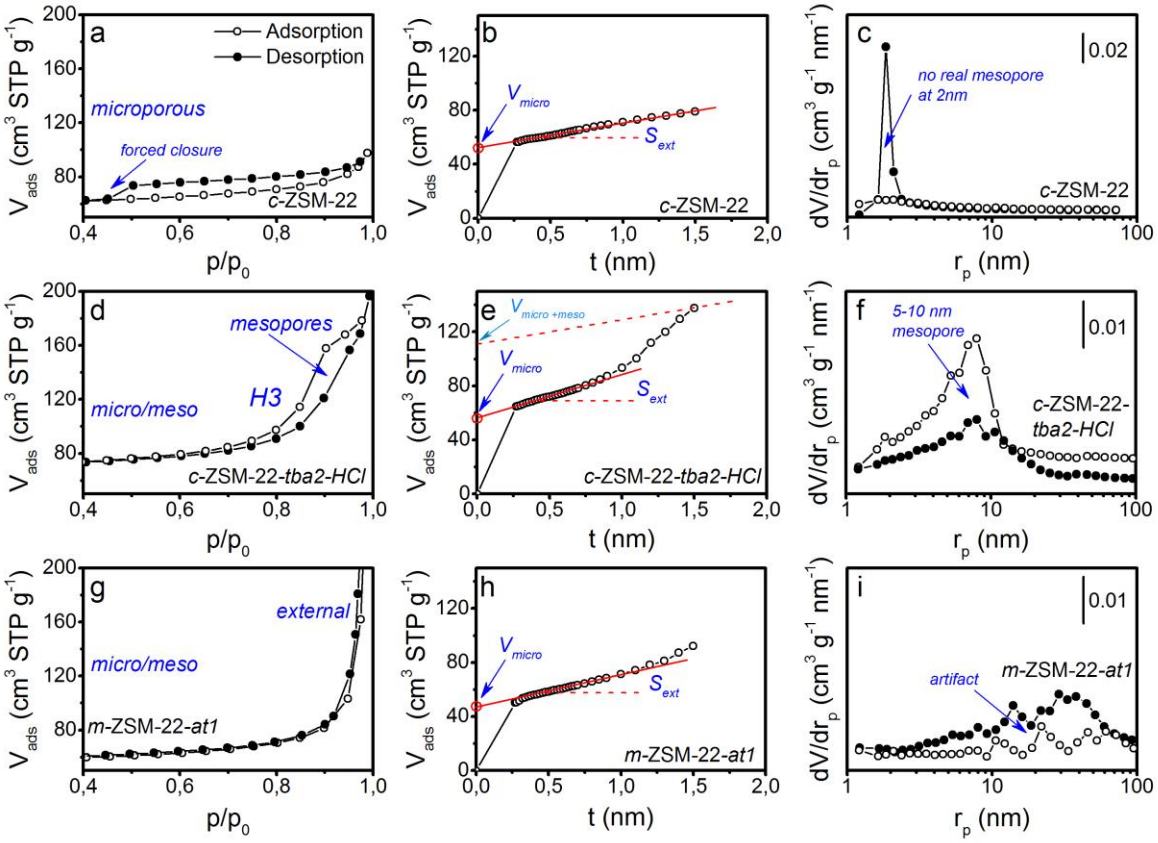

Figure 4.4. Nitrogen physisorption isotherms (**a**, **d**, **g**), *t-plot* (**b**, **e**, **f**) and BJH pore size distribution analysis (**c**, **f**, **i**) for a microporous zeolite (**a** – **c**), for a micro/mesoporous zeolite with intra-crystalline mesopores (**d** – **f**) and for a micro/mesoporous fragmented zeolite with inter-crystalline mesopores (**g** – **i**).

Surface area analysis

The BET (Brunauer, Emmett and Teller) method was applied to obtain the specific or BET surface area, $\boldsymbol{S_{BET}}$ (m^2/g). Evaluation of S_{BET} involves two steps. First, the physisorption N2 isotherm is transformed to the so-called BET plot by using the BET equation (**2**):

$$\frac{\mathbf{1}}{\boldsymbol{n}[(\boldsymbol{p_0}/\boldsymbol{p})-\mathbf{1}]} = \frac{\mathbf{1}}{\boldsymbol{n_m C}} + (\boldsymbol{p}/\boldsymbol{p_0})\frac{\boldsymbol{C}-\mathbf{1}}{\boldsymbol{n_m C}} \qquad (\mathbf{2})$$

where

- $\boldsymbol{n}$ is the adsorbed amount
- $\boldsymbol{n_m}$ is the monolayer capacity (adsorbed amount in one monolayer)
- $\boldsymbol{C}$ is an empirical constant which gives an indication of the order of magnitude of the attractive adsorbent-adsorbate interactions

The linearization of the BET equation allows obtaining the monolayer capacity ($\boldsymbol{n_m}$) from the slope and the intercept of the linear regression curve.

The specific surface area ($\boldsymbol{S_{BET}}$) is the calculated from the monolayer capacity ($\boldsymbol{n_m}$) by the application of the following equation (**3**):

$$\boldsymbol{S_{BET} = n_m \cdot L \cdot \sigma} \qquad \textbf{(3)}$$

where

- $\boldsymbol{L}$ is the Avogadro constant
- $\boldsymbol{\sigma}$ is the cross-sectional area (average area occupied by each adsorbed molecule in a complete monolayer). $\boldsymbol{\sigma}$ (N_2) = 0.162 nm^2

The BET method is applicable for surface area determination of mesoporous materials, but is in a strict sense not applicable for microporous materials since they do not fulfil all the boundary conditions for multilayer adsorption [165]. However, if the BET equation is applied within its classical range ($\boldsymbol{p/p_0}$ = 0.05–0.3) on adsorption data of a microporous material, a linear range is difficult to find and the $\boldsymbol{C}$ constant may be negative, with has no physical meaning. In such case, the BET area depends on the selected data points and the obtained value is considered an apparent or equivalent $\boldsymbol{S_{BET}}$ [165]. In this respect, Rouquerol *et al.* [168] suggested a consistency criteria for the determination of the correct linear range. The first consistency criterion states that the entire $\boldsymbol{p/p_0}$ range used for the BET analysis must be lower than the value from which the $\boldsymbol{V_a(1 - p/p_0)}$ curve starts to decrease. The second criterion states that the value for $\frac{\boldsymbol{1}}{\sqrt{\boldsymbol{C+1}}}$ must be equal to 0.087 within the chosen $\boldsymbol{p/p_0}$ range. The value of the $\boldsymbol{C}$ constant must be positive to fulfil the third criterion.

The use of the standard nitrogen cross-sectional area (assuming spheres) results in overestimated $\boldsymbol{S_{BET}}$ values, since the quadrupole moment of nitrogen leads to specific interactions with polar groups of the zeolite surface (hydroxyl groups, silanols, defects). Consequently, the effective cross-sectional area of adsorbed nitrogen might be smaller than the usual value [166].

Micropore volume and external surface area

The *t-plot* method developed by Lippens and de Boer [169, 170] was used to determine the micropore volume and external surface area (the surface area of all the pores larger than micropores) of the zeolites. This method is based on a comparison plot constructed from a standard isotherm. The standard isotherm is the adsorption isotherm of a nonporous adsorbent. It is ideally best to use a standard isotherm of a nonporous material with surface chemical properties equal to those of the sample under study. Therefore, the best is to select a standard isotherm with similar $\boldsymbol{C}$ constant to the sample isotherm, but this is difficult to achieve. Instead, the BEL Japan software employs the standard isotherm of *de Boer*, which is an average value calculated from various reference isotherms and give acceptable results.

The *t-plot* is constructed by plotting the statistical thickness $\boldsymbol{t}$ (nm) of the adsorbed layer, *i.e.* the adsorbed volume for unit surface, against the adsorbed amount, $\boldsymbol{V_a}$ (cm^3/g). First, the adsorbed amount ($\boldsymbol{V_a}$) of the standard isotherm is converted to the statistical thickness ($\boldsymbol{t}$) with equation (**4**).

$$\boldsymbol{t} = \frac{\boldsymbol{V_a}}{\boldsymbol{V_m}}\boldsymbol{\sigma_t} \qquad (\mathbf{4})$$

where

- $\boldsymbol{\sigma_t}$ is the thickness of a single adsorbed layer. $\boldsymbol{\sigma_t}(N_2)$ = 0.354 nm assuming hexagonal arrangement of N_2 molecules
- $\boldsymbol{V_m}$ is the volume adsorbed in one monolayer

Then, $\boldsymbol{p/p_0}$ is transformed into $\boldsymbol{t}$, so the abscissa of the *t-plot* is expressed by $\boldsymbol{t}$ instead of $\boldsymbol{p/p_0}$. For a nonporous adsorbent isotherm described by multilayer adsorption (type II according to IUPAC classification), the *t-plot* is a straight line passing through the origin and with the slope directly proportional to the surface area of the material. Zeolites as microporous adsorbents show a deviation from the linearity. Different deviation gives information on the type of pores, pore volume and specific surface areas. After the complete filling of the micropores, a straight line with the slope corresponding to the external surface area, $\boldsymbol{S_{ext}}$ (m^2/g) is obtained. The extrapolation of the linear region gives a positive intercept corresponding to the adsorbed volume employed to fill the micropores, so the micropore volume, $\boldsymbol{V_{micro}}$ (cm^3/g) (Figure 4.4b, e, h). For mesoporous zeolites with intra-particle mesopores, an upward

deviation from the linearity due to capillary condensation is expected. After the filling of the mesopores a second straight line with the slope corresponding to the lower external or mesopore surface area and intercept corresponding to the mesopore plus micropore volume has to be expected. If the crystallite size remains the same during the formation of mesopores the difference between the external surface areas of the parent and the treated zeolite is the surface area of the mesopores created. However, for most of the micro/mesoporous zeolites investigated in this work this second linear range was too short (Figure 4.4e) and did not allow the proper analysis. Besides, a number of treatments resulted in variation of the crystal morphology showing practically no hysteresis loop and limited upward deviation from the linear curve, as seen with the sample in Figure 4.4h. Bearing that in mind, the textural properties of the zeolites were determined as:

- $\boldsymbol{V_{ext}}$ (cm^3/g) = $\boldsymbol{V_{pore}}$ (from the adsorbed volume at $\boldsymbol{p/p_0}$ ~ 0.99) – $\boldsymbol{V_{micro}}$(from the 1st linear *t-plot*)
- $\boldsymbol{S_{micro}}$ (m^2/g) = $\boldsymbol{S_{BET}}$ – $\boldsymbol{S_{ext}}$(from the 1st linear *t-plot*)

Along this thesis, S_{ext} and V_{ext} will be used to refer to the surface area or volume of the pores larger than the micropore size (> 2 nm).

Pore size distribution (PSD) analysis

The size of the mesopores was evaluated with the Barett-Joyner-Halenda (BJH) method [171]. This method is based on the Kelvin equation to describe the multilayer adsorption/capillary condensation process occurring in the mesopores. The Kelvin equation correlates the pore condensation pressure with the meniscus and pore radius at the liquid-gas interphase in narrow pores (Figure 4.5). For cylindrical pores, the modified Kelvin equation (**5**) is:

$$\boldsymbol{ln\frac{p}{p_0} = \frac{-2\gamma cos\theta}{RT\Delta\rho\, r_k}} \qquad \textbf{(5.1)}$$

$$\boldsymbol{ln\frac{p}{p_0}\,(\theta = 0) = \frac{-2\gamma V_M}{RT\, r_k}} \qquad \textbf{(5.2)}$$

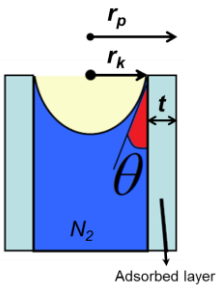

Figure 4.5. Meniscus at the L-G interphase in cylindrical narrow pore.

Adapted from [165].

where

- γ is the surface tension of the bulk N_2

- $\boldsymbol{\Theta}$ is the contact angle of the liquid meniscus against the pore wall. $\boldsymbol{\Theta} = 0^{o}$ (complete wetting of the wall) is usually assumed
- $\boldsymbol{\Delta\rho}$ is the difference between the coexistent liquid ($\boldsymbol{\rho_l}$) and gas ($\boldsymbol{\rho_g}$)
- $\boldsymbol{r_k} = (\boldsymbol{r_p} - \boldsymbol{t_c})$ is the Kelvin radius: radius of curvature of the meniscus formed in the pore; $\boldsymbol{r_p}$ is the pore radius; $\boldsymbol{t_c}$ is the thickness of an adsorbed multilayer film formed prior to pore condensation

During capillary condensation the gas phase nitrogen molecules increased the number of van der Waals interactions between each other and condense to a liquid-like phase. This results in increased adsorbed volume at lower pressures than the saturation pressure of nitrogen. During evaporation, capillary forces must be overcome and nitrogen gas leaves the pore at lower pressure than it entered. The different mechanisms of adsorption desorption results in the formation of the hysteresis loop. The Kelvin equation predicts that condensation in the narrow pore shifts to a higher relative pressure with increasing pore diameter. Therefore, from this equation and the results provided by the sorption methods it is possible to estimate the PSD of the mesoporous zeolite. First, the pore radius ($\boldsymbol{r_p}$) is obtained from the Kelvin radius ($\boldsymbol{r_k}$) plus the multilayer thickness ($\boldsymbol{t_c}$), often obtained from BET method results. Once the pore radius is calculated, the change in volume per change in pore radius ($\boldsymbol{dV_p / dr_p}$) is plotted against $\boldsymbol{r_p}$ (Figure 4.4c, f, i). The $\boldsymbol{dV_p / dr_p}$ represents the slope of the change in volume of adsorbate for the corresponding pore with radius $\boldsymbol{r_p}$.

The assumptions of the BJH method (regular pore shape, complete wetting, filling/emptying independent of the position, adsorption in pore walls similar to open surface) are often not fully validated. In addition, the Kelvin equation fails to describe correctly the behaviour of critical regions and confinement effects in the pores. Indeed, the method may underestimate the pore size by a factor up to 20–30 % for pores smaller than 15 nm, due to the fact that the assessment of the statistical thickness becomes problematic when the pore diameter decreases [166]. Therefore, the BJH method should be taken as estimation of the PSD.

Additionally, the analysis should be made carefully as often there are misinterpretations in the mesopore size distribution derived from nitrogen adsorption measurements using the BJH method. For instance, the area between 2 and 4 nm is prone to errors if a hysteresis loop with a forced closure is present [172, 173]. In this case, a large amount of nitrogen is released at once between $\boldsymbol{p/p_0}$ of 0.38-0.44, which is visible as the closing of the hysteresis loop. The

BJH analysis correlates then the volume of the released N_2 to pores of 2-4 nm via the Kelvin equation, but this is not always correct. Real mesopores should lead to reversibility for both the adsorption and desorption branches. The sample *c*-ZSM-22, with nitrogen isotherm and BJH plot showed in Figure 4.4a and c, serves as an example. In this case, the sharp peak at 2 nm observed in the BJH mesopore size distribution calculated with the desorption branch is not present when using the adsorption branch and, hence, does not indicate real mesoporosity. Additionally, inkbottle pores with pore necks smaller than 4 nm might release nitrogen between relative pressures of 0.38-0.44. The determination of the mesopore size distribution should be accompanied with TEM images to avoid misinterpretations.

Furthermore, zig-zag curves observed in the large pore region of the BJH plot (Figure 4.4i) do not represent true mesoporosity but is considered an artifact of the analysis. As mentioned, the BJH pore size distribution is the first derivative of the accumulative volume. Then, a very small jump in the isotherm could give a sharp increase in the BJH but without any significance when it occurs between 2 consecutive points.

4.3.6. Infrared Spectroscopy (IR)

Nature and concentration of acid sites

The nature and concentration of the acid sites in the protonated zeolites was investigated using Fourier Transformed Infra-red (FTIR) spectroscopy. The interaction of the active sites with probe molecules such as CO and pyridine was studied to determine the type, strength and concentration of the active site.

FTIR spectra were collected on a Bruker Vertex 80 instrument with MCT detector, working at 2 cm^{-1} resolution and a number of 32 or 64 scans. An in-house designed quartz sample cell with KBr windows was employed for the measurements.

Zeolite powder was pressed into self-supporting wafers, put in a golden envelope and placed in the measuring cell. Samples were pre-treated under vacuum for 3h: at 150 °C for 1 h, at 300 °C for 1 h and at 450 °C for 1 h. CO was adsorbed on the sample at liquid nitrogen temperature (77 K). After dosing, CO was gradually pumped out of the cell while spectra were recorded at regular intervals. The spectra were normalized to the overtone modes at wavenumber 1750–2000 cm^{-1}. Quantification of the acid sites was performed by adsorption of

pyridine at room temperature, followed desorption and evacuation *in-situ* at 200 °C for 2 h under vacuum, in order to remove the physisorbed species. All spectra were corrected for water and CO_2 present in the sample compartment.

The absorbance for IR radiation was checked for all the activated samples to ensure the absence of water, which should be seen as a flat curve in the 3300-2500 cm^{-1} frequency range (Figure 4.6). Typically, two features are distinguished in the OH stretching region of the activated zeolite: an asymmetric band at 3745 cm^{-1} and a broader band centered at 3600 cm^{-1}, corresponding to the mode of isolated external silanols and BAS, respectively [12, 174, 175] (Figure 4.6 top inset). The band associated with the isolated silanols generally exhibits a tail on the lower frequency side, indicating the existence of silanol groups in different framework environments (internal and perturbed) [14, 175].

Adsorption of CO at 77 K reveals the existence of different types of acid sites. The interaction of CO with the bridging hydroxyl results in a decrease in the intensity at 3600 cm^{-1} concomitant of the appearance of broad band at 3280 cm^{-1} (Figure 4.6 top insets). This shift can be considered as an estimation of the acid strength of zeolite. Upon increasing CO dosage, the band associated with isolated silanols also shifts to lower wavenumbers (Figure 4.6 top insets). Upon CO dosage, bands at 2174 cm^{-1} and at 2160 cm^{-1} in the CO stretching region (Figure 4.6 bottom insets), corresponding to CO interacting with the BAS and with silanol groups, respectively, are typically observed. The sharp band at 2138 cm^{-1} is assigned to liquid-like CO phase condensed into the zeolite pores [12].

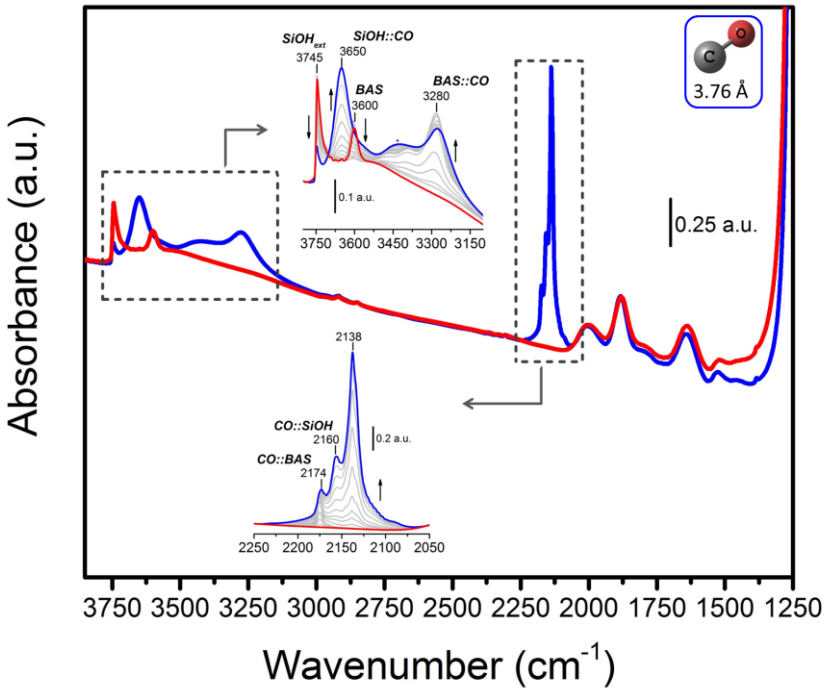

Figure 4.6. FTIR spectra of a H-ZSM-22 zeolite interacting with CO. Spectra after activation at 450 °C (red line) at RT and after maximum CO dosage (blue line) at liquid nitrogen T. The insets shows FTIR spectra in the hydroxyl (**top**) and CO (**bottom**) stretching region collected while outgassing CO from maximum (blue line) to minimum coverage at liquid nitrogen T; grey lines correspond to intermediate CO coverages.

The concentration and accessibility of Brønsted and Lewis acid sites was determined by pyridine adsorption monitored by FTIR. Complete consumption of the BAS band at 3600 cm^{-1} (Figure 4.7) is expected when all the BAS are accessible to pyridine. The concentration of Brønsted and Lewis acid sites was obtained by the integration of the bands at 1545 cm^{-1} and 1455 cm^{-1} (Figure 4.7a) [176], respectively, and from the values of the extinction coefficients using equations (**6**) and (**7**).

$$[\boldsymbol{BAS}]\left(\frac{\boldsymbol{mmol}}{\boldsymbol{g}}\right) = \frac{\boldsymbol{IA_{1544}} \cdot \boldsymbol{Area_{wafer}}\,(\boldsymbol{cm^2})}{\boldsymbol{\varepsilon_{BAS}}(\mathbf{0.73}) \cdot \boldsymbol{Mass_{wafer}}(\boldsymbol{mg})} \qquad (\mathbf{6})$$

$$[\boldsymbol{LAS}]\left(\frac{\boldsymbol{mmol}}{\boldsymbol{g}}\right) = \frac{\boldsymbol{IA_{1452}} \cdot \boldsymbol{Area_{wafer}}\,(\boldsymbol{cm^2})}{\boldsymbol{\varepsilon_{LAS}}(\mathbf{0.64}) \cdot \boldsymbol{Mass_{wafer}}(\boldsymbol{mg})} \qquad (\mathbf{7})$$

Pyridine adsorption analysis may underestimate the acid site density. This is due to the fact that the diffusion of pyridine (5.7 Å) within the zeolite pores might be sterically limited, since it is similar to the maximum channel opening of ZSM-22 and ZM-23 (Section 1.3).

Accessibility and diffusion

The accessibility and diffusion properties of the zeolites were investigated with time-dependent uptake of toluene monitored by IR.

The measurements were carried out in a flow-through transmission cell connected to the feeding system. The IT cell allowed continuous heating and cooling of the sample. The IR measurements were performed on a Bruker Vertex 70 instrument with MCT detector.

The sample was pressed into a self-supporting wafer and placed on the sample holder inside the transmission cell. Before the experiments, evacuation of the cell and activation the sample was performed overnight at 450 ^{o}C using a nitrogen flow of 10 mL/min. The temperature was lowered to 100 ^{o}C keeping the pure nitrogen stream. The partial pressure of toluene in nitrogen was adjusted to 0.1 mbar. The uptake of toluene was monitored by collecting the IR spectra with a time resolution of 2 sec.

The intensity of the IR band at 1495 cm^{-1} corresponding to the interaction with toluene (Figure 4.7b) was used to quantify the amount of toluene adsorbed per mass of zeolite catalyst.

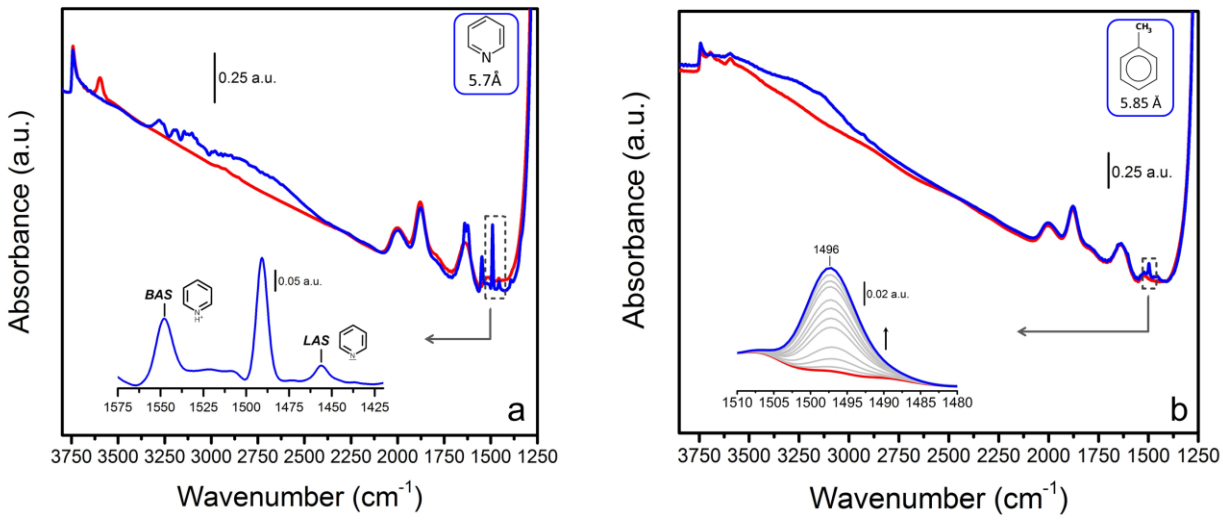

Figure 4.7. FTIR spectra of a H-ZSM-22 zeolite interacting with pyridine (**a**) and toluene (**b**). (**a**) Spectra after activation at 450 ^{o}C (red line) and after pyridine adsorption (blue line) at rT. The inset shows FTIR spectra in the pyridine region at maximum pyridine coverage. (**b**) Spectra after activation (red line) and after maximum toluene uptake (blue line) at 100 ^{o}C and 0.1 mbar. The insets shows FTIR spectra in the toluene region collected while dosing toluene up to a maximum (blue line); grey lines correspond to intermediate coverages.

4.3.7. Additional characterization

Temperature Programmed Desorption (TPD)

TPD of *n*-propylamine was used to determine the number of acid sites on *c*-ZSM-22 and *c*-ZSM-22-*ats1-HCl* catalysts (only in **Paper I**). The Si/Al ratio was estimated assuming that one propylamine molecule interacts with Al substitution to produce ammonia and propene [177]. However, propylamine cannot read Al atoms that not incorporated in the zeolite lattice.

15 mg of catalyst were place in an 11 mm glass reactor and pretreated in a flow of oxygen at 550 ^{o}C for 1 h, before cooling to 150 ^{o}C. A stream of 50 ml/min of nitrogen bubbled through *n*-propylamine at room temperature was then fed over the catalyst for 30 min in order to adsorb the amine at 150 ^{o}C. After this, the catalyst was left at 150 ^{o}C for 4 h in a stream of 80 ml/min nitrogen to desorb the excess of amine. The temperature was then increased up to 550 ^{o}C with a heating ramp of 20 ^{o}C/min and kept at this temperature for 30 min. The amount of propene desorbed was quantified using an on-line Pfeiffer Omnistar quadrupole mass spectrometer.

Thermogravimetric Analysis (TGA)

TGA was used to determine the amount and stability of the oxidable coked species retained in the pores of the relevant deactivated catalysts investigated in **Paper I** and **Paper III**. The thermogravimetric measurements were carried out using a Stanton Redcroft TGA-DSC instrument.

Approximately 15-20 mg of coked sample was loaded in a Pt crucible. The sample was heated from room temperature up to 800 ^{o}C at a rate of 5 ^{o}C/min. Then the temperature was kept at 800 ^{o}C for 40 min. The measurements were performed under a constant and simultaneous flow of 20 mL/min nitrogen and 5 mL/min oxygen while the mass loss was being acquired.

4.4. Operando High Energy XRD (HXRD)

Time- and space-resolved HXRD patterns were acquired at real time (*operando*) reaction conditions. The method was used to investigate the unit cell variations of the catalyst during the MTH reaction over H-ZSM-22 catalyst in different conditions (**Paper I**). *Operando* X-Ray synchrotron radiation based powder diffraction patterns (PDP) were collected on BM01A of the Swiss-Norwegian Beam Line (SNBL) at the European Synchrotron Radiation Facility (ESRF).

All the PXRD data were acquired and processed by David Wragg and Wojciech A. Slawinski. The PXRD data was acquired by a Pilatus 2M detector and integrated into a 1D powder diffraction pattern. The wavelength used was 0.69811 A. The scattering vector length Q, covered by the experiment was 0.43 $Å^{-1}$ < Q < 4.50 $Å^{-1}$. During data collection the reactor was moved back and forth through the beam. Individual PDPs were measured in 10-13 positions of the reactor with a time resolution of approximately 180 sec. The reactor was then moved back with no data collection. The observed Bragg reflections showed significant broadening due to the large dimension of the reactor bed. The experimental setup used at the ESRF is schematically presented in Figure 4.8.

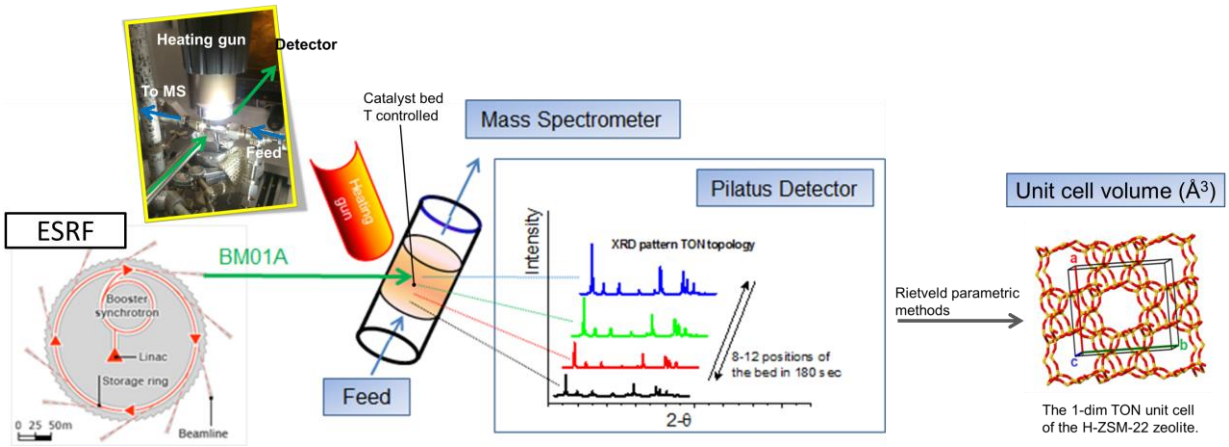

Figure 4.8. Scheme of the process for simultaneous acquisition of HXRD and catalytic data at synchrotron facilities.

A separate experiment for the precise calculation of the unit cell temperature dependence was performed in a 0.6 mm quartz capillary with standard hot air blower. The data collected with this experiment assessed whether the unit cell variation was due to a thermal expansion or to an accumulation of HCP species during the MTH reaction.

The PXRD structure refinement was done by David Wragg and Wojciech A. Slawinski. The collected PDPs were analysed using Rietveld method implemented in FullProf program. For each individual position of the reactor bed we refined PDPs in sequential mode. The crystal structure of H-ZSM-22 samples was described in Cmcm space group. The *a*, *b* and *c* unit cell parameters, common isotropic temperature factor for Si and O atoms were refined. The observed peak shape was described using Pseudo-Voigt function and for peak width angular dependence the Caliotti formula was used. We also used peak asymmetry correction below 8 deg. All atomic positions were fixed. In case of the analysis of the small capillary experiment (thermal expansion of the unit cells) also atomic positions were refined.

4.5. Catalytic testing

4.5.1. Catalytic testing at home laboratory

All MTH catalytic tests were performed over acidic ZSM-22 and ZSM-23 catalysts at 400 ^{o}C and WHSV ≈ 2 $gg^{-1}h^{-1}$, except for the catalytic tests performed at similar conditions (375 ^{o}C and WHSV ≈ 2 $gg^{-1}h^{-1}$) to those used at the ESRF. These tests were performed to confirm the differences in catalytic performance observed for the catalysts under *operando* conditions (370-385 ^{o}C) than those observed at 400 ^{o}C. Most of the experiments in this thesis involve only methanol as a reactant, whereas experiments carried out in **Paper I** also involve the co-conversion of methanol and isopropanol. The experiments were performed using a reactor system schematically presented in Figure 4.9.

The reactor system is equipped with five supply lines: Line 1 to 5. Lines 1 to 4 are connected to helium and line 5 is connected to oxygen. Lines 1 and 2 were fitted with saturation evaporators allowing the feeding of the liquid reactants. Saturator connected to line 1 was filled with methanol (BDH Laboratory Supplies, >99.8 %) and saturator connected to line 2 was filled with isopropanol (Sigma Aldrich, >99.8 %). Helium from line 3 was used during heating and cooling cycles. The flow of gases was regulated by Porter P-150 ball flowmeters

and measured using ADM2000 Universal flowmeter (Agilent Technologies). Desired reactant flow rates (WHSV) were established by adjusting the carrier gas flow and temperature of the water bath surrounding the saturators. The temperature of the oven was monitored using a thermocouple fixed inside the oven.

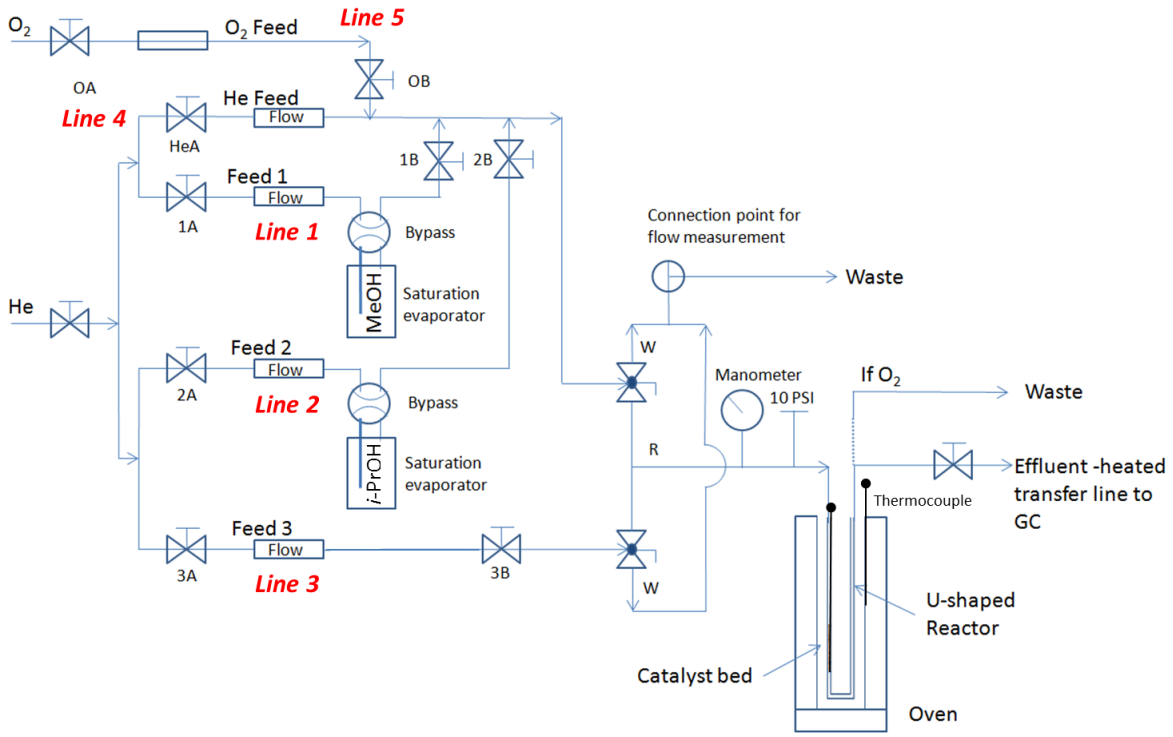

Figure 4.9. Schematic representation of the reactor system for catalytic experiments carried out at home laboratory.

Catalytic testing experiments were performed at ambient pressure using 50 mg of sample in a fixed-bed quartz reactor with 10 mm diameter. The protonated zeolite was pressed into wafers, crushed and sieved to obtain particles in the 250-420 μm range before transferring it to the reactor. Before each catalytic experiment the samples were calcined in situ in a flow of pure oxygen at 550 ºC for 1 hour in order to remove species adsorbed during catalyst handling and storage. Methanol was fed by passing helium through a saturation evaporator kept at 20 ^{o}C (p_{MeOH} = 130 mbar) to the inlet of the reactor. The temperature of the reaction was monitored using a thermocouple with a quartz thin cover inserted at the bottom of the catalyst bed. The product stream was analysed online using an automatic injection Gas Chromatograph (GC) connected to the reactor outlet by a heated transfer line. An Agilent 6890N GC with FID,

equipped with a HP-PLOTQ capillary column (15 m, 0.320 mm i.d. film thickness 20 µm) was used for the analysis. The temperature of the GC oven was programmed between 90 and 270 ^{o}C with a heating rate of 20 ^{o}C/min (hold time of 5 min at 90 ^{o}C and at 220 ^{o}C and 9 min at 270 ^{o}C).

For the co-feeding experiments isopropanol was used as a precursor for propene. The reactants were fed from two different saturators at 20 ^{o}C each containing methanol or isopropanol, using He as carrier gas. The partial pressure of the reactants was p_{MeOH} = 130 mbar and $p_{\mathrm{i\text{-}PrOH}}$ = 13 mbar and the total He flow 10 ml/min.

Methanol conversion (*X*), product selectivity (*S*) and product yield (*Y*) were calculated from GC-FID areas, following the equations (**8**)-(**10**) shown below. Methanol and dimethyl ether (DME) were considered as reactants, while all effluent non-oxygen hydrocarbons were considered reaction products. Appropriate response factors were used for the integrated peak areas for methanol (0.776) and DME (0.598). No correction was employed for the integrated peak areas of the hydrocarbons.

$$X_i(\%) = \frac{area\ of\ HC\ product\ peaks}{total\ peak\ area} \times 100 \qquad (\mathbf{8})$$

$$S_i(\%) = \frac{area\ of\ HC\ product\ peak\ i}{area\ of\ HC\ product\ peaks} \times 100 \qquad (\mathbf{9})$$

$$Y_i(\%) = \frac{area\ of\ HC\ product\ peak\ i}{total\ peak\ area} \times 100 \qquad (\mathbf{10})$$

For the reaction involving co-conversion of methanol and isopropanol, product molecules cannot be used for the calculation of conversion due to the presence of reactants in both reactant and product streams. The area of oxygenates (methanol and DME) over the fully deactivated catalyst was used as a reference area (A_{ref}). The conversion is then calculated as follows.

$$X\ (\%) = 100 - \frac{corrected\ peak\ area\ (MeOH\ and\ DME)}{A_{ref}} \times 100 \qquad (\mathbf{11})$$

Note that this procedure implies an increasing uncertainty in the calculated conversion at decreasing conversions. The distributions of hydrocarbon products in the effluent were reported as reactor outlet composition in C%, due to the complications caused by the presence of alkenes in both the reactant and the product streams.

4.5.2. Catalytic testing at ESRF

The catalytic setup constructed at the SNBL at ESRF (Figure 4.8) allowed to simultaneously monitor the catalyst activity and unit cell volume variations by time- and space-resolved HXRD in *operando* conditions.

The ESRF laboratories were equipped with a gas panel, which allowed using different lines and reaction gases from the SNBL gas mixing system. The testing conditions were adjusted to be the same as the ones described for the experiments at our home laboratories with some distinctions that are now described. Catalyst sieved powder samples (50 mg) were placed between two layers of quartz wool in a specially prepared quartz cylindrical reactor with a diameter of 10 mm. Reaction gases (helium, oxygen diluted in helium or helium bubbled through methanol or isopropanol saturators at 20 ^{o}C with a temperature difference of 1 ^{o}C) with the desired flow rate were fed to the reactor. The reactor was mounted horizontally on a Huber stage capable of translations in the flow direction. The setup was connected on one side (inlet) with a T-connection (allowing feed of the reactants) to a Huber goniometer head used for alignment, and on the other side (outlet) to a locally heated transfer line connected to a Pfeiffer Omnistar MS. The reactor zone was heated with a Leister LE mini heating gun fitted with heat spreader to keep the temperature at 370-385 ^{o}C. The temperature along the horizontal catalytic bed was measured by inserting a thermocouple into the center of the sample and varied in a range of 15 ^{o}C between the extremes and center of the reaction zone.

When the experiments were carried out only with methanol, a flow rate of 10 ml/min was used. For the co-feed experiments the flow rate of methanol and isopropanol were adjusted to 10 and 3 ml/min, respectively, to reach a total WHSV of 2 $gg^{-1}h^{-1}$. After the reaction, the deactivated samples were gently divided in 3 segments (inlet-middle-outlet) and collected to further analysis. For the reactions involving only methanol, the conversion was calculated from the methanol signal in the MS normalized by the helium signal as follows:

$$X\ (\%) = 100 - \frac{MeOH_t - MeOH_{min}}{MeOH_{max} - MeOH_{min}} \times 100\% \qquad (\mathbf{12})$$

The signal-to-noise ratio of the MS data was rather high. Therefore, selected data points representative of the deactivation trend were chosen and the resulting curve was smoothed to facilitate interpretation.

For the reaction involving co-conversion of methanol and isopropanol, the conversion was calculated in the same way from the methanol signal, since calculations using A_{ref} from MS data gave too low signal-to-noise ratios.

4.5.3. Analysis of the retained species

The identity and distribution of the hydrocarbon species retained in the catalyst pores after reaction was carried out by dissolving the coked catalyst and analysing it on an offline Gas Chromatography-Mass Spectrometer (GC-MS).

Retained hydrocarbons were investigated by dissolution experiments. Approximately 15 mg of coked zeolite was dissolved in a small capped Teflon vial with 1 ml 15 wt% HF (Fluka, 40 %). Addition of 1 ml of dichloromethane (Merck, > 99 %) with o-chlorotoluene as internal standard allowed the extraction of the organic phase for further analysis by GC-MS. An Agilent 7890A GC connected to an Agilent 5975C mass-selective detector with a HP-5MS column (60 m, 0.25 mm i.d., stationary phase thickness 0.25 µm) was used for the analysis. The temperature of the oven was programmed between 50 and 300 ^{o}C with a heating rate of 10 ^{o}C/min (hold time of 3 min at 50 ^{o}C and 15 min at 300 ^{o}C). The mass spectral library of the NIST98 database was used for identification of the retained species.

5. Summary of Results

As stated in the Scope, this chapter summarizes the main results obtained during this Ph.D. work. Rather than presenting the papers in chronological order, the results are presented in the most natural order to allow a consistent follow-up of the work. Furthermore, this chapter briefly presents results that have not been submitted to publication, but contribute to the rest of the work. Detailed discussion of the results and additional graphs are provided in the papers attached as an appendix to the Thesis. The chapter is divided into four sections.

Section 5.1 provides the principal results from the extensive investigation of the preparation of a large body of desilicated ZSM-22 zeolites and their characterization (reported in **Paper II**). The properties of the zeolites were studied using two different parameters: the features of the starting zeolite (commercial or in house synthesized) and the desilication method employed for the creation of mesopores (NaOH, mixtures of CTAB/NaOH and mixtures of TBAOH/NaOH), followed by acid washing. The composition, morphology, textural and acidity modifications are investigated with particular emphasis in the mesopore development.

In Section 5.2, the performance of the mesoporous H-ZSM-22 materials as improved catalysts for the MTG conversion is investigated. An attempt is made to correlate the catalytic performance to the characterization data from Section 5.1 and also to diffusion and accessibility features based on additional spectroscopic methods. The influence of the post-synthetic treatments on the catalytic lifetime and total conversion capacity, as well as on the product distribution and mechanisms of the MTH reaction is examined. **Paper III** forms the basis of this section. In addition, the main results from the structure-deactivation relations obtained by time- and space-resolved *operando* HXRD studies over commercial H-ZSM-22 catalysts and the effect of surfactant-assisted desilication and acid washing as well as the effect of product co-feed are presented as a summary of the work carried out in **Paper I**. The effect of internal silanol defects on the catalytic performance is also investigated.

The main body of this work comprises the studies on ZSM-22 zeolites. In Section 5.3 the preparation, characterization and catalytic investigations are extended to the also unidimensional ZSM-23 zeolite with MTT topology.

5.1. Effect of the post-synthetic modifications on the catalyst properties

5.1.1. Relevance of the starting material on the mesopore generation

As mentioned in Chapter 3, the composition and crystal morphology of the starting zeolites may strongly influence the extent of crystal dissolution upon desilication and the resulting pore structures. Two parent ZSM-22 zeolites, the commercial *c*-ZSM-22 and the in house prepared *m*-ZSM-22, are the starting materials for this study. In Section 4.3 it was confirmed that both samples consist of a highly crystalline TON structure.

Both *c*-ZSM-22 (Si/Al = 49) and *m*-ZSM-22 (Si/Al = 38) zeolites displays a Si/Al ratio within the optimum for efficient desilication (25–50) as found by Groen and co-workers for MFI zeolites [114]. This implies that the composition of the starting zeolite should not represent an impediment for efficient mesopore formation. As discussed in Section 3.1, the location of gradients in Al concentration in the zeolite crystal may also influence the mechanism of mesopore generation, since mesopores will be preferentially developed from low Al framework environments. However, none of the characterization techniques used in this work was appropriate to identify areas with higher or lower Al concentration within the zeolite particle, and the possible effect, if any, will need to be speculated from the morphology of the already desilicated crystals.

The yields of the desilication treatments (defined as 100 – weight loss % after desilication) are reported in Table A.1 of the Appendix. In principle, the *m*-ZSM-22 zeolite with lower Si/Al ratio is expected to be more difficult to desilicate than *c*-ZSM-22, due to the aforementioned protective effect given by the Al. However, a similar extent of crystal dissolution was obtained independently of the starting material. Overall, the same desilication approach led to similar yields for both the commercial and the in house prepared samples.

With respect to the morphology, differences are found between the two starting ZSM-22 samples. SEM micrographs for the commercial and in house prepared ZSM-22 zeolites are shown in Figure 5.1a and b, respectively. TEM images of the parent zeolites (together with the desilicated samples) are displayed in Figure 5.2. The *c*-ZSM-22 zeolite shows a complex

morphology. The rod-like particles of dimensions of about 2–4 x 0.5 μm appear to be an agglomeration of more defined nanorods with lengths from 600 nm and up to 200 nm in width. These nanorods can be interpreted as the primary particles which are aligned into the rod-like bigger crystals, thus following the mode of crystallization previously described by Hayasaka *et al.* [178]. The *m*-ZSM-22 zeolite displays more defined needle-shaped crystals with a broad distribution of lengths but with regular thickness of about 30–60 nm.

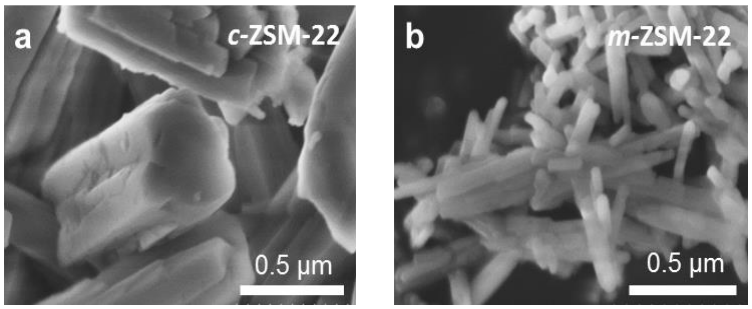

Figure 5.1. SEM images for the commercial *c*-ZSM-22 (**a**) and in house prepared (**b**) parent zeolites.

As one of the main findings of this work, the morphology of the starting zeolite crystal was found to be the dominant parameter which influences the mesopore generation. TEM images of the desilicated zeolites clearly reveal that different zones of the crystal were preferentially dissolved during desilication depending on the starting material. The inner zones of the rod-like *c*-ZSM-22 crystals were the most affected, resulting in the creation of intra-crystalline mesopores. In contrast, the thinner dimensions of the needle-shaped *m*-ZSM-22 particles represent an obstacle for intra-mesopore creation. Instead, the external surfaces of the needle crystals were preferentially affected, resulting in eroded nanoparticles with high exposed surface area. This was obvious when the parent zeolite was treated with CTAB at lower alkaline concentrations (*m*-ZSM-22-*ats2*). Furthermore, the mode of crystal dissolution might also be influenced by an uneven distribution of the Al: a lower Al concentration on the external surface of the *m*-ZSM-22 crystal may result in a lower protective effect against the Si extraction in this zone, as proposed by Dessau *et al.* [115]. The *c*-ZSM-22-*ats2* sample (treated with CTAB/NaOH at high concentration) shows the most clear intra-crystalline mesopores, which are most likely created via selective dissolution of siliceous zones from the bulk crystal. For the rest of the desilicated commercial zeolites, mesopore formation by preferential dissolution along boundaries and framework defects within the crystal, as discussed in Section 3.1, cannot be dismissed.

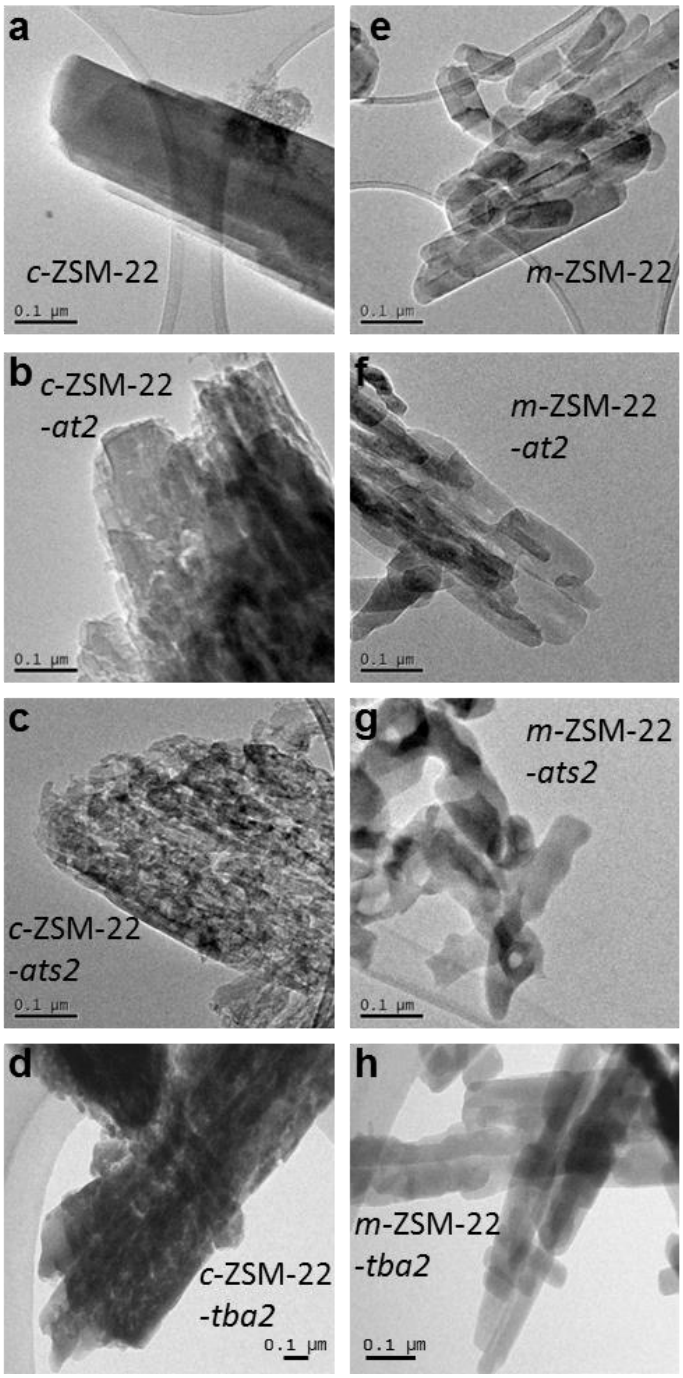

Figure 5.2. TEM images for the parent and desilicated commercial (**left**) and in house prepared (**right**) zeolites.

Framework defects can be identified from the FTIR spectra of the activated zeolite. Previous spectroscopic studies using pyridine and bulky 2,4,6-collidine as probe molecules for determining the location of silanol groups in ZSM-5 [175], concluded that the frequency bands at 3700-3735 cm^{-1} in the activated FTIR spectra are associated with the presence of OH groups interacting weakly with Si in different environments inside the zeolite framework,

which might be present as internal framework defects. Figure 5.3 shows the FTIR spectra of the protonated *c*-ZSM-22 and *m*-ZSM-22 zeolites, together with one sample of each post-synthetic approach activated at 450 °C. The absorbance seen at wavenumbers ranging from 3650 cm^{-1} to 3735 cm^{-1} varies with respect to the starting material. The commercial material has a substantially higher absorbance in this region relative to the in house prepared material, indicating a larger contribution of internal silanols and thus higher amount of defects. Such defects, hence, might initiate the mesopore generation from the commercial ZSM-22 crystal as proposed by Ogura *et al.* [123] and Svelle *et al.* [124], confirming the observations derived from the TEM investigations. Further, the raised baseline seen for the in house prepared zeolite in this region is no longer noticeable for the desilicated samples. Conversely, the intensity was not noticeably reduced, or even increased, after the desilication treatments of the commercial zeolite. A rationalization of this behaviour might be found in the TEM analysis. The shrinking of the thinner, aggregated crystals of the *m*-ZSM-22 zeolite after desilication might also have cleaned up the defects in the micropores near external crystal zones. On the other hand, desilication of the larger *c*-ZSM-22 crystals did not remove the weaker silanols, but resulted in a larger contribution of defects, which might be located on the created mesopore surface inside the zeolite crystal.

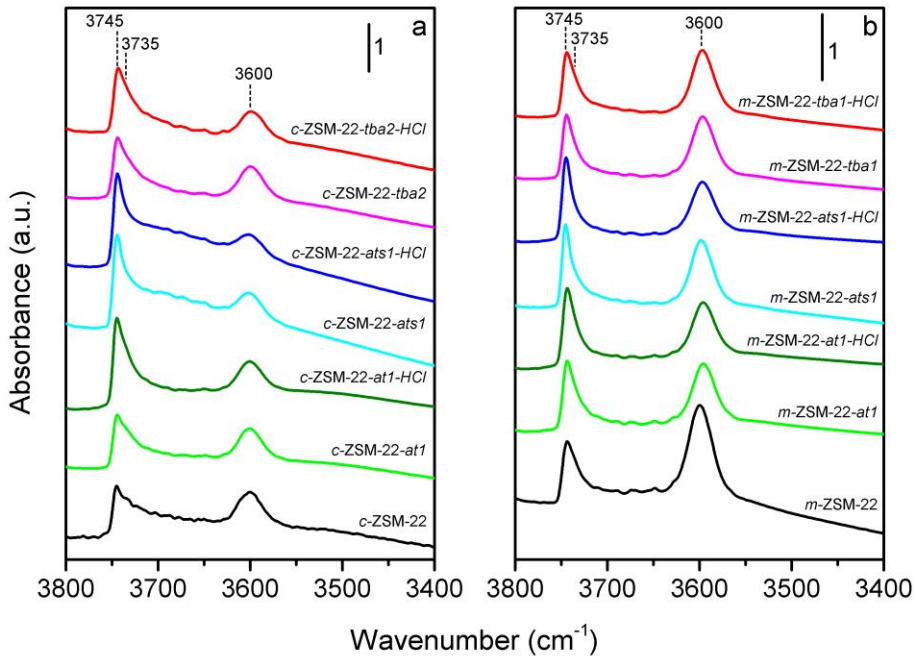

Figure 5.3. FTIR spectra of the parent and post-synthetic treated commercial (**a**) and in house prepared (**b**) ZSM-22 zeolites activated at 450 °C in the hydroxyl stretching region.

As expected for the *m*-ZSM-22, having a lower Si/Al ratio, the intensity of the 3600 cm^{-1} band, associated with the BAS, is larger compared to the *c*-ZSM-22. However, the concentration of Brønsted sites, as determined by IR spectroscopy of adsorbed pyridine (Table A.2 of the Appendix), is the same for both samples. This is a result of the inaccessible microporosity of the *m*-ZSM-22 sample, which might be caused by the presence of stacking faults or MTT/TON intergrowths [179], preventing the diffusion of the probe molecule through the unidirectional channel system. The low micropore volume of the *m*-ZSM-22 sample (Table A.1 of the Appendix) could be also responsible of the lack of intra-crystalline mesoporosity formation upon the treatments, because bases and/or silicates species cannot diffuse freely through the unidirectional channel system.

5.1.2. Effect of the desilication and acid treatments

The PXRD diffractograms (Figure A.1 of the Appendix) confirmed that the crystallinity of the starting zeolites was maintained after the post-synthetic treatments. Some of the XRD patterns show loss of crystallinity. The XRD peak intensities of reflections at 25° diminish in samples *c/m*-ZSM-22-*tba1-HCl*, *c/m*-ZSM-22-*tba2-HCl*, *m*-ZSM-22-*ats2*, *m*-ZSM-22-*ats2-HCl*. Full plate was not used, so the intensities are not fully comparable. As expected, the solid yield was reduced with the severity of the treatment for each desilication series (Table A.1), *i.e.* the more severe treatments led to more extensive crystal dissolution (see References in Table 3.1).

Figure 5.4a presents the variation of the Si/Al ratio as a function of the NaOH molarity for the desilicated samples. The numerical values are reported in Table A.1 of the Appendix. The dashed (reference) curve indicates the Si/Al ratio variation when only NaOH was used as desilication agent. As expected from the similar dissolution rates, also similar reduction of the Si/Al ratio is systematically observed for the commercial and in house prepared materials with increased NaOH concentration. After a drastic reduction of the initial Si/Al ratio upon the mild treatment, the severe NaOH solution reduced the Si/Al to a lesser extent, suggesting an upper limit for Si extraction given by the less severe NaOH concentration. Slightly less pronounced reduction is observed for the in house prepared zeolites, which is an indication of the (little) protective effect of Al in *m*-ZSM-22 against Si-O bond breaking. When CTAB or TBAOH were added to the alkaline solution, the Si/Al ratios deviate from the reference curve, but similar trends are obtained with the commercial or in house prepared samples. The low

concentrated surfactant-assisted approach (*ats1*) leads to Si/Al ratios above the reference curve. Together with the lower yield, this indicates that the crystals were less dissolved upon this treatment, confirming that the surfactant protects the zeolite structure against the attack of the OH^-, as anticipated in Section 3.2. On the other hand, the lower Si/Al ratio achieved at the higher CTAB concentration (*ats2*) compared to the NaOH treatment suggests that the OH^- attack prevails at higher concentrations, and the protective effect of the surfactant is lost. In this case, the dissolved silica aggregates might also be stabilized which in turn shift the equilibrium to further dissolution. With respect to the *tba* treatment, the reduced Si/Al ratio and the highest yields are indicative of a more selective Si removal. The increase of the temperature of the treatment had little impact beyond slightly more Si extraction.

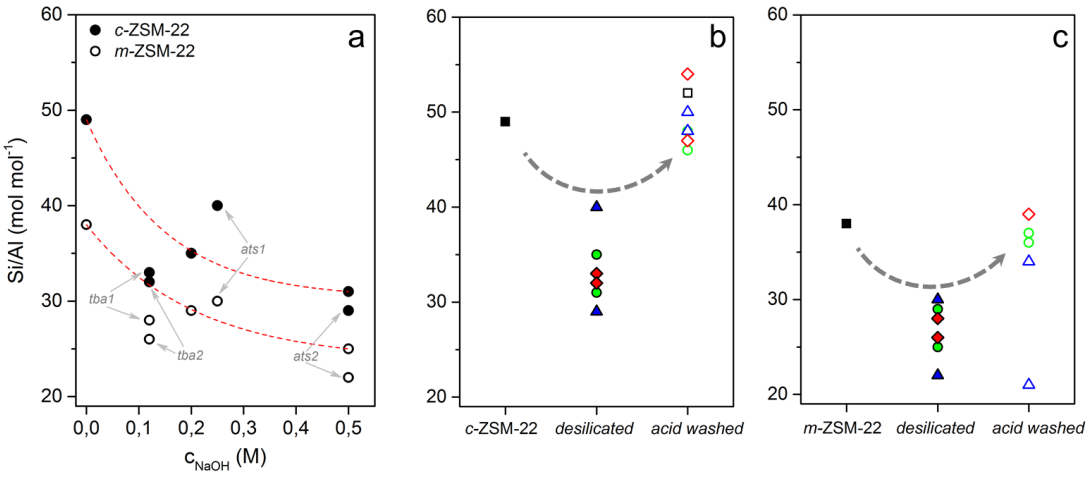

Figure 5.4. (**a**) Si/Al ratio as a function of NaOH molar concentration for the commercial and in house prepared desilicated samples (dashed red curve shows the reference effect of the only alkaline treatment); and Si/Al ratio for the parent, desilicated and acid-washed commercial (**b**) and in house prepared (**c**) zeolites.

Detailed examination of the TEM micrographs shows that the different desilication methods differently influence the mesopore creation for the *c*-ZSM-22 zeolite. The conventional NaOH treatment resulted in both roughening of the crystal surface and creation of non-uniform mesopores (Figure 5.2b), whereas when CTAB (Figure 5.2c) or TBAOH (Figure 5.2d) agent was added to the alkaline solution, well-defined intra-crystalline mesopores were obtained. The crystal edges appear to be less affected in this case, confirming that the addition of PDA provides better control of the mesopore generation, as cited in Section 3.2. TEM observations are supported by the nitrogen sorption measurements. The nitrogen physisorption isotherms and the BJH pore size distribution plots of the parent and post-synthetic treated samples are shown in Figure 5.5 and Figure 5.6, respectively. As seen from

Figure 5.5.a-c, the desilication treatments over the commercial ZSM-22 zeolite led to the transformation of the microporous type I isotherm into type II-IV isotherms with hysteresis loop at higher partial pressures, characteristic of mesoporous materials, and this remains for the acid-washed counterparts (Figure 5.5d-f). The non-uniform distribution of mesopores observed for the commercial samples treated with NaOH (Figure 5.6a) supported in this case that the zeolite crystal was irregularly dissolved. For the commercial samples treated with CTAB/NaOH, the BJH analysis (Figure 5.6b) clearly revealed defined mesopores of 2-3 nm in size, thus verifying the small mesopores seen by TEM. As a technical point, the size of the mesopores fall within the smaller range typically found for mesopores obtained by the use of CTAB as surfactant (3-10 nm), as indicated in Section 3.2. The voids observed by TEM of the TBAOH/NaOH treated commercial samples appear to be larger than the ones generated by the surfactant-aided method. This is confirmed by the larger mesopores of 2-10 nm in size evidenced in the BJH plot (Figure 5.6c). These mesopores are still small enough to be accommodated within the ZSM-22 particles. With respect to the in house prepared ZSM-22 zeolites, the same shape of the parent *m*-ZSM-22 isotherm holds for the treated samples (Figure 5.5g-i and j-l), with absence of hysteresis loop. Together with the absence of defined mesopores in the BJH pore size distribution (Figure 5.6d-f), this confirms the microscopy observations: the *m*-ZSM-22 crystals with size of ~50 nm does not provide enough room for making large pores. Indeed, pores of 10 nm represent 20 % of the total thickness. As anticipated in Section 3.1 the formation of inter-crystalline mesopores by roughening of the crystal surface is favoured in this case.

The numerical results from the nitrogen adsorption experiments are listed in Table A.1 of the Appendix. Contrary to most desilication studies over unidimensional 10-ring zeolites (see Table 3.1 in Section 3), the microporosity of the *c*-ZSM-22 sample was generally unaffected by the desilication treatments, as also indicated by the similar uptake at low partial pressures of the isotherm. Only the *c*-ZSM-*22-tba2* sample shows a ~ 38 % loss in micropore volume, also seen in the reduced uptake (Figure 5.5c). The microporosity of the *m*-ZSM-22 was drastically reduced after the surfactant-assisted and the high temperature TBAOH/NaOH treatment, whereas the rest of the treatments resulted in an increased micropore volume. As the crystallinity was intact, this reduction is most likely caused by extra-framework species re-deposited on the pore entrances (see below). A reduction of the total surface area ($\boldsymbol{S_{BET}}$) is observed for the samples with reduced microporosity. Micropore volume and $\boldsymbol{S_{BET}}$ follow each other quite closely (R^2 = 0.87, 27 data points), as shown in Figure A.2a of the Appendix.

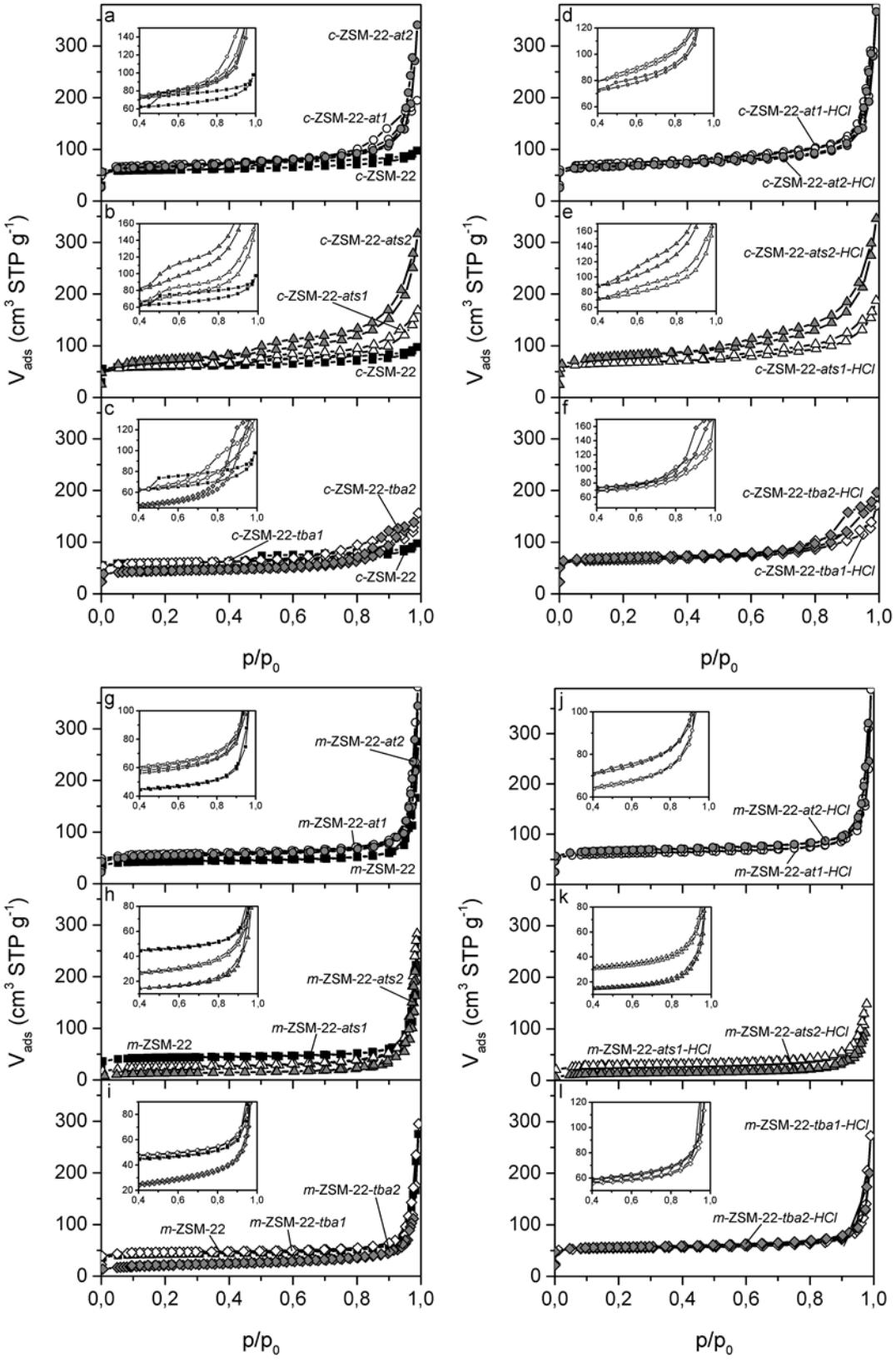

Figure 5.5. Nitrogen adsorption-desorption isotherms for the parent, desilicated and acid washed ZSM-22 samples (**a-c**): commercial desilicated, (**d-f**) commercial acid-washed; (**g-i**): in house desilicated, (**j-l**) in house acid washed). The insets highlight particular regions of each plot.

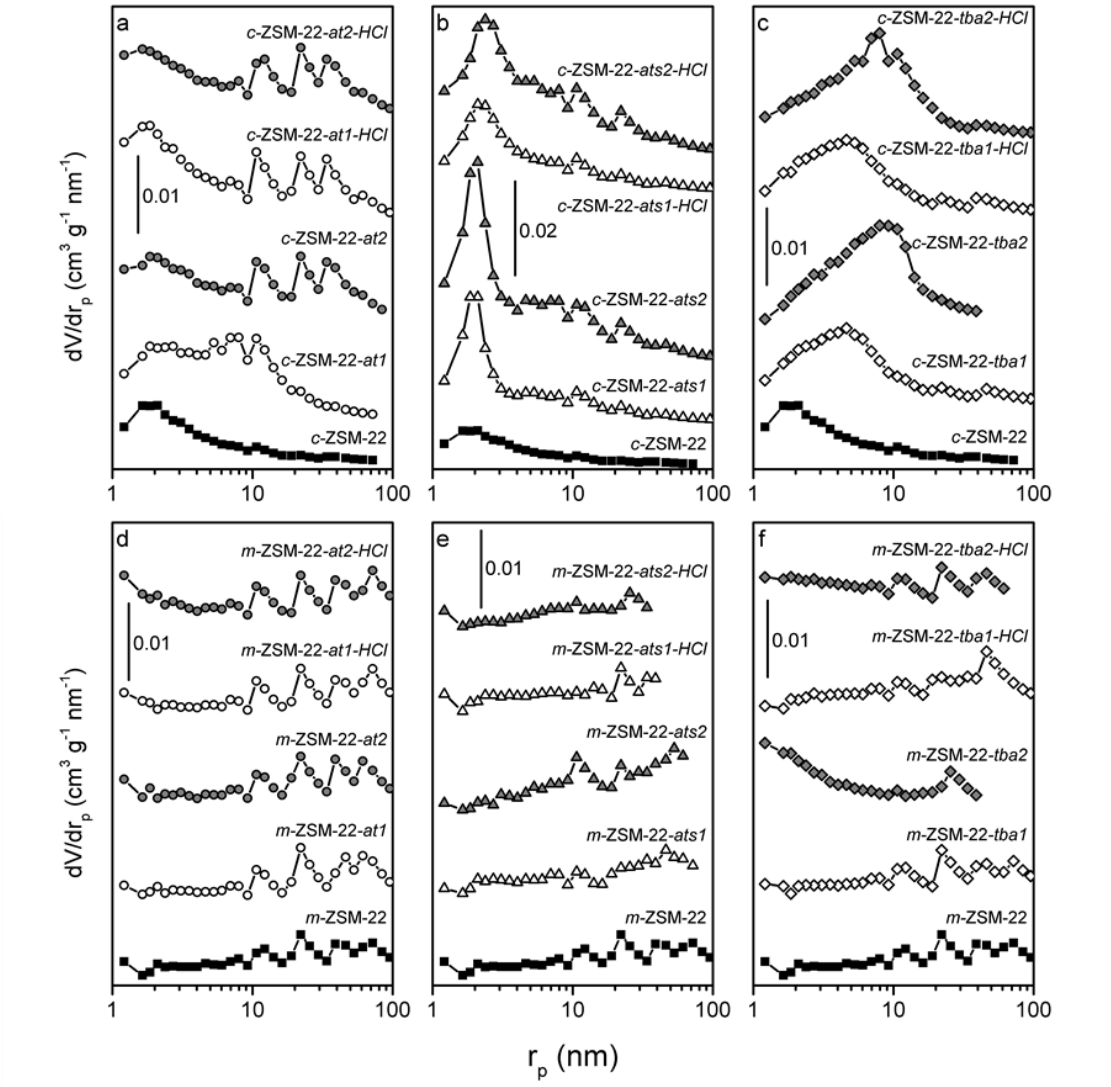

Figure 5.6. Effect of the post-synthetic treatments on the BJH mesopore size distribution (calculated from the adsorption branch of the isotherm) for the commercial (**a-c**) and in house prepared (**d-f**) ZSM-22 samples.

As introduced in Section 3.3, the acid washing was expected to have a marked influence on the porosity of the samples for which micropore volume was reduced upon desilication. Indeed, the microporosity of the samples treated with the high temperature TBAOH/NaOH solution was restored both in commercial and in house prepared materials (Table A.1 of the Appendix), also seen in the increase in N_2 uptake (insets in Figure 5.5e, l). This suggests that the acid treatment successfully removed the re-deposited extra-framework species. However, the micropore volume of the surfactant treated in house prepared samples was not affected by the acid treatment (Table A.1), indicating that the acid leaching was not sufficient to remove the blocking species in this case, most likely because the ellipsoidal unidirectional channels of ZSM-22 prevents these species to diffuse out of the framework.

The external surface area ($\boldsymbol{S_{ext}}$) and external pore volume ($\boldsymbol{V_{ext}}$) are generally correlated, but with substantial spread (linear regression of the entire dataset gives a positive slope, but a quite poor value $R^2 = 0.14$ in Figure A.2b of the Appendix). As a general observation, $\boldsymbol{S_{ext}}$ and $\boldsymbol{V_{ext}}$ were intact or substantially increased for the samples after the various treatments. Particularly, the high temperature TBAOH/NaOH treatment over the *m*-ZSM-22 sample resulted in an increase of the $\boldsymbol{S_{ext}}$, whereas the $\boldsymbol{V_{ext}}$ was reduced, suggesting a larger dissolution of the outer crystal surface. The presence of extra-framework species, apart from blocking the micropores, might inhibit the creation of mesopores in this case. The actual mesoporosity seen by TEM and BJH analysis for the commercial treated zeolites should also be reflected as increased $\boldsymbol{S_{ext}}$ or $\boldsymbol{V_{ext}}$. However, $\boldsymbol{S_{ext}}$ and $\boldsymbol{V_{ext}}$ of the cited samples do not stand out from the rest of samples, suggesting a minor influence of the actual mesoporosity in the external properties. Only the sample treated with the severe surfactant-assisted method (*c*-ZSM-22-*ats2*) showed a marked increase in $\boldsymbol{S_{ext}}$ as a consequence of the created mesopores.

As seen in Table A.1 of the Appendix and from the similar shapes of the nitrogen isotherms, the acid washing affected the $\boldsymbol{S_{ext}}$ and $\boldsymbol{V_{ext}}$ of the desilicated samples to a lesser extent. Noteworthy, the acid washing of the commercial sample treated with low NaOH concentration (*c*-ZSM-22-*at1-HCl*) caused a remarkable increase of the $\boldsymbol{V_{ext}}$ compared to the rest of acid washed samples. For the in house prepared series, the main finding was a significant reduction of the $\boldsymbol{V_{ext}}$ after the acid washing of the surfactant treated samples. Furthermore, the acid washing of the fresh ZSM-22 commercial sample (*c*-ZSM-22-*HCl*) did not have any remarkable influence on the textural properties (Table A.1).

5.1.3. Composition – porosity – acidity interdependence

During the post-synthetic treatments several parameters are simultaneously varied. As indicated in Chapter 3, desilication not only causes the dissolution of the crystal upon Si removal, but also a reorganization of the Al species in the framework. Therefore, the observations herein cannot be understood without assuming a combined effect of the composition (Si/Al), porosity and acidity modifications during the process.

The discrepancies observed between the extent of dissolution (or yield) and the resulting decrease of the Si/Al ratio suggest that apart from Si, Al is extracted upon desilication. This Al can be either redistributed as EFAl species, or extracted from the crystal, or both [13], as

discussed along Section 3. Indeed, Figure 5.4b and c shows that the acid treatment returned the Si/Al ratio of the desilicated samples to the original value of ~49 for the commercial zeolites and ~38 for the in house prepared materials. These results strongly support the idea of the extraction of framework Al and redeposition as EFAl species upon desilication. This EFAl species are then removed with the acid leaching, causing the rise of the Si/Al ratio. As an exception, the Si/Al ratio of the *m*-ZSM-22-*ats2* sample did not vary after the acid treatment, suggesting that either no EFAl species were generated, or that the acid was not capable of washing them out.

As seen from Figure 5.3, the band associated with the BAS at 3600 cm^{-1} is slightly reduced, whereas the isolated silanol band at 3745 cm^{-1} is significantly increased after the desilication treatments over the commercial zeolite. These effects were more pronounced when the surfactant-assisted method was employed (*c*-ZSM-22-*ats1*). The results indicate that the concentration of Brønsted sites do not substantially change upon desilication, in contrast with the general findings reported for one-dimensional zeolites (see Table 3.1), but in agreement with studies of desilicated MFI zeolites [143]. However, the Si/Al ratio decreased upon desilication (Figure 5.4). Then, desilicated samples must give higher acid site concentration if Al remained the same. This again indicates the existence of EFAl species in the desilicated materials. The larger concentration of external silanol groups is readily associated with the increment of the exposed external surface [14, 106, 124, 150, 153, 160], where more silanol groups can be located. Conversely, less mesopore-generated surface can be linked to a lower contribution of external silanol groups. Focusing on the desilicated in house prepared zeolites, a general reduction of the intensity of the 3600 cm^{-1} band is evidenced, indicating that the desilication process also removed Al from framework Si(OH)Al positions. Together with the microscopy, the results suggest that most of the Al is extracted from external acidic positions, reducing the protecting effect on neighboring Si atoms and thus promoting the desilication in external surface areas. Noteworthy, the surfactant treatment resulted in a narrower and more intense band at 3745 cm^{-1}, as a result of larger contribution of silanols located at the created external surface on the more dissolved crystal boundaries of this sample.

Figure 5.3 shows that the distribution of surface sites (BAS, SiOH) of the desilicated samples was barely affected by the acid washing, which indicates that removal of the redeposited EFAl species occur without a marked alteration of the strong Brønsted acidity. The band associated with the isolated silanol groups at 3745 cm^{-1} increased significantly after the acid washing of the commercial alkaline treated sample (*c*-ZSM-*22-at1-HCl*) in Figure 5.3a,

suggesting that the acid washing contributes to clean up not only the strong acid sites, but also to some extent the silanol defects. By using CO as a probe molecule, it was shown that the acid strength of the BAS is practically unaltered by the post-synthetic treatments.

For a detailed study of the simultaneous variation of the zeolite properties upon desilication, a correlation between the amount of acid sites, as calculated from pyridine adsorption measurements (equations **6** and **7** in Section 4.3), and the Al concentration is established. Table A.2 of the Appendix presents the BAS, LAS and BAS+LAS concentration, together with the total amount of Al as calculated from elemental analysis. Pyridine adsorption experiments also provide information of the accessibility to the acid sites. Figure 5.7a shows that the Brønsted acid site band at 3600 cm^{-1} of the parent *m*-ZSM-22 zeolite after pyridine dosing is not completely eroded, indicating that BAS are not fully accessible to pyridine, in accordance with the inaccessible microporosity. Clearly, the access to the BAS was drastically hampered for the *m*-ZSM-22-*ats1* sample Figure 5.7d and this is due to the micropore blockage already seen for this sample. Also, a small fraction of BAS does not seem to be accessible to pyridine for *m*-ZSM-22-*at1* and *m*-ZSM-22-*tba1* samples. The erosion of the BAS band of the *m*-ZSM-22-*at1-HCl* sample (Figure 5.7c) implies that the Brønsted sites of the desilicated counterpart are accessible after the acid washing. On the other hand, BAS were still inaccessible after the acid washing of the *m*-ZSM-22-*ats1* sample (Figure 5.7e), in line with the reduced micropore volume observed for this sample. The same analysis demonstrated the absence of accessibility limitations for the commercial samples, demonstrating that pyridine can reach acidic sites in the micropores.

The data from Table A.2 is graphically represented in Figure 5.8a. The dotted line represents the situation where all the Al atoms form acidic sites. The deviation of the parent *c*-ZSM-22 zeolite from the dotted line together with the low contribution of Lewis acidity seen in Figure 5.8b (ratio BAS:LAS of 8:1 as seen in Table A.2), suggests that non-acidic Al species are already present in the starting material. The *m*-ZSM-22 parent material deviates more from the reference line. However, together with the presence of Al in non-acidic positions, the limited access to the BAS also contributes to the deviation in this case.

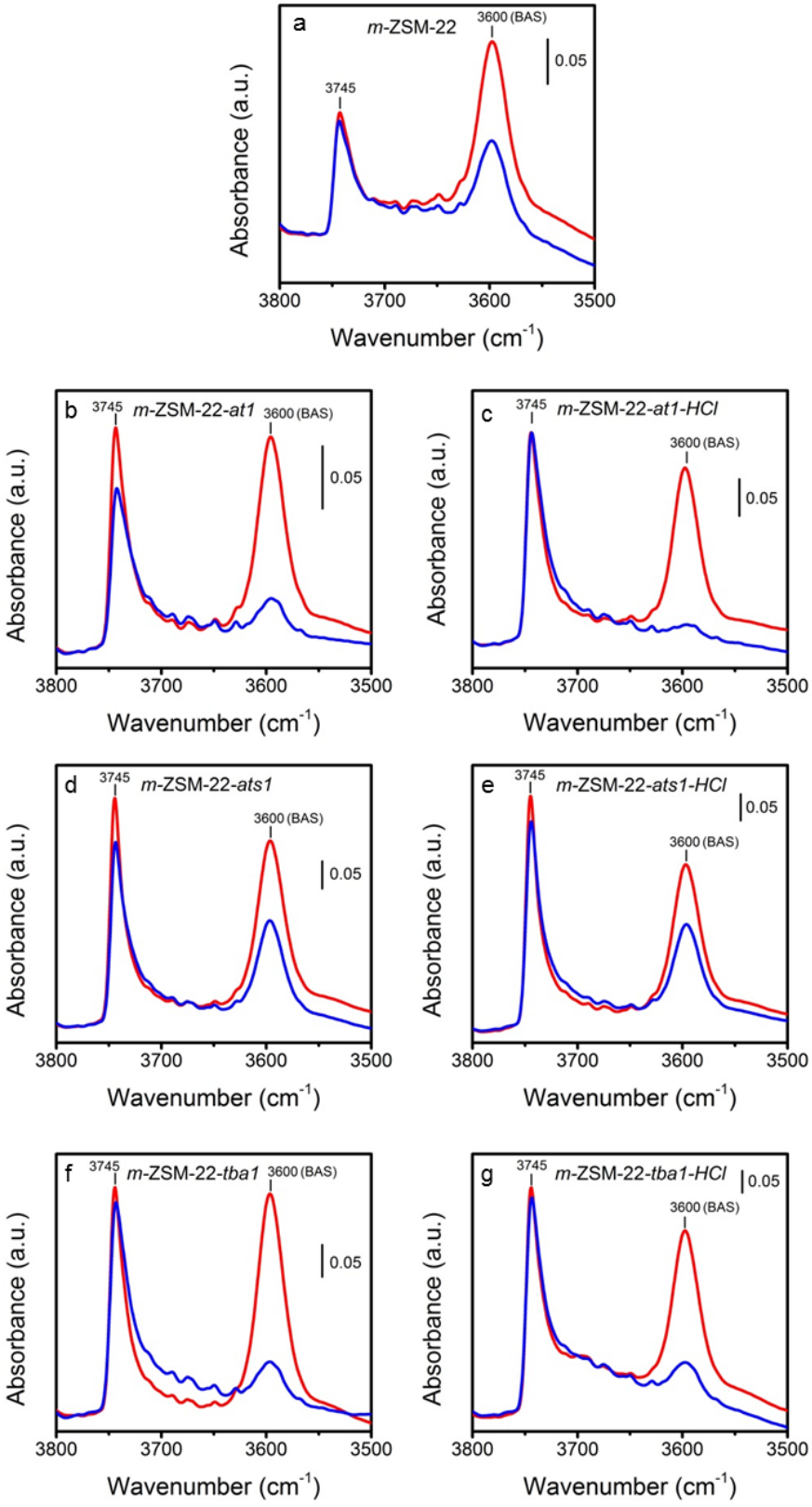

Figure 5.7. FTIR spectra of the parent (**a**), desilicated (**b**, **d** and **f**) and acid washed (**c**, **e** and **g**) in house prepared ZSM-22 zeolites in the hydroxyl stretching region activated at 450 ^{o}C (red line) and after pyridine adsorption (blue line).

Two different features are readily observed for the treated samples. On one hand, the concentration of acid sites is generally lower than the total Al concentration for the desilicated samples (solid points in Figure 5.8a), but higher of that of the starting materials. The *m*-ZSM-22-*ats1* sample (red point) shows a marked low contribution of acid sites, as a result of the hindered access of pyridine to the acidic sites. Figure 5.8b (and Table A.2) shows that desilication lead to approximately a fourfold increase of LAS concentration relative to the corresponding parent material, with the exception of two samples: for *m*-ZSM-22-*tba1* the contribution of LAS was doubled and no remarkable increase was observed for the for *m*-ZSM-22-*ats1* sample. As aforementioned, LAS are associated with EFAl species. The rather low contribution of LAS for both surfactant- and acid-treated samples suggests that other extra-framework species than Al^{3+} (Lewis sites) cause the hindrance effect. On the other hand, the acid washed samples follow closely the dotted line (open symbols in Figure 5.8a), indicating a very similar concentration of acidic sites and total Al. The *m*-ZSM-22-*ats1-HCl* sample clearly deviates from this behavior. However, the general trend is that the acidity is recovered after acid washing. At the same time, the Lewis acidity is reduced with respect to the desilicated analogues (open symbols in Figure 5.8b), supporting the notion of the removal of EFAl species by the acid leaching and linking EFAl species to LAS.

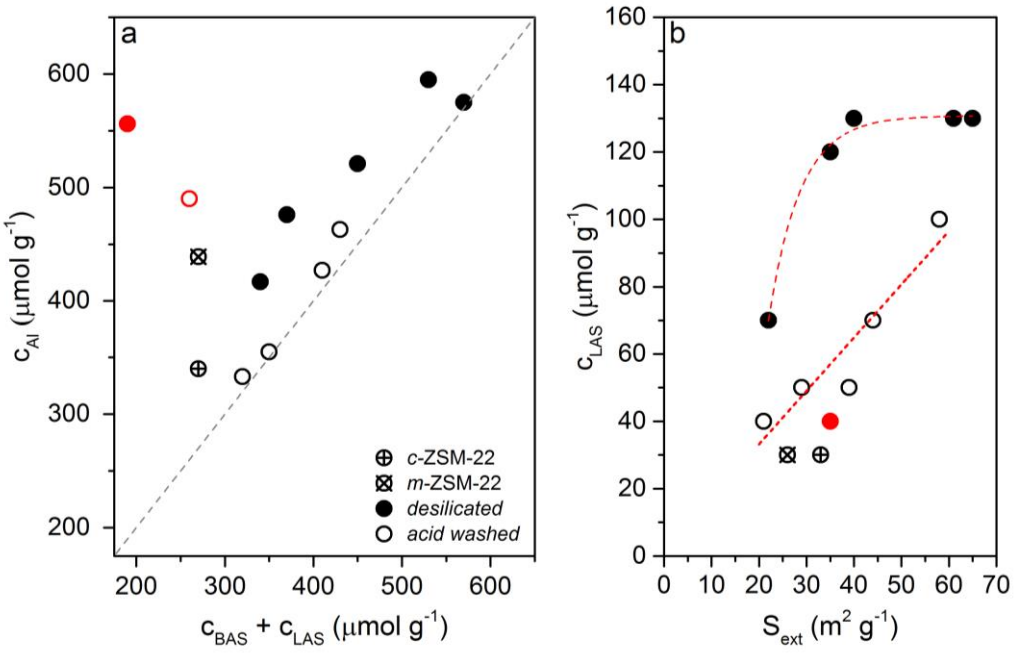

Figure 5.8. (**a**) Correlation between total Al concentration and concentration of acidic sites (BAS + LAS) and (**b**) interdependence between Lewis acidity and external surface area for the parent and selected treated zeolites.

It is generally accepted that the LAS associated with EFAl species are redeposited on the external zeolite surface after desilication [14, 106, 127]. In the present study, Lewis species can be assumed to be redeposited on the external surface of the in house prepared crystals or on the mesopore surface created for the commercial samples, before being washed out by the acid. As seen from Figure 5.8b, the amount of LAS of the desilicated samples reached a level where any further increment in S_{ext} does not imply a further gain in Lewis sites. This suggests that the formation of LAS is limited by another parameter, such as the initial number Al species in non-framework positions.

The origin of the EFAl species generated and redistributed upon desilication is discussed now. As mentioned, BAS concentration should increase since Si/Al decreases upon desilication. However, the process over the commercial sample occurs without a pronounced alteration of the Brønsted acidity, which suggests a transformation of Brønsted to Lewis acid sites. As aforementioned, there is a fraction of non-acidic species already present in the starting material. It is speculated that these species remain after desilication, and that part of them also generate Lewis acid sites. The extra-framework species, including a substantial part of Lewis groups, are eventually removed by acid washing. Regarding the in house prepared series, both contributions of framework Al in Si(OH)Al groups and non-acidic species present in the starting material could contribute to the formation of Lewis species.

5.2. Assessing the catalytic consequences

5.2.1. Improvement of the MTH performance

Among the extensive amount of samples prepared and characterized, the catalytic performance of one sample from each post-synthetic approach over the two microporous ZSM-22 zeolites is investigated in this Section. These samples showed generally higher surface area, micropore and external volume and enhanced accessibility to the acid sites than the parent zeolites.

The methanol conversion versus time on stream plots at 400 ^{o}C and WHSV of 2 h^{-1} are presented in Figure 5.9a, b for the commercial and in house prepared treated catalysts, respectively. The total methanol conversion capacity, calculated as the total grams of

methanol converted per gram of catalyst, was used to quantitatively study the capacity of the catalysts for converting methanol into hydrocarbon products until complete loss of activity (Figure 5.9c, d). The microporous catalysts (*c*-ZSM-22 and *m*-ZMS-22) showed a lifetime of nearly 3 h until complete deactivation, which is shorter than the maximum lifetime previously reported [79]. The suggested stacking faults and the low micropore volume of the *m*-ZSM-22 catalyst may be the cause of the rapid deactivation since the diffusion of reacting molecules through the pores may be slower causing an easier build-up of coke species.

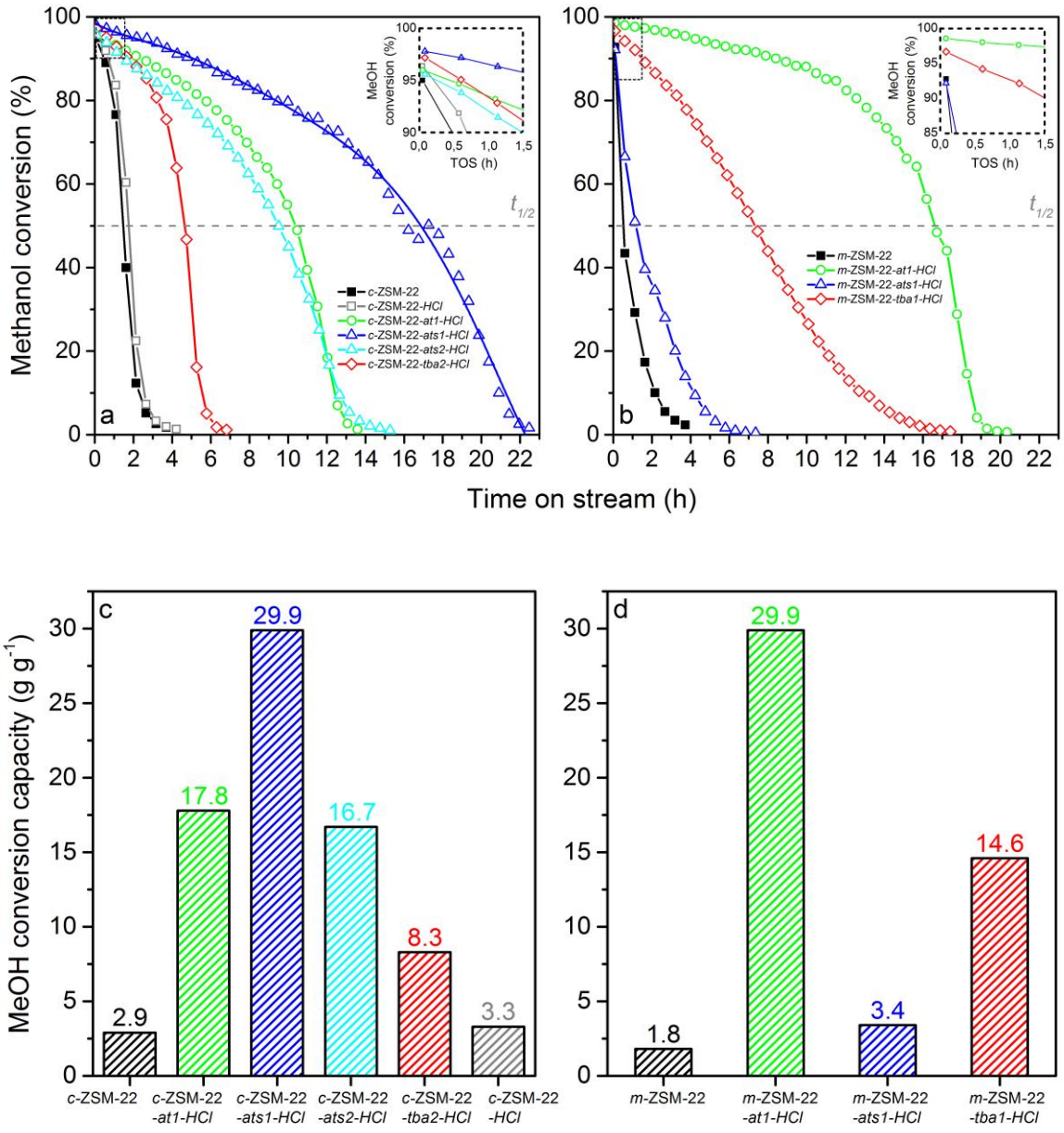

Figure 5.9. Methanol conversion versus time on stream (**top panels**) and total methanol conversion capacity (**bottom panels**) for the parent and treated commercial (**a** and **c**) and in house prepared (**b** and **d**) ZSM-22 catalysts, at WHSV = 2 h^{-1} and T = 400 ^{o}C. $t_{1/2}$ indicates the time at which the conversion decreased by 50%. Insets show the performance during the first 90 minutes on stream.

The hierarchical catalysts show enhanced initial activity and longer lifetime with respect to the microporous H-ZSM-22 catalysts, also reflected in analogous increased conversion capacities. The surfactant treated catalyst (*c*-ZSM-22-*ats1-HCl*) showed the longest lifetime and exceptional enhancement of the total conversion capacity up to 30 g g^{-1}, which represent a 10-fold increase from the parent *c*-ZSM-22 catalyst. The NaOH treated catalyst (*c*-ZSM-22-*at1-HCl*) displayed a notable increase in lifetime and conversion capacity, analogous to the high concentrated surfactant treated catalyst (*c*-ZSM-22-*ats2-HCl*). The TBAOH treatment (*c*-ZSM-22-*tba2-HCl*) had a modest influence in lifetime and conversion capacity, with an increase up to 8 g g^{-1}, which is roughly a three-fold increase from that of *c*-ZMS-22. The only acid washing (*c*-ZSM-22-*HCl*) had no evident influence on the conversion capacity, that highlights that sequential desilication and acid leaching is necessary to improve the catalytic performance of the microporous catalyst. With respect to the in house prepared series, the best increase of more than 17 times in conversion capacity, up to 30 g g^{-1}, was evidenced for the NaOH treated catalyst (*m*-ZSM-22-*at1-HCl*). An 8-fold increase is achieved for the catalyst treated with TBAOH (*m*-ZSM-22-*tba1-HCl*), whereas the surfactant treated catalyst (*m*-ZSM-22-*ats1-HCl*) showed a minor variation. The trends in increased performance are somehow opposite for the two parent H-ZSM-22 catalysts, suggesting that the influence of the starting material on the change in the catalyst properties is also reflected in the catalytic behaviour.

As mentioned in Section 2.5, the potential of ZSM-22 as MTH catalyst resides in their ability to produce environmental friendly gasoline product precursors. Apart from prolonging the lifetime, one of the main goals of this work was to maintain the H-ZSM-22 yield towards aromatic-free C_{5+} alkenes [25, 77, 79] after the post-synthetic treatments. This involves that the micropore topology should not be altered upon the treatments. Previous MTH studies conducted over a range of residence times, concluded that the ZSM-22 shape selectivity was independent of the degree of coking and may be described solely as function of conversion [78]. Accordingly, differences in product distribution for the catalysts will be examined over the full range of conversion.

Figure 5.10 shows that the product yield is very similar for all the catalysts, showing the highest initial contribution of C_{5+} olefins (all > 42 %). The main by-products were C_3 and C_4 alkenes and very low amount (< 5 %) of C_2 (mainly ethene) was obtained. The C_{5+} hydrocarbon yield increased up to the maximum at around 90 % conversion, corresponding to selectivities between 45 to 65 %, while C_3 and C_4 yield decreased for all the catalysts with decreasing conversion. Clearly, the two microporous catalysts showed the lower C_{5+} yield

(black stars), whereas the hierarchical materials yielded the highest C_{5+} fraction. The results correlate with the increased trends seen in lifetime for these catalysts. A maximum C_{5+} yield of 58 and 55 % were observed for the *c*-ZSM-22-*ats1-HCl* and *m*-ZSM-22-*at1-HCl* catalysts, respectively, which showed the longest lifetime. Notably, the highest C_{5+} yield (58 %) improved the one previously reported for one-dimensional medium pore size zeolites under the same conditions [41, 78] by ~ 5 % percentage points.

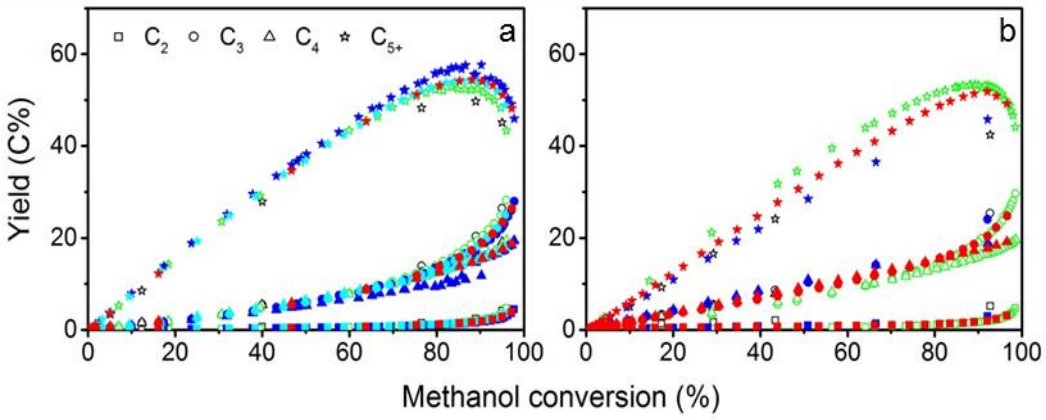

Figure 5.10. Product yield as a function of methanol conversion for the parent and treated commercial (**a**) and in house prepared (**b**) H-ZSM-22 catalysts, at WHSV = 2 h^{-1} and T = 400 ^{o}C. ***c-*** and ***m*-ZSM-22-*at1-HCl*** are shown in green, ***c-*** and ***m*-ZSM-22-*ats1-HCl*** in blue and ***c*-ZSM-*22-ats2-HCl*** in light blue, ***c*-ZSM-22-*tba2-HCl*** and ***m*-ZSM-22-*HCl*** in red. Parent catalysts are shown in black.

The C_{5+} fraction is examined more rigorously in Figure 5.11. The C_5 products are the most abundant between 90-100% conversions, followed by C_{6+} alkenes. With increasing deactivation, there is a marked increase of the C_{6+} products at the expense of the C_5 fraction. As expected, the selectivity towards aromatic hydrocarbons was inferior to 5 % at all conversions for all the catalysts. The results suggest that the cracking activity of long alkenes is reduced with deactivation.

The similar product distribution of the microporous and hierarchical catalysts indicates that the product shape selectivity of the H-ZSM-22 catalysts in the MTH reaction is governed by the micropore system inherent of the TON topology, regardless of the introduction of mesopores, in agreement with Dyballa *et al.* [147]. Furthermore, we can assume that reactions on acid sites at the external surface are not relevant, since they would not be affected by steric restrictions and would result in different product distribution. Overall, the hierarchical H-

ZSM-22 catalysts resulted in a remarkable increase of the lifetime while maintaining the desired selectivity towards aromatic-free C_{5+} alkene fraction, thus reaching the primarily goal of the present work.

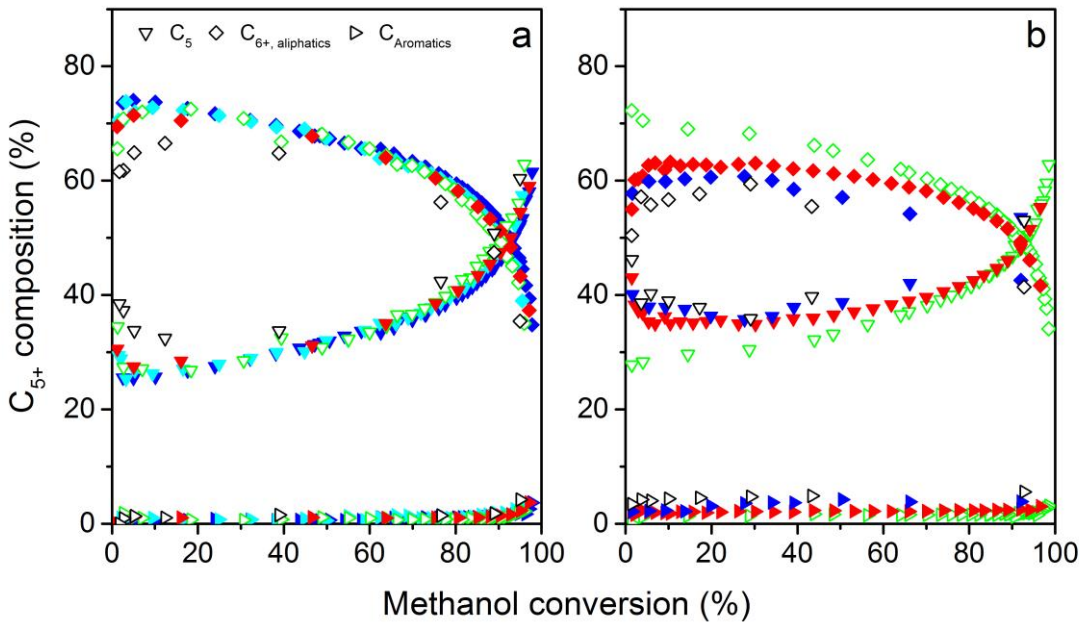

Figure 5.11. Composition of the C_{5+} fraction as a function of methanol conversion for the parent and treated commercial (**a**) and in house prepared (**b**) H-ZSM-22 catalysts, at WHSV = 2 h^{-1} and T = 400 ^{o}C. Same colour codes as in Figure 5.10 are used.

Mechanistic information can be extracted from the analysis of the C_3/C_2 and ethene/2-methyl-2-butene (2M2B) ratios, shown in Figure 5.12, together with the shape of the deactivation curves. In Section 2.3 it was mentioned that the ratio between ethene and 2M2B can be used to describe the relative propagation of the alkene or aromatic cycle in MTH [80], assuming that ethene originates mainly from aromatics and 2M2B (and propene) are to a large extent formed from the alkene methylation/cracking reactions from the olefin MTH cycle. It should be recalled that the alkene-based cycle dominates over the aromatic cycle in the TON topology [25, 77]. Therefore, low ethene/2M2B ratios and high C_3/C_2 ratios are expected.

As seen from Figure 5.12, ethene formation is more significant for the catalysts which deactivated rapidly (*c*-ZSM-22, *m*-ZSM-22 and *m*-ZSM-22-*ats1-HCl*), whereas the most stable catalysts (*c*-ZSM-22-*ats1-HCl* and *m*-ZSM-22-*at1-HCl*) show a lower relative production of ethene and a higher contribution of propene and 2M2B products, resulting in greater increase in the C_3/C_2 ratio and sharper drop in the ethene/2M2B ratio.

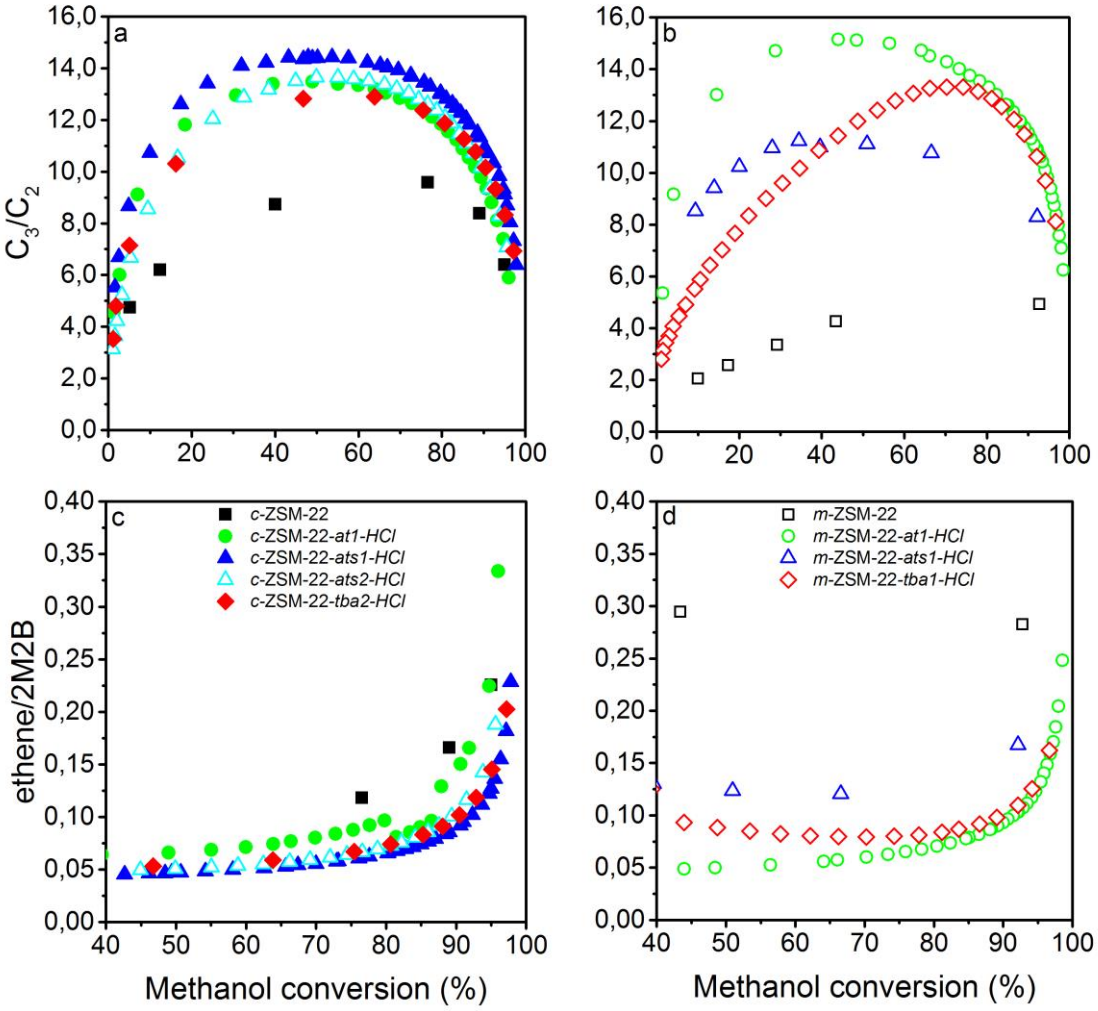

Figure 5.12. C_3/C_2 (**top panels**) and ethene/2-methyl-2-butene (**bottom panels**) yield ratio as a function of methanol conversion over the parent and treated commercial (**a** and **c**) and in house prepared (**b** and **d**) H-ZSM-22 catalysts, at WHSV = 2 h^{-1} and T = 400 ^{o}C.

With this information it can be hypothesized a different degree of progression of alkene methylation/cracking reactions over the H-ZSM-22 catalyst. The more stable catalysts allow a longer operation of the olefin cycle, leading to propene and higher alkenes production for longer times. With increasing deactivation, the propagation of the alkene cycle is not increased anymore and a progressive drop in activity is observed until complete deactivation. The higher formation of ethene is associated with a higher participation of the aromatic cycle already from short reaction times (*m*-ZSM-22 and *m*-ZSM-*22-ats1-HCl*) or after a short initial or induction period of olefin cycle progression (*m*-ZSM-22-*tba1-HCl*), causing faster coke formation. Together with the lower C_{5+} contribution and the higher C_4-hydrogen transfer index (HTI is defined as the combined yields of isobutene and *n*-butane divided by the total

yield of C_4 alkanes and alkenes and constitutes a measure of the hydrogen transfer activity towards more cyclization and aromatization reactions), the results suggest that product molecules cannot easily diffuse out of the unidirectional microporous catalyst topology in these cases, and will be involved in aromatization and cyclization reactions leading to deactivation.

For the rest of post-synthetic treated zeolites from Section 5.1, only the total methanol conversion capacity was calculated (Table A.3 of the Appendix). Even though some of them show higher methanol conversion capacity than the microporous ZSM-22 catalysts, their MTH performance was not as promising as for the hierarchical catalysts investigated.

5.2.2. Correlation with catalyst features

The post-synthetic modifications affected the MTH activity and stability in an interdependent manner for the H-ZSM-22 tested catalysts. All the commercial catalysts had very similar Si/Al ratios of 47-50, and all the in house prepared catalysts showed Si/Al ratios of 34-39. All the catalysts showed also similar acid strength. This implies that that the variations seen in catalytic conversion are too large to be caused by a minor modification of the composition or acid strength for each series.

For the *c*-ZSM-22 with 200 nm crystals, the most beneficial treatment was the combined alkaline and surfactant and acid washing, which leads to 2 nm mesopores, whereas for thinner 50 nm particles of *m*-ZSM-22, the NaOH treatment and acid leaching, which caused the highest increase in external surface and microporous volume, gave the greatest catalytic performance. The very different effects depending on the individual treatments highlight again the importance of the physico-chemical properties of the starting material. As introduced in Section 3.4, porosity and acidic properties cannot be discussed independently since acidity is useless if not accessible and porosity, similarly, will not be fully effective if access to reactive centers is not provided.

Concentrating first on the textural properties, Figure 5.13a shows that both *c*-ZSM-22 and *m*-ZSM-22 microporous catalysts displayed the lowest external surface area. For the commercial hierarchical catalysts (open points), a rather linear correlation of the total conversion capacity with $\boldsymbol{S_{ext}}$ is observed, indicating that the increased catalytic performance is associated with the created intra-crystalline mesoporosity in this case. Surprisingly, the sample with the highest

methanol conversion capacity (*c*-ZSM-*22-ats1-HCl*) clearly deviates from the trend, showing a very low contribution of the mesopore surface in the total conversion of methanol. This indicates that additional factors play a decisive role in the catalytic performance. The in house prepared hierarchical catalysts (closed points) show weak correlation between the total methanol conversion capacity and $\boldsymbol{S_{ext}}$. However, the correlation with $\boldsymbol{S_{micro}}$, shown (Figure 5.13b), indicates that, in this case, the improvement in conversion capacity can be explained by an increased microporosity, where the active sites are available for the reacting molecules. The low conversion capacity of the *m*-ZSM-*22-ats1-HCl* catalyst was expected owing to the severe micropore blocking.

Moving now to acidity modifications, Figure 5.13c and d shows the total methanol conversion capacity as a function of the amount of Brønsted and Lewis acid sites. As aforementioned, these sites were fully accessible to pyridine, except for the *m*-ZSM-22 and *m*-ZSM-*22-ats1-HCl* samples, which showed blocked access to the Brønsted sites. Roughly a linear correlation is found between the amount of BAS and the methanol conversion capacity for all the catalyst, except for *c*-ZSM-*22-ats1-HCl* (top open point), implying that the increased catalytic performance resulted from increased population of accessible BAS. The concentration of Lewis acid sites is systematically higher for the commercial treated catalysts than for the in house prepared treated samples (Figure 5.13d). The plots are separated in three regions, corresponding to the catalysts with high, moderate or low methanol conversion capacity. Among the catalysts showing the best catalytic performance, the commercial *c*-ZSM-22-*ats1-HCl* sample shows a marked contribution of LAS, whereas the amount of BAS was essentially unchanged. To the contrary, the BAS of the in house prepared *m*-ZSM-22-*at1-HCl* catalyst is increased but there is a minor contribution of LAS. For the catalysts in the second region, the Brønsted acidity is increased for the commercial *c*-ZSM-22-*ats2-HCl* sample, accompanied by a marked contribution of LAS, whereas only the BAS of the in house prepared treated catalyst (*c*-ZSM-22-*tba1-HCl*) is significantly increased. The commercial catalyst with lower conversion capacity (*c*-ZSM-22-*tba2-HCl*) showed combined contribution of Brønsted and Lewis acidity, but lower than the samples with higher conversion capacity.

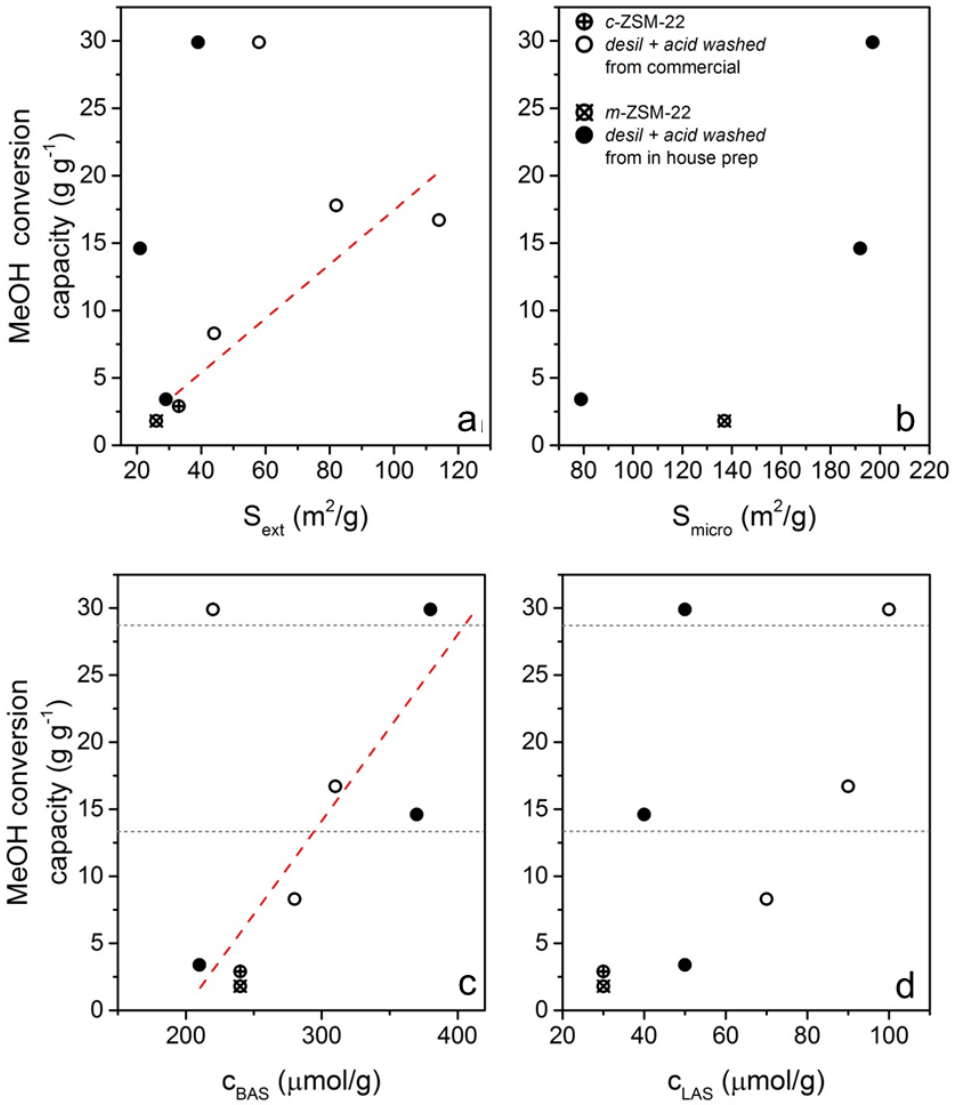

Figure 5.13. Correlation of total methanol conversion capacity with the (**a**) external surface area (S_{ext}), (**b**) microporous surface area (S_{micro}), (**c**) amount of accessible Brønsted acid sites (c_{BAS}) and (**d**) Lewis acid sites (c_{LAS}), for the studied catalysts.

With these results it is proposed that the accessible BAS of the microporous *c*-ZSM-22 catalyst allow the initiation of the olefin cycle. A higher diffusion of the higher alkenes caused by increased porous properties and accessibility to BAS favours alkene methylation/cracking reactions, resulting in increased MTH catalytic performance. Furthermore, it appears that the larger contribution of LAS favours the olefin cycle to operate longer and thus increase the catalytic performance. On the other hand, the restricted micropores of the *m*-ZSM-22 resulted in limited activity in the MTH conversion, but the increased micropore access and the resulting accessible BAS allow the propagation of the olefin cycle for the in house prepared catalysts.

Even though the effect of LAS on the zeolite catalytic activity is not completely understood, some contributions proposed a synergistic effect between Lewis and nearby Brønsted acid sites to enhance the activity of acid zeolite catalysed reactions [17, 18]. Increased MTH activity has also been reported for desilicated MFI catalysts samples with high Lewis acidity [153]. It has been proposed that LAS may promote hydrogen transfer reactions leading to the formation of formaldehyde from methanol, which further reacts with alkenes at BAS to produce coke over ZSM-5 catalyst [14, 180]. Conversely, it has been reported that the incorporation of Ca into ZSM-5 leads to $CaOCaOH^+$ species with Lewis character that weaken the acid strength and cause the reduction of hydride transfer reaction rate and consequently the suppression of the aromatic cycle and increased light olefin selectivity [181]. The results presented in this work agree better with the latter observation, since the interaction of a bridging OH group and a Lewis site seems to promote the alkene cracking/methylation reactions possibly because LAS are more prone to accept coking species leaving the Brønsted sites ready for operating the alkene cycle.

The accessibility and internal diffusion was examined by measuring the uptake of toluene at 100 ^oC and 0.1 mbar. These conditions are far from the reaction temperature (400 ^oC), at which the diffusion of toluene will be improved. Therefore, it is difficult to confidently assess the real diffusion effect by this technique. *In-situ* experiments will be needed for a successful assessment of the diffusion properties at relevant reaction conditions. Apart from the two parent catalysts, two representative samples were measured: *c*-ZSM-22-*ats2-HCl* and *c*-ZMS-22-*tba2-HCl* for the commercial series and *m*-ZSM-22-*at1-HCl* and *m*-ZSM-22-*tba1-HCl* for the in house prepared set. In principle, toluene molecule (6.1 Å) would have difficulties in diffusing through the micropores of the H-ZSM-22 zeolite framework (see Section 1.3). This anticipates that the diffusion of toluene might be limited for the samples with low micropore volume. Figure 5.14 shows a higher adsorption capacity for all the hierarchical catalysts as compared with the commercial microporous material. Besides, the adsorption of toluene was slightly faster for the hierarchical samples at shorter times, since the same uptake is reached at shorter times. These results indicate increased diffusivity in the hierarchical catalyst crystals. Since the microporosity of the catalysts was practically unaffected (Table A.1), the intrinsic diffusivity throughout the catalyst micropores is considered to be very similar. Therefore, the higher adsorption capacity may be attributed to an improved accessibility and/or shorter diffusion path length for the mesoporous crystals. The toluene uptake of the in house prepared hierarchical catalysts (Figure 5.14b) correlates with the increased total conversion capacity,

suggesting that the created microporosity is fully accessible. The diffusivity of the in house prepared treated catalyst was barely increased by the post-synthetic treatments at shorter times, but it was increased at longer times.

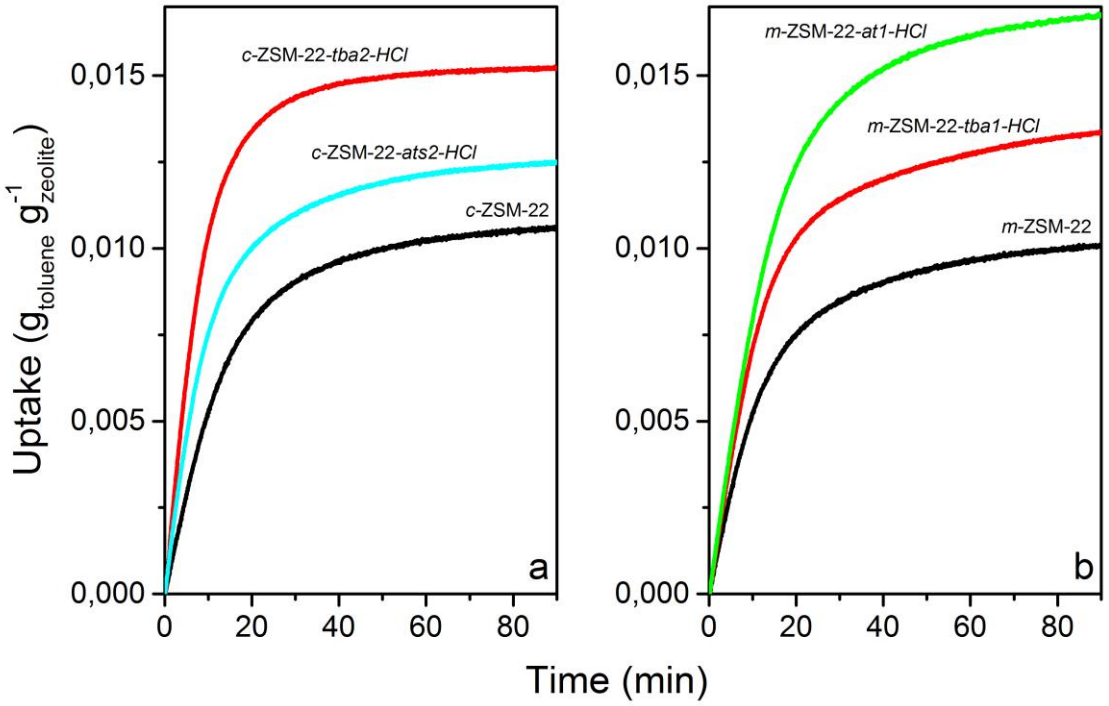

Figure 5.14. Normalized toluene uptake curves of the selected parent and hierarchical commercial (**a**) and in house prepared (**b**) ZSM-22 catalysts.

5.2.3. Structure-deactivation investigations

As stated above, the main issue of H-ZSM-22 as MTH catalyst is the low lifetime. Therefore, understanding of the causes of the rapid deactivation and providing insight into the time-on-stream behaviour of H-ZSM-22 catalysts were of particular interest in the present work. In this regard, the catalytic behaviour of H-ZSM-22 under three different conditions and the crystallographic changes during testing were studied by *operando* time- and space-resolved HXRD. The performance of the commercial *c*-ZSM-22 catalyst was compared before and after surfactant and acid treatment, and with and without propanol co-feed. The surfactant-assisted and acid washing method has already been proved to enhance the methanol conversion capacity for *c*-ZSM-22-*ats1-HCl* at 400 ^{o}C and WHSV of 2 h^{-1}. The high critical contact time showed for H-ZSM-22 (Section 2.5) strongly suggest that the conversion capacity can be increased if the autocatalytic reaction is forced to start at the beginning of the

catalyst bed, in other words, if the induction period is reduced leading to a larger active fraction of the bed. This was reached by co-feeding experiments, explained in **Paper IV**. Co-feeding a methanol:propanol ~ 50:1 mixture over H-ZSM-22 at 400 ^{o}C and WHSV of 2 h^{-1} gave 4 times higher methanol conversion capacity compared to feeding methanol alone, as a result of a more effective utilization of the catalyst and/or a reduced tendency for coking reactions [182].

The catalytic setup described in Section 4.4 allowed to simultaneously measure the catalyst activity and unit cell volume variations with TOS. Figure 5.15 shows the MS intensities of the key species (top plots) and ZSM-22 unit cell volume variations (bottom plots) for the three different systems. It can be observed that the increasing of the cell volume ($Å^3$), interpreted as the expansion of the unit cell, at different positions in the catalytic bed and final flattering matched nicely with the catalytic activity gradients, suggesting that the expansion was mainly caused by deposition of deactivating coke species. Red, blue and open symbols in Figure 5.15 represent first, middle and last segments of the catalytic bed, respectively. Noteworthy, thermal expansion experiments performed by a capillary confirmed that the initial expansion (0.5-1 $Å^3$) at very low TOS might correspond to a local temperature increase of about 13 ^{o}C caused by the released heat due to the exothermic nature of the MTH reaction, whereas the total lattice expansion of about 3.5 $Å^3$, which represents a 0.28% increase of the initial free unit cell, is not likely to be caused by an increase in temperature but due to the accumulation of coke species in the catalyst framework.

Figure 5.15a shows that when feeding methanol alone over *c*-ZSM-22, all the positions of the catalytic bed showed basically the same unit cell expansion with TOS until the cell volume remains constant at around 40 min. This indicates that coke formation occurs over all the catalytic bed. The deactivation curve from the MS plot follows the observed expansion, showing a very rapid methanol/DME breakthrough and fast deactivation, suggesting that the conversion of oxygenates to alkenes is very fast so is the transition from methanol to coke. This is schematically depicted in step 1 to 2 in the bottom panel in Figure 5.15a. The accumulation of aromatic of polyaromatic coke species eventually block the access (by the rare ends of the ZSM-22 crystal) to the acid sites leading to a deactivated state (step 3).

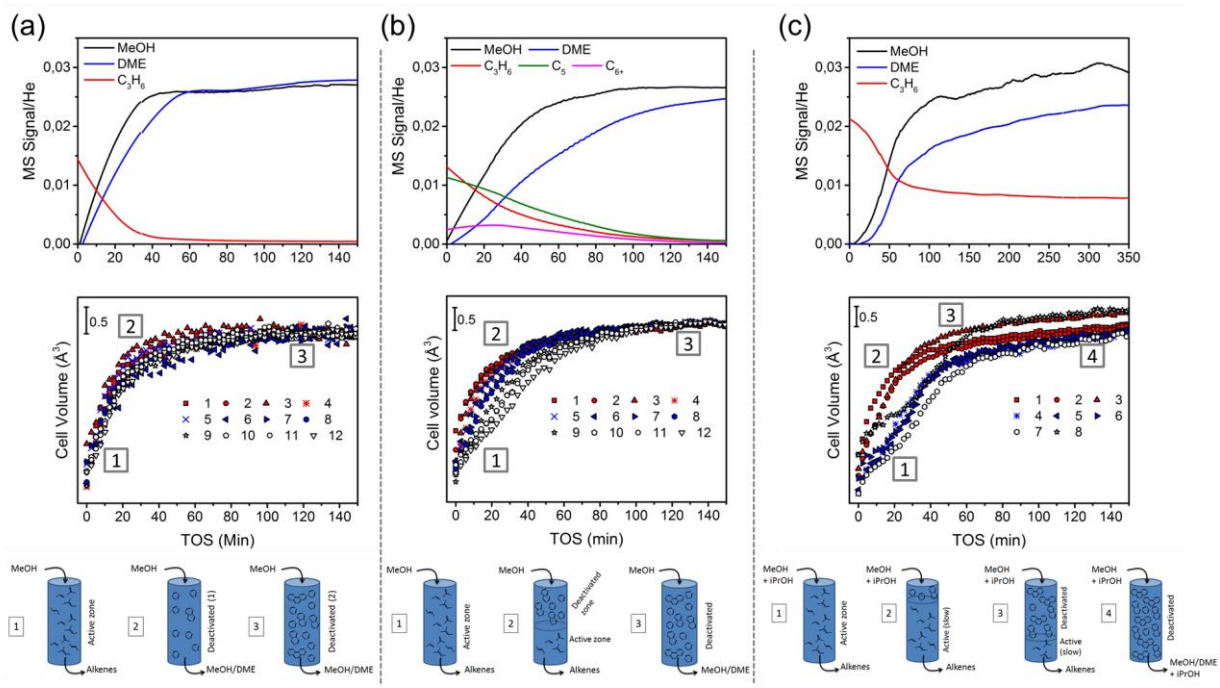

Figure 5.15. MS intensities versus TOS (**top**), unit cell volume versus TOS (**middle**) and schematic representation of the accumulation of deactivating species along the catalyst bed (**bottom**) for the three different systems studied: (**a**) *c*-ZSM-22 fed with methanol, (**b**) *c*-ZSM-22-*ats1-HCl* fed with methanol and (**c**) *c*-ZSM-22 co-fed with methanol and isopropanol. The distance from the reactor inlet increases from 1 (red) to 12/8 (white).

The effect of the post-synthetic modifications on the activity in the MTH process is investigated in Figure 5.15b. The characterization studies of the *c*-ZSM-22-*ats1-HCl* sample showed that the number of accessible acid sites increased after the surfactant-acid treatment, which is supported by the increase from 0.29 to 0.32 mmol/g in acid site density from the propyl-amine TPD experiments. Figure 5.15b shows that the total expansion was very similar also in this case. However, the expansion of the middle and especially the last zones of the catalyst bed were slower than for the first layers. This pattern matched very well the MS deactivation curve. This implies that the long-lived *c*-ZSM-22-*ats1-HCl* catalyst has a different deactivation mechanism with respect to the untreated *c*-ZSM-22. In this case, after a very rapid transition from the full catalytic bed active for methanol conversion into alkenes (step 1 in Figure 5.15b bottom panel), methanol is being converted to coke species in the first zones of the bed, which deactivate rapidly, whereas the rest of the bed remains still active for the autocatalytic MTH conversion (step 2). The results indicate that the higher number of acid sites accessible enhanced the reaction rate by allowing the hydrocarbon production to continue despite the first layers of the bed being deactivated, in accordance with the promotion of the olefin cycle proposed above. These results suggest that methanol is the main

source of deactivating coke formation, in agreement with previous studies over H-ZSM-22 [86, 87, 89], while products alone do not contribute significantly to coke formation. Ultimately, both methanol direct conversion into coke and reactions of oxygenates with alkene products produce aromatics that deactivate the remaining areas of the catalytic bed.

The co-feed process (Figure 5.15c) shows remarkable differences with respect to the two previous scenarios. Propanol dehydrated fast initially to form propene in this case. A similar fast expansion of the first segments of the catalytic bed as that for the normal MTH reaction is observed. The same coking rates for all the length of the reactor when methanol was fed alone, as well as in the first segments of the bed in the co-feed case again suggest that methanol is a major source of deactivating coke, regardless the presence of hydrocarbons and water. The similar expansion rate of the first and the very last layers of the bed at short TOS can be explained by the mentioned local temperature increase. A noticeable double curve shape between the first and last section of the catalytic bed is evidenced in the unit cell volume diffractograms, which also matched the MS curve. The data suggest that after a very short initial period when methanol is being converted to alkenes (step 1 in Figure 5.15c bottom panel), it is converted into coke species at the inlet of the reaction bed, while a rapid conversion of methanol also to products let the rest of the catalyst bed active (step 2) with slow unit cell expansion, resulting in longer lifetime. The aromatic production gradually progressed towards the last segments of the bed (step 3) as suggests the same expansion rate with TOS, until the whole bed was deactivated (step 4). The autocatalytic nature of the MTH reaction implies that the products formed in the first few layers of the bed accelerate product formation in subsequent sections. The improved catalytic performance may be explained by methylation of the co-fed alcohol, which induces activation in the very beginning of the catalyst bed, compared to the reaction involving neat methanol [183, 184].

In the three studied cases, coke formation seemed to be unaffected by the co-presence of reaction products over ZSM-22. This finding differs from previous observations over MFI catalyst [90, 185], where the presence of hydrocarbon products was suggested to prevent coke formation from methanol. The lesser expansion of the unit cell towards the end of the catalytic bed when propene is co-feed over the catalyst at 350-400 ^{o}C and WHSV of 2 h^{-1} supports the notion mentioned in Section 2.5, *i.e.*; the critical contact time represents a significant fraction of the total contact time for H-ZSM-22 catalysts [86, 87]. On the other hand, no initial active zone was found when converting methanol over the untreated catalyst.

The technique employed allows to follow the accumulation of only internal coking species but does not allow to track the deactivation by coke deposition on the external surface of the zeolite particles, which might also block the unidirectional ZSM-22 channels. Nevertheless, taking into consideration the deactivation study by Rojo *et al.* [87], coke species formed from methanol are considered to be accumulated in the micropores. In order to clarify the relative contribution of internal or external coking, the ZSM-22 catalytic performance was correlated with the intensity ratio of the IR absorption bands at 3735 and 3745 cm^{-1} (I_{3735}/I_{3745}), corresponding to internal and external silanol groups, respectively [12]. While external silanols can be formed as natural terminations of the zeolite crystal structure, internal silanols represent defects in the bulk zeolite crystal. Previous investigations on a series of H-ZSM-5 [175] revealed that deactivation is governed by internal framework defects, which do not depend on the acid site density. Catalysts with high internal silanol density or low external surface area showed faster deactivation in MTH, since internal silanols may interact with the hydrocarbons resulting in a slower diffusion and faster deactivation. Figure 5.16 shows a weak correlation (R^2 = 0.6, 8 data points) between the I_{3726}/I_{3745} ratio and the total methanol conversion capacity, indicating that framework defects had a minor effect on the catalytic performance of the studied ZSM-22 catalysts. This was expected, since the increasing of S_{ext} of the treated commercial samples was also accompanied by a substantial contribution of defects, and the removal of defects after the treatment of the in house prepared samples occurred with a lesser modification of the external silanols contribution (Section 5.1). The point depicted in red corresponds to the *m*-ZSM-22-*ats1-HCl*, with lower conversion capacity due to the hampered access to the acid sites.

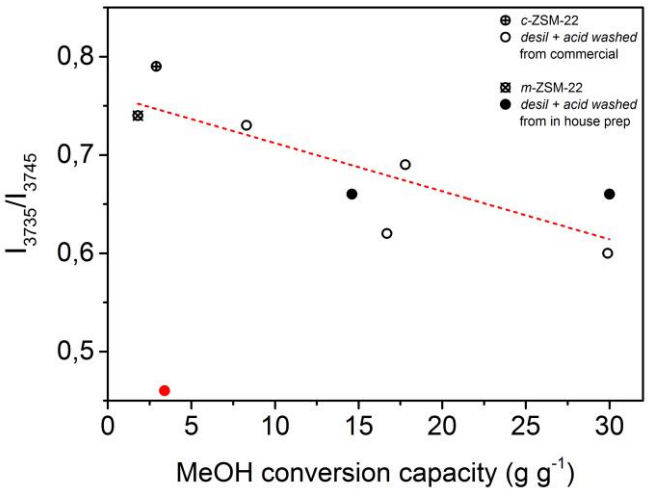

Figure 5.16. Correlation between the total methanol conversion capacity and the IR intensity ratio (I_{3735}/I_{3745}) for the H-ZSM-22 catalysts studied in this work. IR data from activation at 450 ^{o}C have been used.

5.3. Extension to other one-dimensional 10-ring structures

Desilication and sequential acid washing have been demonstrated to improve the MTH performance of one-dimensional H-ZSM-22 catalyst. Similar strategies were also applied to the H-ZSM-23 zeolite, which possess MTT topology with also unidirectional 10-ring channels, but small side pockets and slightly different channel dimensions (see Section 1.3).

The Si/Al ratio of the commercial *c*-ZSM-23 zeolite (24) falls slightly outside the range for an efficient desilication of MFI zeolites [114], which might represent an impediment for efficient mesopore generation. As with the ZSM-22 zeolite, ZSM-23 crystallizes forming needles (Figure 5.17), with the unidirectional channels running in the direction of the needle. Particularly, *c*-ZSM-23 also possess a very low micropore volume, as can be seen in the low adsorbed volume in the nitrogen isotherm (Figure 5.18a). The relatively high external surface area (Table A.4) should be related to the space created between the aggregated particles. This obviously resulted in a very low stability against deactivation in the methanol conversion. Figure 5.19a shows that *c*-ZSM-23 catalyst deactivates completely at 3 hours on stream.

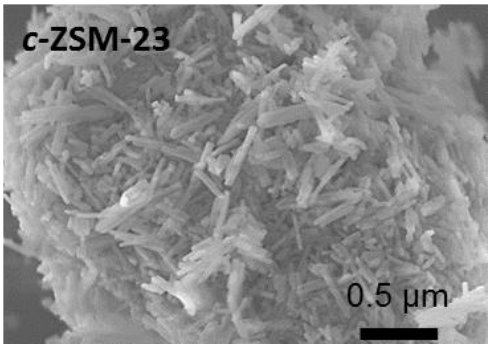

Figure 5.17. SEM micrograph of the parent *c*-ZSM-23 zeolite.

The parent *c*-ZSM-23 sample was selected in order to evaluate the effect of the post-synthetic strategies on a sample with poor catalyst properties. One sample from each post-synthetic treatment is selected as representative: *c*-ZSM-23-*at1-HCl*, *c*-ZSM-23-*ats1-HCl* and *c*-ZSM-23-*HCl*. The numerical values of the different composition, textural and catalytic properties for all the samples are presented in the Table A.4 of the Appendix. Figure A.3 shows that the crystallinity of the samples was generally maintained after the treatments. However, a severe

loss of the crystallinity is evidenced for some of the samples. The XRD peak intensities generally diminish for the samples treated with NaOH (and sequential acid washing). In addition, for the samples *c*-ZSM-23-*ats2* and *c*-ZSM-23-*HCl*, there is a broadening of the peak of reflection at 11.4°, which may reveal some imperfections of the crystals of these samples. Table A.4 shows that the Si/Al ratio is reduced upon alkaline treatment, but it is returned to the initial value after the acid washing. This implies that the EFAl species have been generated and redistributed during desilication are eventually removed upon the acid leaching.

From Figure 5.18a, it can be observed that the nitrogen adsorbed volume at low partial pressures is significantly increased for the selected samples, and this is reflected on an increase in micropore volume and in total surface area (S_{BET}). The external surface area was also increased, as indicated in the increase in the adsorbed volume at high partial pressures. The BJH mesopore size distribution showed in Figure 5.18b indicates no evident appearance of defined mesopores within the crystal after the treatments. As it was with the *m*-ZSM-22 zeolite, the low microporosity and the thinner dimensions of the needles of the parent *c*-ZSM-23 sample (~ 100 nm) are very likely responsible of the lack of intra-crystalline mesoporosity formation upon the treatments. The blocking species were still present after desilication, but they are removed upon the acid washing.

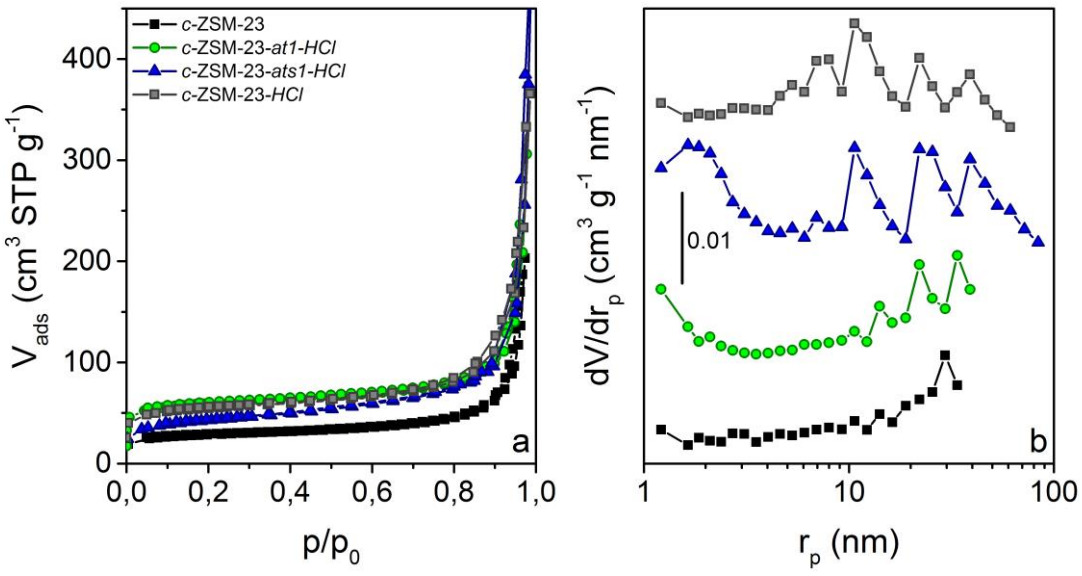

Figure 5.18. Nitrogen adsorption-desorption isotherms (**a**) and BJH mesopore size distribution (calculated from the adsorption branch of the isotherm) (**b**) for the parent and treated selected ZSM-23 samples.

Figure 5.19a presents the conversion versus TOS curves for the parent and treated H-ZSM-23 catalysts. The yield, C_3/C_2 and ethene/2M2B ratios are shown in Figure 5.19b, c and d, respectively. As expected, the enhancement of the microporosity directly causes the improvement of the catalytic performance. The lifetime is consequently increased, as well as the initial activity and the total C_{5+} yield, again demonstrating the benefits of the post-synthetic strategies to obtain improved catalysts for the production of aromatic-free gasoline precursors. The expected product distribution for the unidirectional zeolite catalysts (Section 2.5) is obtained for all the samples. Interestingly, the only acid washed sample resulted in an increasing of the lifetime. All the desilicated H-ZSM-23 show a marked decrease in methanol conversion capacity with respect to the untreated material (Table A.4). On the other hand, the conversion capacity is increased after the acid leaching. The results indicate that, for one-dimensional catalysts with limited microporosity, the acid washing may be sufficient to clean the structure from defects, resulting in more accessible acid sites and open channels. With respect to the product distribution, the *c*-ZSM-23-*ats1-HCl* sample shows the highest C_{5+} yield. As it was observed for the H-ZSM-22 catalysts, Figure 5.19c, d show that ethene is significantly formed relative to higher alkenes for the samples which deactivate faster. The catalysts with longer lifetime show a higher production of propene and 2M2B. The results suggest a longer propagation of the alkene methylation/cracking reactions of the alkene-based MTH cycle also with the MTT treated catalysts.

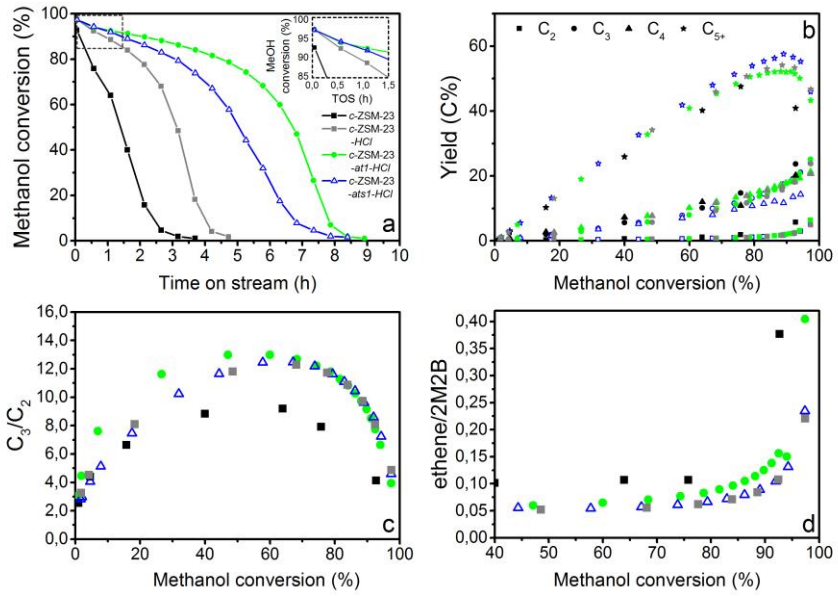

Figure 5.19. (**a**) Methanol conversion versus time on stream. Inset shows the lifetime during the first 90 minutes on stream. Product yield (**b**), C_3/C_2 (**c**) and ethene/2M2B yield ratio (**d**) for the parent and treated selected ZSM-23 samples.

Despite the promising results, the correlation with the catalyst features of the parent and treated H-ZSM-23 was not obvious, owing to the very peculiar properties of the starting ZSM-23 material, and additional advanced characterization was not accomplished.

5.4. Main conclusions

- The crystal morphology of the starting ZSM-22 zeolite is the dominant parameter which influences the mesopore formation.
  - Desilication of the commercial rod-like crystals of 200 nm in with resulted in the creation of intra-crystalline mesopores, whereas the thinner dimensions and low micropore volume of the in house prepared needle-shaped crystals (~50 nm) represent an obstacle for intra-mesopore creation. Instead, the boundaries of the crystals were preferentially affected, resulting in eroded nanoparticles with higher external surface area.
  - Mesopores created from framework defects, however, cannot be dismissed.

- The different desilication approaches resulted in mesopores with different shape and size from the commercial zeolite.
  - The conventional alkaline treatment with NaOH resulted in both roughening of the crystal surface and creation of non-uniform mesopores, whereas when CTAB or TBAOH agent was added, a defined mesopore size distribution is obtained. The surfactant-assisted treatment led to the formation of smaller mesopores of 2 nm in size, while larger pores of about 3-8 nm in size are generated when TBAOH is added to the alkaline solution.
  - The protecting effect of the surfactant over the zeolite structure is only evidenced at low concentrations of base.

- Desilication led to a reduction of the Si/Al ratio. The acid washing returned the values to the original values, indicating that extra-framework alumina species were generated during and redistributed upon desilication.
  - The process occurs without a marked modification of the Brønsted acidity, suggesting a transformation of Brønsted to Lewis acid sites upon desilication.
  - The extra-framework species, including a substantial part of Lewis groups, are eventually removed by the acid treatment
  - Non-acidic Al species already present in the starting commercial zeolite may also contribute to formation of both Lewis and extra-framework species.

- The sequential acid washing recovered the acidity of the desilicated zeolites and generally resulted in increased surface area and micropore and external volume. The exclusive acid washing of the fresh ZSM-22 zeolite did not affect the textural properties.

- A significant enhancement of the H-ZSM-22 MTH catalytic lifetime was obtained after the desilication and acid washing of the zeolites.

  - The methanol conversion capacity was increased at most by a factor of 10 after the surfactant-assisted method followed by acid washing over the commercial material, as a result of a combined effect of mesopore formation, enhanced accessibility to the acid sites and increased transport properties.

  - A 17-fold increase was achieved for the in house prepared catalyst treated with NaOH and sequentially acid washed, due to increased microporosity and enhanced accessibility to the Brønsted sites.

- The high selectivity towards the desired aromatic-free C_{5+} alkene fraction was further optimized after the post-synthetic treatments, thus reaching the goal of obtaining improved catalysts for the process of producing environmental friendly gasoline.

- The presence of Lewis acidity is proposed to have a beneficial effect by allowing a longer operation of the olefin MTH cycle, thus resulting in improved catalytic performance.

- The deposition of deactivating species during the MTH reaction causes the expansion of the unit cell of the H-ZSM-22 catalyst.

- Methanol appears to be the major source of coke and coke formation from products alone is not significant in the TON topology.

- The formation of deactivating species from methanol is independent of the co-presence of products in the TON topology under the conditions employed in this study.

- Isopropanol co-feed improved the methanol conversion capacity of H-ZSM-22 by forcing the autocatalytic reaction to start earlier in the catalyst bed.

- The beneficial effects of the post-synthetic treatments on the MTH performance were extended to unidirectional 10-ring zeolite structure: ZSM-23 with MTT topology. The improvement in methanol conversion capacity is mainly caused by increased microporosity.

6. Suggestions for Further Work

The main goal of improving the lifetime of the catalysts for the production of an aromatic-free product has been reached in this work. However, despite the large body of samples investigated, we do not succeed in arriving at a predictable procedure for mesopore introduction, and general trends are always accompanied by inexplicable deviations. Assessing the causes of variations on the catalytic performance and addressing single-parameter activity/deactivation dependencies was not straightforward, owing to the interdependence between composition, textural properties, morphology and acidity features. Thus, further work could be directed to:

- A better knowledge of the complex transformations involved during the desilication process in order to provide rational tools for a better control of the desilication with, for instance, *in-situ* spectroscopic techniques to study both the desilication physical process and the reaction with a time- (and space-) resolved tool. This constitutes a particular challenge for one-dimensional systems such as ZSM-22 zeolite, which are very prone to pore blocking.

- Validate the results by repeating the synthesis of the zeolites, or employ more starting materials, and the preparation of the post-synthetic catalysts, in order to validate the reproducibility of the characterization methods, treatments and synthesis parameters.

- A systematic analysis of all the numerical values with statistical or numerical methods with the aim to develop a method to screen properties and find descriptor able to describe the catalytic performance in terms of a set of physically meaningful parameters, which ultimately would be used to predict the desired catalytic selectivity.

Furthermore, detailed NMR studies to accurately identify the position of Lewis and Brønsted acid sites in the framework environment would serve to rationalize the contribution of these sites in the propagation of the MTH catalytic cycle.

The use of bulky molecules that cannot enter the medium sized pores of the studied zeolites, such as collidine would be particularly beneficial to distinguish between internal and external acid sites and their implication in the MTH reaction over on-dimensional catalysts.

Isotopic labelling experiments could be performed in order to investigate the intrinsic activity of simpler model reactions, such as cracking of long alkenes (C_{5+}) for the parent and treated catalysts.

Advanced diffusion tools can be used to study the diffusivity of reliable hydrocarbon molecules, such as propene, butenes and C_{5+} alkenes. Uptake experiments with linear and mono/di-branched alkenes and gravimetric gas sorption analysis are of particular interest.

Finally, the strategies carried out in this work can also be extended to other one-dimensional 10-ring topologies. For instance, the influence of side pockets or slight variations in channel dimensions on unidirectional frameworks could be explored by using EUO or MRE structures, respectively.

References

[1] J. Berzelius, Considerations respecting a new power which acts in the formation of organic bodies, Edinburgh New Philos. J., 21 (1836) 223-228.

[2] I. Chorkendorff, J. Niemantsverdriet, Concepts of modern catalysis and kinetics, 2nd ed., Wiley-VCH Verlag GmbH & Co. KGaA, Weinheim, 2003.

[3] I. Fechete, Y. Wang, J.C. Vedrine, The past, present and future of heterogeneous catalysis, Catal. Today, 189 (2012) 2-27.

[4] J.M. Thomas, Turning points in catalysis, Angew. Chem. Int. Ed., 33 (1994) 913-937.

[5] A. Dyer, An introduction to zeolite molecular sieves, 1st ed., John Wiley & Sons, Chichester, 1988.

[6] S.M. Auerbach, K.A. Carrado, P.K. Dutta, Handbook of zeolite science and technology, Marcel Dekker, Inc., 2003.

[7] C. Baerlocher, L.B. McCusker, D.H. Olson, Atlas of zeolite framework types, 6th ed., Elsevier, amsterdam, 2007.

[8] J. Weitkamp, Zeolites and catalysis, Solid State Ionics, 131 (2000) 175-188.

[9] C.S. Cundy, P.A. Cox, The hydrothermal synthesis of zeolites: Precursors, intermediates and reaction mechanism, Microporous and Mesoporous Mater., 82 (2005) 1-78.

[10] H. Robson, Verified synthesis of zeolitic materials, 2nd ed., Elsevier, 2001.

[11] A. Corma, Inorganic solid acids and their use in acid-catalyzed hydrocarbon reactions, Chem. Rev., 95 (1995) 559-614.

[12] S. Bordiga, C. Lamberti, F. Bonino, A. Travert, F. Thibault-Starzyk, Probing zeolites by vibrational spectroscopies, Chem. Soc. Rev., 44 (2015) 7262-7341.

[13] M.-C. Silaghi, C. Chizallet, P. Raybaud, Challenges on molecular aspects of dealumination and desilication of zeolites, Microporous Mesoporous Mater., 191 (2014) 82-96.

[14] M.S. Holm, S. Svelle, F. Joensen, P. Beato, C.H. Christensen, S. Bordiga, M. Bjorgen, Assessing the acid properties of desilicated ZSM-5 by FTIR using CO and 2,4,6-trimethylpyridine (collidine) as molecular probes, Appl. Catal., A, 356 (2009) 23-30.

[15] W. Lutz, C.H. Ruscher, D. Heidemann, Determination of the framework and non-framework [SiO2] and [AlO2] species of steamed and leached faujasite type zeolites: calibration of IR, NMR, and XRD data by chemical methods, Microporous Mesoporous Mater., 55 (2002) 193-202.

[16] R.D. Shannon, K.H. Gardner, R.H. Staley, G. Bergeret, P. Gallezot, A. Auroux, The nature of the nonframework aluminum species formed during the dehydroxylation of H-Y, J. Phys. Chem., 89 (1985) 4778-4788.

[17] S. Li, A. Zheng, Y. Su, H. Zhang, L. Chen, J. Yang, C. Ye, F. Deng, Bronsted/Lewis acid synergy in dealuminated HY zeolite: A combined solid-state NMR and theoretical calculation study, J. Am. Chem. Soc., 129 (2007) 11161-11171.

[18] C.J.A. Mota, D.L. Bhering, N. Rosenbach, Jr., A DFT study of the acidity of ultrastable Y zeolite: Where is the Bronsted/Lewis acid synergism?, Angew. Chem., Int. Ed., 43 (2004) 3050-3053.

[19] S. Bordiga, I. Roggero, P. Ugliengo, A. Zecchina, V. Bolis, G. Artioli, R. Buzzoni, G. Marra, F. Rivetti, G. Spanò, Characterisation of defective silicalites, J. Chem. Soc., Dalton Transactions (2000) 3921-3929.

[20] R.F. Lobo, Introduction to the structural chemistry of zeolites, Marcel Dekker, Inc. (2003) 65-89.

[21] S.M. Csicsery, Catalysis by shape selective zeolites - science and technology, Pure Appl. Chem., 58 (1986) 841-856.

[22] B. Smit, T.L.M. Maesen, Towards a molecular understanding of shape selectivity, Nature, 451 (2008) 671-678.

[23] A. Corma, State of the art and future challenges of zeolites as catalysts, J. Catal., 216 (2003) 298-312.

[24] M. Stocker, Methanol-to-hydrocarbons: catalytic materials and their behavior, Microporous Mesoporous Mater., 29 (1999) 3-48.

[25] U. Olsbye, S. Svelle, M. Bjorgen, P. Beato, T.V.W. Janssens, F. Joensen, S. Bordiga, K.P. Lillerud, Conversion of methanol to hydrocarbons: How zeolite cavity and pore size controls product selectivity, Angew. Chem., Int. Ed., 51 (2012) 5810-5831.

[26] M.E. Davis, Ordered porous materials for emerging applications, Nature, 417 (2002) 813-821.

[27] R.E. Morris, P.S. Wheatley, Gas storage in nanoporous materials, Angew. Chem. Int. Ed., 47 (2008) 4966-4981.

[28] G.T. Kokotailo, J.L. Schlenker, F.G. Dwyer, E.W. Valyocsik, The framework topology of ZSM-22: a high-silica zeolite, Zeolites, 5 (1985) 349-351.

[29] B. Marler, Silica-ZSM-22: synthesis and single crystal structure refinement, Zeolites, 7 (1987) 393-397.

[30] B. Marler, C. Deroche, H. Gies, C.A. Fyfe, H. Groundey, G.T. Kokotailo, Y. Feng, S. Ernst, J. Weitkamp, D.E. Cox, The structure of zeolite ZSM-23 (MTT) refined from synchrotron x-ray powder data, J. Appl. Crystallogr., 26 (1993) 636-644.

[31] J.M. Thomas, G.R. Millward, D. White, S. Ramdas, Direct evidence to support the proposal that ZSM-23 is a recurrently twinned variant of zeolite Theta-1, J. Chem. Soc. (1988) 434-436.

[32] P.A. Wright, J.M. Thomas, G.R. Millward, S. Ramdas, S.A.I. Barri, ZSM-23: a suggested structure, J. Chem. Soc. (1985) 1117-1119.

[33] A.C. Rohrman, Jr., R.B. LaPierre, J.L. Schlenker, J.D. Wood, E.W. Valyocsik, M.K. Rubin, J.B. Higgins, W.J. Rohrbaugh, The framework topology of ZSM-23: a high silica zeolite, Zeolites, 5 (1985) 352-354.

[34] S. Ernst, R. Kumar, J. Weitkamp, Studies on the Kinetics of ZSM-23 Crystallization, American Chem. Soc. (1989) 560-573.

[35] S.-H. Lee, C.-H. Shin, D.-K. Yang, S.-D. Ahn, I.-S. Nam, S.B. Hong, Reinvestigation into the synthesis of zeolites using diquaternary alkylammonium ions as structure-directing agents, Microporous and Mesoporous Mater., 68 (2004) 97-104.

[36] D. Masih, T. Kobayashi, T. Baba, Hydrothermal synthesis of pure ZSM-22 under mild conditions, Chem. Commun. (2007) 3303-3305.

[37] S. Ernst, J. Weitkamp, J.A. Martens, P.A. Jacobs, Synthesis and shape-selective properties of ZSM-22, Appl. Catal., 48 (1989) 137-148.

[38] BP Statistical Review of World Energy, to be found under http://www.bp.com/statisticalreview. [accessed 2016/06/15].

[39] G.A. Olah, Beyond oil and gas: The methanol economy, Angew. Chem. Int. Ed., 44 (2005) 2636-2639.

[40] N.A. Owen, O.R. Inderwildi, D.A. King, The status of conventional world oil reserves-Hype or cause for concern?, Energy Policy, 38 (2010) 4743-4749.

[41] M.W. Erichsen, J.S. Martinez-Espin, F. Joensen, S. Teketel, P. del Campo Huertas, K.P. Lillerud, S. Svelle, P. Beato, U. Olsbye, Syngas to liquids via oxygenates, small-scale gas to liquid fuel synthesis (2015) 441.

[42] C.D. Chang, A.J. Silvestri, The conversion of methanol and other O-compounds to hydrocarbons over zeolite catalysts, J. Catal., 47 (1977) 249-259.

[43] C.D. Chang, The New Zealand gas-to-gasoline plant: An engineering tour de force, Catal. Today, 13 (1992) 103-111.

[44] J. Topp-Jørgensen, Topsøe integrated gasoline synthesis–The TIGAS process, Stud. Surf. Sci. Catal., 36 (1988) 293-305.

[45] J.Q. Chen, A. Bozzano, B. Glover, T. Fuglerud, S. Kvisle, Recent advancements in ethylene and propylene production using the UOP/Hydro MTO process, Catal. Today, 106 (2005) 103-107.

[46] H. Koempel, W. Liebner, Lurgi's methanol to propylene (MTP). Report on a successful commercialisation, Stud. Surf. Sci. Catal., Elsevier (2007) 261-267.

[47] R. Khare, D. Millar, A. Bhan, A mechanistic basis for the effects of crystallite size on light olefin selectivity in methanol-to-hydrocarbons conversion on MFI, J. Catal., 321 (2015) 23-31.

[48] N.Y. Chen, W.J. Reagan, Evidence of autocatalysis in methanol to hydrocarbon reactions over zeolite catalysts, J. Catal., 59 (1979) 123-129.

[49] R.M. Dessau, R.B. LaPierre, On the mechanism of methanol conversion to hydrocarbons over HZSM-5, J. Catal., 78 (1982) 136-141.

[50] R.M. Dessau, On the H-ZSM-5 catalyzed formation of ethylene from methanol or higher olefins, J. Catal., 99 (1986) 111-116.

[51] B.E. Langner, Reactions of methanol on zeolites with different pore structures, Appl. Catal., 2 (1982) 289-302.

[52] T. Mole, G. Bett, D. Seddon, Conversion of methanol to hydrocarbons over ZSM-5 zeolite: An examination of the role of aromatic hydrocarbons using 13carbon- and deuterium-labeled feeds, J. Catal., 84 (1983) 435-445.

[53] T. Mole, J.A. Whiteside, D. Seddon, Aromatic co-catalysis of methanol conversion over zeolite catalysts, J. of Catal., 82 (1983) 261-266.

[54] I.M. Dahl, S. Kolboe, On the reaction mechanism for propene formation in the MTO reaction over SAPO-34, Catal. Lett., 20 (1993) 329-336.

[55] I.M. Dahl, S. Kolboe, On the reaction mechanism for hydrocarbon formation from methanol over SAPO-34. 1. Isotopic labeling studies of the reaction of ethene with methanol, J. Catal., 149 (1994) 458-464.

[56] I.M. Dahl, S. Kolboe, On the reaction mechanism for hydrocarbon formation from methanol over SAPO-34, J. Catal., 161 (1996) 304-309.

[57] B. Arstad, S. Kolboe, Methanol-to-hydrocarbons reaction over SAPO-34. Molecules confined in the catalyst cavities at short time on stream, Catal. Lett., 71 (2001) 209-212.

[58] B. Arstad, S. Kolboe, The reactivity of molecules trapped within the SAPO-34 cavities in the methanol-to-hydrocarbons reaction, J. Am. Chem. Soc., 123 (2001) 8137-8138.

[59] W. Song, J.F. Haw, J.B. Nicholas, C.S. Heneghan, Methylbenzenes are the organic reaction centers for methanol-to-olefin catalysis on HSAPO-34, J. Am. Chem. Soc., 122 (2000) 10726-10727.

[60] M. Bjorgen, U. Olsbye, D. Petersen, S. Kolboe, The methanol-to-hydrocarbons reaction: insight into the reaction mechanism from [12C]benzene and [13C]methanol coreactions over zeolite H-beta, J. Catal., 221 (2004) 1-10.

[61] A. Sassi, M.A. Wildman, H.J. Ahn, P. Prasad, J.B. Nicholas, J.F. Haw, Methylbenzene chemistry on zeolite HBeta: Multiple insights into methanol-to-olefin catalysis, J. Phys. Chem. B, 106 (2002) 2294-2303.

[62] M. Hunger, M. Seiler, A. Buchholz, In situ MAS NMR spectroscopic investigation of the conversion of methanol to olefins on silicoaluminophosphates SAPO-34 and SAPO-18 under continuous flow conditions, Catal. Lett., 74 (2001) 61-68.

[63] M. Seiler, U. Schenk, M. Hunger, Conversion of methanol to hydrocarbons on zeolite HZSM-5 investigated by in situ MAS NMR spectroscopy under flow conditions and online gas chromatography, Catal. Lett., 62 (1999) 139-145.

[64] M. Seiler, W. Wang, A. Buchholz, M. Hunger, Direct evidence for a catalytically active role of the hydrocarbon pool formed on zeolite H-ZSM-5 during the methanol-to-olefin conversion, Catal. Lett., 88 (2003) 187-191.

[65] M. Bjorgen, S. Svelle, F. Joensen, J. Nerlov, S. Kolboe, F. Bonino, L. Palumbo, S. Bordiga, U. Olsbye, Conversion of methanol to hydrocarbons over zeolite H-ZSM-5: On the origin of the olefinic species, J. Catal., 249 (2007) 195-207.

[66] S. Svelle, F. Joensen, J. Nerlov, U. Olsbye, K.-P. Lillerud, S. Kolboe, M. Bjorgen, Conversion of methanol into hydrocarbons over zeolite H-ZSM-5: Ethene formation is mechanistically separated from the formation of higher alkenes, J. Am. Chem. Soc., 128 (2006) 14770-14771.

[67] M. Westgaard Erichsen, S. Svelle, U. Olsbye, The influence of catalyst acid strength on the methanol to hydrocarbons (MTH) reaction, Catal. Today, 215 (2013) 216-223.

[68] M. Bjoergen, F. Joensen, K.-P. Lillerud, U. Olsbye, S. Svelle, The mechanisms of ethene and propene formation from methanol over high silica H-ZSM-5 and H-beta, Catal. Today, 142 (2009) 90-97.

[69] M. Bjorgen, S. Akyalcin, U. Olsbye, S. Benard, S. Kolboe, S. Svelle, Methanol to hydrocarbons over large cavity zeolites: Towards a unified description of catalyst deactivation and the reaction mechanism, J. Catal., 275 (2010) 170-180.

[70] B.P.C. Hereijgers, F. Bleken, M.H. Nilsen, S. Svelle, K.-P. Lillerud, M. Bjorgen, B.M. Weckhuysen, U. Olsbye, Product shape selectivity dominates the Methanol-to-Olefins (MTO) reaction over H-SAPO-34 catalysts, J. Catal., 264 (2009) 77-87.

[71] S. Svelle, U. Olsbye, F. Joensen, M. Bjorgen, Conversion of methanol to alkenes over medium- and large-pore acidic zeolites: steric manipulation of the reaction intermediates governs the ethene/propene product selectivity, J. Phys. Chem. C, 111 (2007) 17981-17984.

[72] W. Song, H. Fu, J.F. Haw, Supramolecular origins of product selectivity for methanol-to-olefin catalysis on HSAPO-34, J. Am. Chem. Soc., 123 (2001) 4749-4754.

[73] J.H. Ahn, B. Temel, E. Iglesia, Selective homologation routes to 2,2,3-trimethylbutane on solid acids, Angew. Chem. Int. Ed., 48 (2009) 3814-3816.

[74] D.A. Simonetti, J.H. Ahn, E. Iglesia, Mechanistic details of acid-catalyzed reactions and their role in the selective synthesis of triptane and isobutane from dimethyl ether, J. Catal., 277 (2011) 173-195.

[75] M. Westgård Erichsen, S. Svelle, U. Olsbye, H-SAPO-5 as methanol-to-olefins (MTO) model catalyst: Towards elucidating the effects of acid strength, J. Catal., 298 (2013) 94-101.

[76] S. Teketel, M.W. Erichsen, F.L. Bleken, S.S.K.P. Lillerud, U. Olsbye, Shape selectivity in zeolite catalysis. The methanol to hydrocarbons (MTH) reaction, Catalysis, 26 (2014) 179-217.

[77] S. Teketel, U. Olsbye, K.-P. Lillerud, P. Beato, S. Svelle, Selectivity control through fundamental mechanistic insight in the conversion of methanol to hydrocarbons over zeolites, Microporous Mesoporous Mater., 136 (2010) 33-41.

[78] S. Teketel, W. Skistad, S. Benard, U. Olsbye, K.P. Lillerud, P. Beato, S. Svelle, Shape selectivity in the conversion of methanol to hydrocarbons: The catalytic performance of one-dimensional 10-ring zeolites: ZSM-22, ZSM-23, ZSM-48, and EU-1, ACS Catal., 2 (2012) 26-37.

[79] S. Teketel, S. Svelle, K.-P. Lillerud, U. Olsbye, Shape-selective conversion of methanol to hydrocarbons over 10-ring unidirectional-channel acidic H-ZSM-22, ChemCatChem, 1 (2009) 78-81.

[80] S. Ilias, R. Khare, A. Malek, A. Bhan, A descriptor for the relative propagation of the aromatic- and olefin-based cycles in methanol-to-hydrocarbons conversion on H-ZSM-5, J. Catal., 303 (2013) 135-140.

[81] R. Khare, A. Bhan, Mechanistic studies of methanol-to-hydrocarbons conversion on diffusion-free MFI samples, J. Catal., 329 (2015) 218-228.

[82] B.-M. Kim, E.k. Park, S.-Y. LeeAn, M. Ha, E.-J. Kim, H. Kwon, Y.-C. Hong, W.-C. Jeong, J. Hur, H.-K. Cheong, J. Yi, J.H. Kim, B.-E. Lee, J.-H. Seo, M.-H. Chang, E.-H. Ha, BTEX exposure and its health effects in pregnant women following the Hebei Spirit oil spill, J. Prev. Med. Public Health, 42 (2009) 96-103.

[83] U. Olsbye, S. Svelle, K.P. Lillerud, Z.H. Wei, Y.Y. Chen, J.F. Li, J.G. Wang, W.B. Fan, The formation and degradation of active species during methanol conversion over protonated zeotype catalysts, Chem. Soc. Rev., (2015) DOI 10.1039/c5cs00304k.

[84] J. Li, Y. Wei, G. Liu, Y. Qi, P. Tian, B. Li, Y. He, Z. Liu, Comparative study of MTO conversion over SAPO-34, H-ZSM-5 and H-ZSM-22: Correlating catalytic performance and reaction mechanism to zeolite topology, Catal. Today, 171 (2011) 221-228.

[85] J. Li, Y. Wei, Y. Qi, P. Tian, B. Li, Y. He, F. Chang, X. Sun, Z. Liu, Conversion of methanol over H-ZSM-22: The reaction mechanism and deactivation, Catal. Today, 164 (2011) 288-292.

[86] T.V.W. Janssens, S. Svelle, U. Olsbye, Kinetic modeling of deactivation profiles in the methanol-to-hydrocarbons (MTH) reaction: A combined autocatalytic-hydrocarbon pool approach, J. Catal., 308 (2013) 122-130.

[87] D. Rojo-Gama, S. Etemadi, E. Kirby, K.P. Lillerud, P. Beato, S. Svelle, U. Olsbye, Time- and space-resolved study of the Methanol to Hydrocarbons (MTH) reaction - influence of zeolite topology on deactivation patterns, Faraday Discuss., (2016). DOI 10.1039/C6FD00187D.

[88] F. Bleken, M. Bjorgen, L. Palumbo, S. Bordiga, S. Svelle, K.-P. Lillerud, U. Olsbye, The effect of acid strength on the conversion of methanol to olefins over acidic microporous catalysts with the CHA topology, Top. Catal., 52 (2009) 218-228.

[89] T.V.W. Janssens, A new approach to the modeling of deactivation in the conversion of methanol on zeolite catalysts, J. Catal., 264 (2009) 130-137.

[90] S. Mueller, Y. Liu, M. Vishnuvarthan, X. Sun, A.C. van Veen, G.L. Haller, M. Sanchez-Sanchez, J.A. Lercher, Coke formation and deactivation pathways on H-ZSM-5 in the conversion of methanol to olefins, J. Catal., 325 (2015) 48-59.

[91] M. Guisnet, L. Costa, F.R. Ribeiro, Prevention of zeolite deactivation by coking, J. Mol. Catal. A: Chem., 305 (2009) 69-83.

[92] J.W. Park, S.J. Kim, M. Seo, S.Y. Kim, Y. Sugi, G. Seo, Product selectivity and catalytic deactivation of MOR zeolites with different acid site densities in methanol-to-olefin (MTO) reactions, Appl. Catal., A, 349 (2008) 76-85.

[93] A. Corma, From microporous to mesoporous molecular sieve materials and their use in catalysis, Chem. Rev., 97 (1997) 2373-2420.

[94] R. Chal, C. Gerardin, M. Bulut, D.S. van, Overview and industrial assessment of synthesis strategies towards zeolites with mesopores, ChemCatChem, 3 (2011) 67-81.

[95] M. Hartmann, Hierarchical zeolites: A proven strategy to combine shape selectivity with efficient mass transport, Angew. Chem., Int. Ed., 43 (2004) 5880-5882.

[96] M. Hartmann, A.G. Machoke, W. Schwieger, Catalytic test reactions for the evaluation of hierarchical zeolites, Chem. Soc. Rev., 45 (2016) 3313-3330.

[97] M.S. Holm, E. Taarning, K. Egeblad, C.H. Christensen, Catalysis with hierarchical zeolites, Catalysis Today, 168 (2011) 3-16.

[98] K. Li, J. Valla, J. Garcia ‐ Martinez, Realizing the commercial potential of hierarchical zeolites: new opportunities in catalytic cracking, ChemCatChem, 6 (2014) 46-66.

[99] S. Mitchell, A.B. Pinar, J. Kenvin, P. Crivelli, J. Karger, J. Perez-Ramirez, Structural analysis of hierarchically organized zeolites, Nat. Commun., 6 (2015) 8633.

[100] K. Moller, T. Bein, Mesoporosity-a new dimension for zeolites, Chem Soc Rev, 42 (2013) 3689-3707.

[101] K. Na, G. Somorjai, Hierarchically nanoporous zeolites and their heterogeneous catalysis: Current status and future perspectives, Catal. Lett., 145 (2015) 193-213.

[102] J. Perez-Ramirez, C.H. Christensen, K. Egeblad, C.H. Christensen, J.C. Groen, Hierarchical zeolites: enhanced utilisation of microporous crystals in catalysis by advances in materials design, Chem. Soc. Rev., 37 (2008) 2530-2542.

[103] D.P. Serrano, J.M. Escola, P. Pizarro, Synthesis strategies in the search for hierarchical zeolites, Chem. Soc. Rev., 42 (2013) 4004-4035.

[104] J. Shi, Y. Wang, W. Yang, Y. Tang, Z. Xie, Recent advances of pore system construction in zeolite-catalyzed chemical industry processes, Chem. Soc. Rev., 44 (2015) 8877-8903.

[105] V. Valtchev, G. Majano, S. Mintova, J. Pérez-Ramírez, Tailored crystalline microporous materials by post-synthesis modification, Chem. Soc. Rev., 42 (2013) 263-290.

[106] D. Verboekend, J. Perez-Ramirez, Design of hierarchical zeolite catalysts by desilication, Catal. Sci. Technol., 1 (2011) 879-890.

[107] D. Schneider, D. Mehlhorn, P. Zeigermann, J. Kärger, R. Valiullin, Transport properties of hierarchical micro–mesoporous materials, Chem. Soc. Rev., 45 (2016) 3439-3467.

[108] K. Möller, T. Bein, Crystallization and porosity of ZSM-23, Microporous and Mesoporous Mater., 143 (2011) 253-262.

[109] J.C. Groen, T. Sano, J.A. Moulijn, J. Pérez-Ramírez, Alkaline-mediated mesoporous mordenite zeolites for acid-catalyzed conversions, J. Catal., 251 (2007) 21-27.

[110] J. Perez-Ramirez, S. Abello, A. Bonilla, J.C. Groen, Tailored mesoporosity development in zeolite crystals by partial detemplation and desilication, Adv. Funct. Mater., 19 (2009) 164-172.

[111] A. Čimek, B. Subotić, I. Šmit, A. Tonejc, R. Aiello, F. Crea, A. Nastro, Dissolution of high-silica zeolites in alkaline solutions II. Dissolution of 'activated'silicalite-1 and ZSM-5 with different aluminum content, Microporous Materm, 8 (1997) 159-169.

[112] R.M. Dessau, E.W. Valyocsik, N.H. Goeke, Aluminum zoning in ZSM 5 as revealed by selective silica removal, Zeolites, 12 (1992) 776-779.

[113] J.C. Groen, T. Bach, U. Ziese, A.M. Paulaime van Donk, K.P. de Jong, J.A. Moulijn, J. Perez-Ramirez, Creation of hollow zeolite architectures by controlled desilication of Al-zoned ZSM-5 crystals, J. Am. Chem. Soc., 127 (2005) 10792-10793.

[114] J.C. Groen, J.C. Jansen, J.A. Moulijn, J. Perez-Ramirez, Optimal Aluminum-assisted mesoporosity development in MFI zeolites by desilication, J. Phys. Chem. B, 108 (2004) 13062-13065.

[115] R. Dessau, E. Valyocsik, N. Goeke, Aluminum zoning in ZSM-5 as revealed by selective silica removal, Zeolites, 12 (1992) 776-779.

[116] J.C. Groen, W. Zhu, S. Brouwer, S.J. Huynink, F. Kapteijn, J.A. Moulijn, J. Perez-Ramirez, Direct demonstration of enhanced diffusion in mesoporous ZSM-5 zeolite obtained via controlled desilication, J. Am. Chem. Soc., 129 (2007) 355-360.

[117] N. Chaouati, A. Soualah, I. Hussein, J. Comparot, L. Pinard, Formation of weak and strong Brønsted acid sites during alkaline treatment on MOR zeolite, Appl. Catal. A: General, 526 (2016) 95-104.

[118] X. Li, R. Prins, J.A. van Bokhoven, Synthesis and characterization of mesoporous mordenite, J. Catal., 262 (2009) 257-265.

[119] V. Paixão, A.P. Carvalho, J. Rocha, A. Fernandes, A. Martins, Modification of MOR by desilication treatments: structural, textural and acidic characterization, Microporous and Mesoporous Mater., 131 (2010) 350-357.

[120] A.N.C. van Laak, S.L. Sagala, J. Zečević, H. Friedrich, P.E. de Jongh, K.P. de Jong, Mesoporous mordenites obtained by sequential acid and alkaline treatments – Catalysts for cumene production with enhanced accessibility, J. Catal., 276 (2010) 170-180.

[121] A.N.C. van laak, R.W. Gosselink, S.L. Sagala, J.D. Meeldijk, P.E. de Jongh, K.P. de Jong, Alkaline treatment on commercially available aluminum rich mordenite, Appl. Catal., A, 382 (2010) 65-72.

[122] O. Muraza, M.A. Sanhoob, M.A.B. Siddiqui, Fabrication of desilicated MTW zeolite and its application in catalytic cracking of n-heptane, Adv. Powder Technology, 27 (2016) 372-378.

[123] M. Ogura, E. Kikuchi, M. Matsukata, MFI zeolite with uniform mesopores created by alkali treatment, Stud. Surf. Sci. Catal., 135 (2001) 1820-1827.

[124] S. Svelle, L. Sommer, K. Barbera, P.N.R. Vennestrom, U. Olsbye, K.P. Lillerud, S. Bordiga, Y.-H. Pan, P. Beato, How defects and crystal morphology control the effects of desilication, Catal. Today, 168 (2011) 38-47.

[125] J.C. Groen, L.A.A. Peffer, J.A. Moulijn, J. Perez-Ramirez, On the introduction of intracrystalline mesoporosity in zeolites upon desilication in alkaline medium, Microporous Mesoporous Mater., 69 (2004) 29-34.

[126] D. Verboekend, S. Mitchell, J. Perez-Ramirez, Hierarchical zeolites overcome all obstacles: next stop industrial implementation, Chimia, 67 (2013) 327-332.

[127] D. Verboekend, A.M. Chabaneix, K. Thomas, J.-P. Gilson, J. Perez-Ramirez, Mesoporous ZSM-22 zeolite obtained by desilication: peculiarities associated with crystal morphology and aluminum distribution, CrystEngComm, 13 (2011) 3408-3416.

[128] S. Liu, J. Ren, H. Zhang, E. Lv, Y. Yang, Y.-W. Li, Synthesis, characterization and isomerization performance of micro/mesoporous materials based on H-ZSM-22 zeolite, J. Catal., 335 (2016) 11-23.

[129] M.H.M. Ahmed, O. Muraza, A.M. Al Amer, Y. Sugiura, N. Nishiyama, Development of desilicated EU-1 zeolite and its application in conversion of dimethyl ether to olefins, Microporous Mesoporous Mater., 207 (2015) 9-16.

[130] B. Gil, L. Mokrzycki, B. Sulikowski, Z. Olejniczak, S. Walas, Desilication of ZSM-5 and ZSM-12 zeolites: Impact on textural, acidic and catalytic properties, Catal. Today, 152 (2010) 24-32.

[131] Ł. Mokrzycki, B. Sulikowski, Z. Olejniczak, Properties of desilicated ZSM-5, ZSM-12, MCM-22 and ZSM-12/MCM-41 derivatives in isomerization of α-pinene, Catal. Lett., 127 (2009) 296-303.

[132] D. Verboekend, L.A. Villaescusa, K. Thomas, I. Stan, J. Perez-Ramirez, Acidity and accessibility studies on mesoporous ITQ-4 zeolite, Catal. Today, 152 (2010) 11-16.

[133] D. Verboekend, J. Perez-Ramirez, Desilication mechanism revisited: Highly mesoporous all-silica zeolites enabled through pore-directing agents, Chem. Eur. J., 17 (2011) 1137-1147.

[134] I.I. Ivanova, I.A. Kasyanov, A.A. Maerle, V.I. Zaikovskii, Mechanistic study of zeolites recrystallization into micro-mesoporous materials, Microporous and Mesoporous Mater., 189 (2014) 163-172.

[135] F. Schmidt, M.R. Lohe, B. Buechner, F. Giordanino, F. Bonino, S. Kaskel, Improved catalytic performance of hierarchical ZSM-5 synthesized by desilication with surfactants, Microporous Mesoporous Mater., 165 (2013) 148-157.

[136] W.C. Yoo, X. Zhang, M. Tsapatsis, A. Stein, Synthesis of mesoporous ZSM-5 zeolites through desilication and re-assembly processes, Microporous Mesoporous Mater., 149 (2012) 147-157.

[137] I.I. Ivanova, E.E. Knyazeva, Micro–mesoporous materials obtained by zeolite recrystallization: synthesis, characterization and catalytic applications, Chem. Soc. Rev., 42 (2013) 3671-3688.

[138] I.I. Ivanova, A.S. Kuznetsov, E.E. Knyazeva, F. Fajula, F. Thibault-Starzyk, C. Fernandez, J.P. Gilson, Design of hierarchically structured catalysts by mordenites recrystallization: Application in naphthalene alkylation, Catal. Today, 168 (2011) 133-139.

[139] V. Ordomsky, I. Ivanova, E. Knyazeva, V. Yuschenko, V. Zaikovskii, Cumene disproportionation over micro/mesoporous catalysts obtained by recrystallization of mordenite, J. Catal., 295 (2012) 207-216.

[140] S. Abello, A. Bonilla, J. Perez-Ramirez, Mesoporous ZSM-5 zeolite catalysts prepared by desilication with organic hydroxides and comparison with NaOH leaching, Appl. Catal., A, 364 (2009) 191-198.

[141] J. Perez-Ramirez, D. Verboekend, A. Bonilla, S. Abello, Zeolite catalysts with tunable hierarchy factor by pore-growth moderators, Adv. Funct. Mater., 19 (2009) 3972-3979.

[142] K. Mlekodaj, K. Tarach, J. Datka, K. Gora-Marek, W. Makowski, Porosity and accessibility of acid sites in desilicated ZSM-5 zeolites studied using adsorption of probe molecules, Microporous Mesoporous Mater., 183 (2014) 54-61.

[143] K. Sadowska, K. Gora-Marek, M. Drozdek, P. Kustrowski, J. Datka, J. Martinez Triguero, F. Rey, Desilication of highly siliceous zeolite ZSM-5 with NaOH and NaOH/tetrabutylamine hydroxide, Microporous Mesoporous Mater., 168 (2013) 195-205.

[144] K. Sadowska, A. Wach, Z. Olejniczak, P. Kustrowski, J. Datka, Hierarchic zeolites: Zeolite ZSM-5 desilicated with NaOH and NaOH/tetrabutylamine hydroxide, Microporous Mesoporous Mater., 167 (2013) 82-88.

[145] D. Verboekend, M. Milina, S. Mitchell, J. Perez-Ramirez, Hierarchical zeolites by desilication: Occurrence and catalytic impact of recrystallization and restructuring, Cryst. Growth Des., 13 (2013) 5025-5035.

[146] K. Tarach, K. Gora-Marek, J. Tekla, K. Brylewska, J. Datka, K. Mlekodaj, W. Makowski, M.C. Igualada Lopez, J. Martinez Triguero, F. Rey, Catalytic cracking performance of alkaline-treated zeolite Beta in the terms of acid sites properties and their accessibility, J. Catal., 312 (2014) 46-57.

[147] M. Dyballa, U. Obenaus, M. Rosenberger, A. Fischer, H. Jakob, E. Klemm, M. Hunger, Post-synthetic improvement of H-ZSM-22 zeolites for the methanol-to-olefin conversion, Microporous Mesoporous Mater., 233 (2016) 26-30.

[148] J.A. Martens, D. Verboekend, K. Thomas, G. Vanbutsele, J. Perez-Ramirez, J.-P. Gilson, Hydroisomerization and hydrocracking of linear and multibranched long model alkanes on hierarchical Pt/ZSM-22 zeolite, Catal. Today, 218 (2013) 135-142.

[149] D. Verboekend, K. Thomas, M. Milina, S. Mitchell, J. Perez-Ramirez, J.-P. Gilson, Towards more efficient monodimensional zeolite catalysts: n-alkane hydro-isomerisation on hierarchical ZSM-22, Catal. Sci. Technol., 1 (2011) 1331-1335.

[150] P. Matias, C.C. Sa, I. Graca, J.M. Lopes, A.P. Carvalho, R.F. Ramoa, M. Guisnet, Desilication of a TON zeolite with NaOH: Influence on porosity, acidity and catalytic properties, Appl. Catal., A, 399 (2011) 100-109.

[151] C. Martinez, E.J. Doskocil, A. Corma, Improved THETA-1 for light olefins oligomerization to diesel: influence of textural and acidic properties, Top. Catal., 57 (2014) 668-682.

[152] M.H.M. Ahmed, O. Muraza, A.M. Al Amer, K. Miyake, N. Nishiyama, Development of hierarchical EU-1 zeolite by sequential alkaline and acid treatments for selective dimethyl ether to propylene (DTP), Appl. Catal., A, 497 (2015) 127-134.

[153] M. Bjoergen, F. Joensen, H.M. Spangsberg, U. Olsbye, K.-P. Lillerud, S. Svelle, Methanol to gasoline over zeolite H-ZSM-5: Improved catalyst performance by treatment with NaOH, Appl. Catal., A, 345 (2008) 43-50.

[154] F.L. Bleken, K. Barbera, F. Bonino, U. Olsbye, K.P. Lillerud, S. Bordiga, P. Beato, T.V.W. Janssens, S. Svelle, Catalyst deactivation by coke formation in microporous and desilicated zeolite H-ZSM-5 during the conversion of methanol to hydrocarbons, J. Catal., 307 (2013) 62-73.

[155] S. Fathi, M. Sohrabi, C. Falamaki, Improvement of HZSM-5 performance by alkaline treatments: Comparative catalytic study in the MTG reactions, Fuel, 116 (2014) 529-537.

[156] J. Kim, M. Choi, R. Ryoo, Effect of mesoporosity against the deactivation of MFI zeolite catalyst during the methanol-to-hydrocarbon conversion process, J. Catal., 269 (2010) 219-228.

[157] C. Mei, P. Wen, Z. Liu, H. Liu, Y. Wang, W. Yang, Z. Xie, W. Hua, Z. Gao, Selective production of propylene from methanol: Mesoporosity development in high silica HZSM-5, J. Catal., 258 (2008) 243-249.

[158] F. Schmidt, C. Hoffmann, F. Giordanino, S. Bordiga, P. Simon, W. Carrillo-Cabrera, S. Kaskel, Coke location in microporous and hierarchical ZSM-5 and the impact on the MTH reaction, J. Catal., 307 (2013) 238-245.

[159] M. Milina, S. Mitchell, P. Crivelli, D. Cooke, J. Pérez-Ramírez, Mesopore quality determines the lifetime of hierarchically structured zeolite catalysts, Nature Commun., 5 (2014) 3922.

[160] C. Sá Couto, P. Matias, E.T. Santos, A. Fernandes, I. Graça, J.M. Lopes, M.F. Ribeiro, Towards a deep desilication/dealumination of NU-10 zeolite: Shape-selectivity regulation, Eur. J. Inorg. Chem., 2012 (2012) 4190-4199.

[161] O. Muraza, I.A. Bakare, T. Tago, H. Konno, A.-l. Adedigba, A.M. Al-Amer, Z.H. Yamani, T. Masuda, Controlled and rapid growth of MTT zeolite crystals with low-aspect-ratio in a microwave reactor, Chem. Eng. Journal, 226 (2013) 367-376.

[162] W. Aslam, M.A.B. Siddiqui, B. Rabindran Jermy, A. Aitani, J. Cejka, S. Al-Khattaf, Selective synthesis of linear alkylbenzene by alkylation of benzene with 1-dodecene over desilicated zeolites, Catal. Today, 227 (2014) 187-197.

[163] D. Verboekend, J.C. Groen, J. Perez-Ramirez, Interplay of properties and functions upon introduction of mesoporosity in ITQ-4 zeolite, Adv. Funct. Mater., 20 (2010) 1441-1450.

[164] S.J.S.K.S.W. Gregg, Adsorption, surface area and porosity, Academic Press, London, 1982.

[165] J. Rouquerol, F. Rouquerol, P. Llewellyn, G. Maurin, K.S. Sing, Adsorption by powders and porous solids: principles, methodology and applications, Academic press, 2013.

[166] M. Thommes, Physical adsorption characterization of ordered and amorphous mesoporous materials, Ser. Chem. Eng., 4 (2004) 317-364.

[167] G. Leofanti, M. Padovan, G. Tozzola, B. Venturelli, Surface area and pore texture of catalysts, Catal. Today, 41 (1998) 207-219.

[168] J. Rouquerol, P. Llewellyn, F. Rouquerol, Is the bet equation applicable to microporous adsorbents?, Stud. Surf. Sci. Catal., 160 (2007) 49-56.

[169] B.C. Lippens, J.H. de Boer, Pore systems in catalysts. V. The t-method, J. Catal., 4 (1965) 319-323.

[170] B.C. Lippens, B.G. Linsen, J.H. de Boer, Pore systems in catalysts. I. Adsorption of nitrogen; apparatus and calculation, J. Catal., 3 (1964) 32-37.

[171] E.P. Barrett, L.G. Joyner, P.P. Halenda, The determination of pore volume and area distributions in porous substances. I. Computations from nitrogen isotherms, J. Am. Chem. Soc., 73 (1951) 373-380.

[172] J.C. Groen, L.A.A. Peffer, J. Perez-Ramirez, Pore size determination in modified micro- and mesoporous materials. Pitfalls and limitations in gas adsorption data analysis, Microporous Mesoporous Mater., 60 (2003) 1-17.

[173] J.C. Groen, J. Perez-Ramirez, Critical appraisal of mesopore characterization by adsorption analysis, Appl. Catal., A, 268 (2004) 121-125.

[174] F. Geobaldo, S. Fiorilli, B. Onida, G. Giordano, A. Katovic, E. Garrone, An FTIR study of zeolite Theta-1, J. Phys. Chem. B, 107 (2003) 1258-1262.

[175] K. Barbera, F. Bonino, S. Bordiga, T.V.W. Janssens, P. Beato, Structure-deactivation relationship for ZSM-5 catalysts governed by framework defects, J. Catal., 280 (2011) 196-205.

[176] C. Emeis, Determination of integrated molar extinction coefficients for infrared absorption bands of pyridine adsorbed on solid acid catalysts, J. Catal., 141 (1993) 347-354.

[177] C. Pereira, R.J. Gorte, Method for distinguishing Brønsted-acid sites in mixtures of H-ZSM-5, H-Y and silica-alumina, Appl. Catal. A, General, 90 (1992) 145-157.

[178] K. Hayasaka, D. Liang, W. Huybrechts, B.R. De Waele, K.J. Houthoofd, P. Eloy, E.M. Gaigneaux, G. van Tendeloo, J.W. Thybaut, G.B. Marin, J.F.M. Denayer, G.V. Baron, P.A. Jacobs, C.E.A. Kirschhock, J.A. Martens, Formation of ZSM-22 zeolite catalytic particles by fusion of elementary nanorods, Chem. Eur. J., 13 (2007) 10070-10077.

[179] A.W. Burton, S.I. Zones, T. Rea, I.Y. Chan, Preparation and characterization of SSZ-54: A family of MTT/TON intergrowth materials, Microporous and Mesoporous Mater., 132 (2010) 54-59.

[180] S. Müller, Y. Liu, F.M. Kirchberger, M. Tonigold, M. Sanchez-Sanchez, J.A. Lercher, Hydrogen transfer pathways during zeolite catalyzed methanol conversion to hydrocarbons, J. Am. Chem. Soc., 138 (2016) 15994-16003.

[181] I. Yarulina, S. Bailleul, A. Pustovarenko, J.R. Martinez, K.D. Wispelaere, J. Hajek, B.M. Weckhuysen, K. Houben, M. Baldus, V. Van Speybroeck, Suppression of the aromatic cycle in methanol-to-olefins reaction over ZSM-5 by post-synthetic modification using Calcium, ChemCatChem, 8 (2016) 3057-3063.

[182] S. Teketel, U. Olsbye, K.P. Lillerud, P. Beato, S. Svelle, Co-conversion of methanol and light alkenes over acidic zeolite catalyst H-ZSM-22: Simulated recycle of non-gasoline range products, Appl. Catal., A, 494 (2015) 68-76.

[183] Z.-M. Cui, Q. Liu, Z. Ma, S.-W. Bian, W.-G. Song, Direct observation of olefin homologations on zeolite ZSM-22 and its implications to methanol to olefin conversion, J. Catal., 258 (2008) 83-86.

[184] J. Li, Y. Qi, Z. Liu, G. Liu, D. Zhang, Co-reaction of ethene and methylation agents over SAPO-34 and ZSM-22, Catal. Lett., 121 (2008) 303-310.

[185] S. Muller, Y. Liu, M. Sanchez-Sanchez, J.A. Lercher, Deactivation pathways during methanol to propylene (MTP) conversion over ZSM-5 catalysts, Am. Chem. Soc., 248 (2014).

Appendix

A.1. Additional results

Table A.1

Yield, composition and textural properties for the ZSM-22 investigated samples.

Sample	Yield[a] (%)	Si/Al ratio[b] (mol mol^{-1})	Pore volume (cm^3 g^{-1})			Surface area (m^2 g^{-1})	
			V_{total}[c]	V_{micro}[d]	V_{ext}[e]	S_{BET}	S_{ext}[d]
c-ZSM-22	-	49	0.15	0.08	0.07	232	33
c-ZSM-22-*at1*	60	35	0.30	0.08	0.22	257	65
c-ZSM-22-*at2*	46	31	0.53	0.08	0.45	247	60
c-ZSM-22-*at1-HCl*	-	48	0.56	0.08	0.48	276	82
c-ZSM-22-*at2-HCl*	-	46	0.53	0.07	0.46	251	68
c-ZSM-22-*ats1*	82	40	0.26	0.07	0.19	233	61
c-ZSM-22-*ats2*	51	29	0.48	0.06	0.42	263	118
c-ZSM-22-*ats1-HCl*	-	50	0.29	0.08	0.21	257	58
c-ZSM-22-*ats2-HCl*	-	48	0.52	0.07	0.45	296	114
c-ZSM-22-*tba1*	88	33	0.23	0.08	0.14	232	43
c-ZSM-22-*tba2*	75	32	0.21	0.05	0.16	171	35
c-ZSM-22-*tba1-HCl*	-	54	0.26	0.09	0.17	257	49
c-ZSM-22-*tba2-HCl*	-	47	0.29	0.09	0.20	272	44
c-ZSM-22-*HCl*	-	52	0.14	0.08	0.06	214	21
m-ZSM-22	-	38	0.39	0.05	0.34	163	26
m-ZSM-22-*at1*	60	29	0.57	0.07	0.50	216	40
m-ZSM-22-*at2*	48	25	0.53	0.07	0.47	202	38
m-ZSM-22-*at1-HCl*	-	36	0.56	0.08	0.48	236	39
m-ZSM-22-*at2-HCl*	-	37	0.59	0.08	0.51	257	45
m-ZSM-22-*ats1*	83	30	0.44	0.02	0.42	88	35
m-ZSM-22-*ats2*	58	22	0.34	0.01	0.33	47	23
m-ZSM-22-*ats1-HCl*	-	34	0.23	0.03	0.20	108	29
m-ZSM-22-*ats2-HCl*	-	21	0.14	0.01	0.13	47	21
m-ZSM-22-*tba1*	90	28	0.39	0.06	0.33	178	22
m-ZSM-22-*tba2*	82	26	0.17	0.01	0.16	73	43
m-ZSM-22-*tba1-HCl*	-	39	0.42	0.08	0.34	213	21
m-ZSM-22-*tba2-HCl*	-	39	0.31	0.07	0.24	211	32

[a] 100 – weight loss (%) after desilication.

[b] Determined by MP-AES.

[c] Volume adsorbed at $p/p_0 = 0.99$.

[d] *t*-plot method. V_{ext} and S_{ext} represent the pore volume and surface area for all the pores except the micropores.

[e] $V_{total} - V_{micro}$.

Table A.2

Acidic properties for selected ZSM-22 protonated zeolites.

Sample	c_{BAS}[a] (µmol g^{-1})	c_{LAS}[a] (µmol g^{-1})	c_{BAS} + c_{LAS} (µmol g^{-1})	c_{Al}[b] (µmol g^{-1})	Acidic sites[c] (%)
c-ZSM-22	240	30	270	340	79
c-ZSM-22-*at1*	240	130	370	476	78
c-ZSM-22-*at1-HCl*	-	-	-	347	-
c-ZSM-22-*ats1*	210	130	340	417	82
c-ZSM-22-*ats1-HCl*	220	100	320	333	96
c-ZSM-22-*tba2*	330	120	450	521	86
c-ZSM-22-*tba2-HCl*	280	70	350	355	98
m-ZSM-22	240	30	270	439	62
m-ZSM-22-*at1*	440	130	570	575	99
m-ZSM-22-*at1-HCl*	380	50	430	463	93
m-ZSM-22-*ats1*	150	40	190	556	34
m-ZSM-22-*ats1-HCl*	210	50	260	490	53
m-ZSM-22-*tba1*	460	70	530	595	89
m-ZSM-22-*tba1-HCl*	370	40	410	427	96

[a]Amount of Brønsted or Lewis acid sites determined by IR spectroscopy of adsorbed pyridine.

[b]Total Al concentration calculated from elemental analysis.

[c]Total acid sites reached by pyridine (c_{BAS} + c_{LAS}) / total Al concentration (c_{Al}) in %.

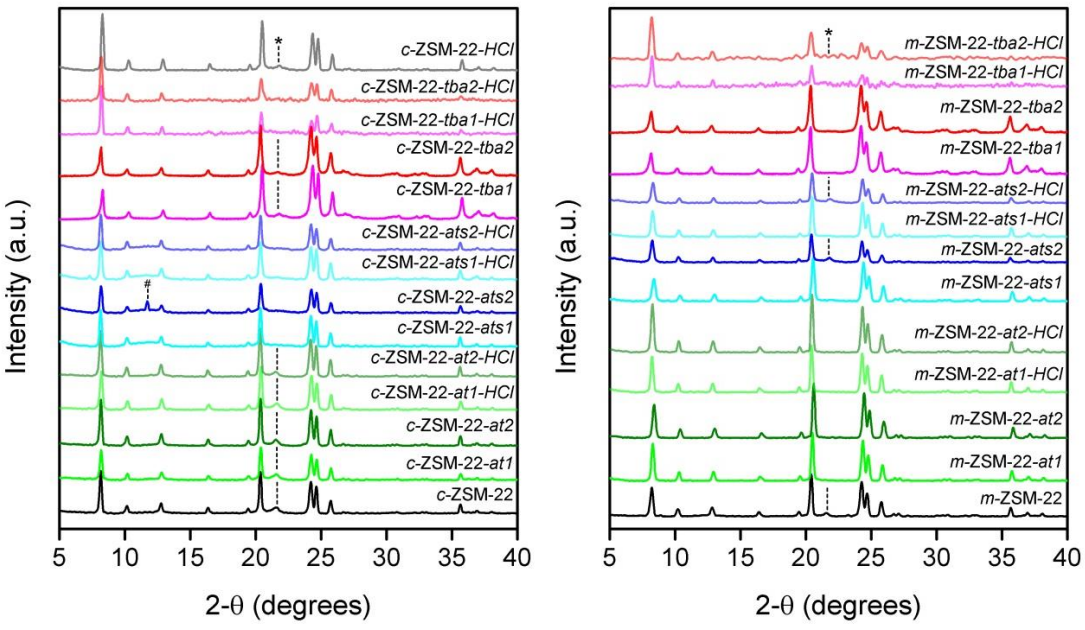

Figure A.1. PXRD patterns of parent and post-synthetic treated commercial (**left**) and in house prepared (**right**) ZSM-22 samples. (*) and (#) indicate the position of a cristobalite or undefined impurity, respectively.

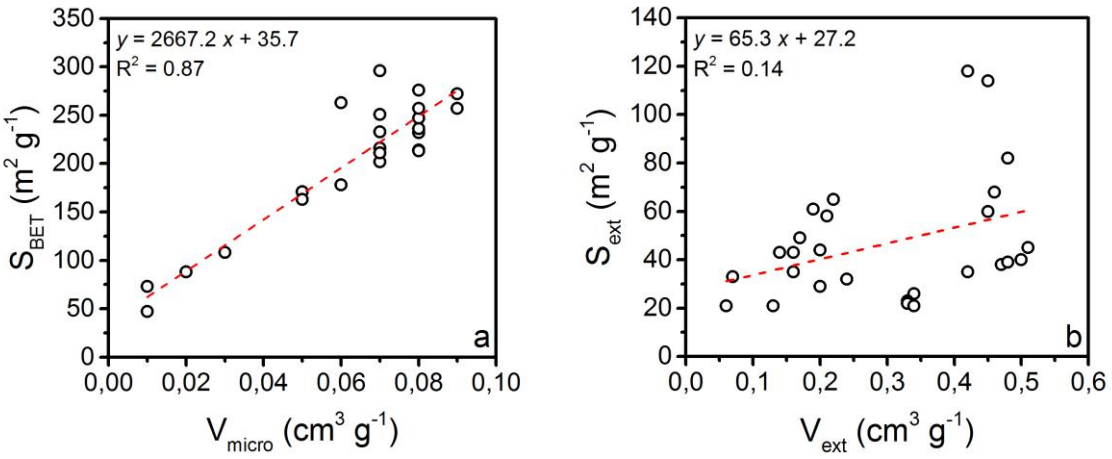

Figure A.2. Correlations between (**a**) total surface area (S_{BET}) and micropore volume (V_{micro}) and (**b**) external surface area (S_{ext}) and external volume (V_{ext}) for the treated samples.

Table A.3

Si/Al ratio and total methanol conversion capacity of the H-ZSM-22 and H-ZSM-23 catalyst not present in 5.2.

Catalyst	Si/Al[a]	Methanol conversion capacity[b] (g_{MeOH} $g^{-1}_{catalyst}$)
c-ZSM-22-*at1*	35	5.9
c-ZSM-22-*at2*	31	2.9
c-ZSM-22-*at2-HCl*	46	10.9
c-ZSM-22-*ats1*	40	8.2
c-ZSM-22-*ats2*	29	5.9
c-ZSM-22-*tba1*	33	4.5
c-ZSM-22-*tba1-HCl*	54	5.4
c-ZSM-22-*tba2*	32	2.7
m-ZSM-22-*at1*	29	4.8
m-ZSM-22-*ats1*	30	1.4
m-ZSM-22-*tba1*	28	7.2

[a]From MP-AES.

[b]Total grams of methanol converted per gram of catalyst before complete deactivation.

Table A.4

Methanol conversion capacity, composition and textural properties for the ZSM-23 samples.

Sample	MeOH conv capacity ($g\ g^{-1}$)	Si/Al ratio[a] ($mol\ mol^{-1}$)	Pore volume ($cm^3\ g^{-1}$)			Surface area ($m^2\ g^{-1}$)	
			V_{total}[b]	V_{micro}[c]	V_{ext}[d]	S_{BET}	S_{ext}[c]
c-ZSM-23	2.7	24	0.31	0.02	0.29	103	50
c-ZSM-23-*at1*	1.9	19	0.72	0.03	0.69	153	76
c-ZSM-23-*at2*	0.7	13	0.64	0.03	0.61	146	82
c-ZSM-23-*at1-HCl*	11.8	25	0.47	0.06	0.41	216	63
c-ZSM-23-*at2-HCl*	8.9	26	0.89	0.06	0.83	253	107
c-ZSM-23-*ats1*	-	-	0.77	0.02	0.74	101	65
c-ZSM-23-*ats2*	-	-	0.71	0.004	0.706	79	70
c-ZSM-23-*ats1-HCl*	9.3	-	0.76	0.03	0.73	152	93
c-ZSM-23-*ats2-HCl*	-	-	0.71	0.01	0.70	95	63
c-ZSM-23-*HCl*	5.6	-	0.57	0.05	0.52	200	76

[a] Determined by MP-AES.

[b] Volume adsorbed at $p/p_0 = 0.99$.

[c] *t*-plot method. V_{ext} and S_{ext} represent the pore volume and surface area for all the pores except the micropores.

[d] $V_{total} - V_{micro}$.

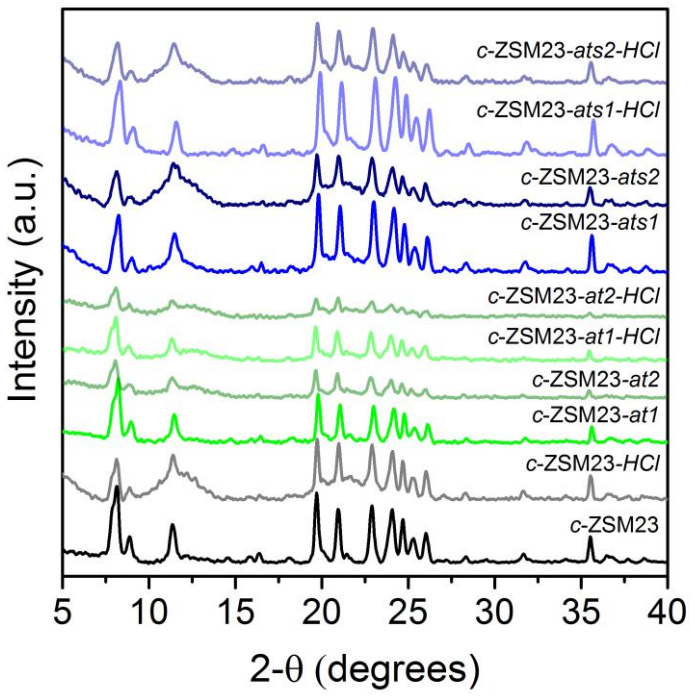

Figure A.3. PXRD patterns of parent and post-synthetic treated commercial ZSM-23 samples.

A.2. Papers I-IV